Time Resolved Particle Image Velocimetry Techniques with Continuous Wave Laser and their Application to Transient Flows

by

Amir Elzawawy

A dissertation submitted to the Graduate Faculty in Engineering in partial fulfillment of the requirements for the degree of Doctor of Philosophy, The City University of New York

2012

This manuscript has been read and accepted for the Graduate Faculty in Engineering in satisfaction of the dissertation requirement for the degree of Doctor of Philosophy.

Professor Yiannis Andreopoulos

Date

Chair of Examining Committee

Dean Mumtaz Kassir

Date

Executive Officer

Professor Peter Ganatos
Dept. of Mechanical Engineering, CCNY

Professor Jeffery Morris
Dept. of Chemical Engineering, CCNY

Professor Mark Glauser
Dept. of Mechanical & Aerospace Engineering, Syracuse University

Supervisory Committee

THE CITY UNIVERSITY OF NEW YORK

Abstract

Time Resolved Particle Image Velocimetry Techniques with Continuous Wave Laser and their Application to Transient Flows

by

Amir Elzawawy

Adviser: Professor Yiannis Andreopoulos

The demand to increase the temporal resolution of Stereo-Particle Image Velocimetry systems used in the measurement of highly unsteady flow fields is limited by the low repetition rate of the pulse lasers and cameras. The availability of high-frame-rate digital cameras and CW lasers opens new possibilities in the development of continuous PIV systems with increased temporal resolution. Time-Resolved Particle Image Velocimetry (TR-PIV) with continuous wave (CW) laser sheet technique and a high frame-rate camera is introduced here to be used in gas flows at low to moderate Reynolds numbers. This experimental technique can measure velocity of the flow in a planar field with good spatial and temporal resolution. Additional modifications led to the development of a Split view TR-PIV system capable of resolving three-component velocity fields. The optical setup consists of a single high-frame-rate camera which can accommodate two simultaneous stereo view images of the deforming fluid on its CMOS chip obtained by using four different planar mirrors, appropriately positioned. This approach offers several advantages over traditional systems with two different cameras. First, it provides identical system parameters for the two views which minimize their differences and thus facilitating robust stereo matching. Second, it reduces calibration time since only one

camera is used and third its cost is substantially lower than the cost of a system with two cameras.

The TR-PIV with the CW laser technique has been evaluated in canonical turbulent boundary layer flows and the results were compared to data from the vast literature. Particular attention has been given to the performance of the system components, such as the high speed cameras, and the CW lasers. The techniques were also investigated in terms of the duration of exposure of PIV images. The effect of the duration of exposure was proven to be particularly important, and it has a negative effect for the case with higher freestream velocity of 11m/sec.

In the second part of the present work, an application of the technique on transient flow with moving boundaries was attempted. This involved the investigation of the unusually high unsteady aerodynamic forces generated on a flat panel (actuator) during its impulsive deployment against the incoming turbulent boundary layer flow. The actuator is embedded in the wall and it's fully deployed when it reaches 90^{o} angle. Also, experiments at different deployment speeds (1 to 20 rad/sec) and different Reynolds numbers (23,000 and 68,200) were carried out to investigate their effects on the force generation. In particular three different sets of experiments were carried out. The first one aimed at directly measuring the aerodynamic forces with the means of a force balance. In these experiments, significantly higher aerodynamic forces are seen compared to the steady state case for the actuator at full deployment. These higher aerodynamic forces increase with the increasing values of the Strouhal number. The other two sets were carried out to understand the flow dynamics during the deployment. In these sets, flow visualization and TR-PIV experiments were carried out to investigate the flow structure around the actuator. It is has been observed that at the early stages of the deployment a tip vortex is

developed. This vortex carries significant strength as seen by the vorticity magnitude during the deployment. This vortex is separated from the actuator during the early stages of the deployment. However, it stays in the vicinity of the wake of the actuator during most of the deployment period, while a large increase in its strength is observed. It is believed that this strong vorticity field of the tip vortex structure is initially generated on the surface of the actuator during the early part of deployment, while the actuator is moving with high acceleration. This vortical structure, which is not observed in the steady state case, is seen to be convected downstream by the time the actuator is fully deployed. Other vortices of weaker strength continue to shed off the tip after the full deployment of the actuator as in the case for the steady state. A strong standing horseshoe vortex is seen to be established in front of the actuator at a late stage of the deployment.

The velocity data obtained by the TR-PIV techniques is also used to analyze the aerodynamic forces based on the flow field velocity data. This analysis shows a significant contribution of force terms involved unsteady vorticity, lamb vector, and inertial motion of the actuator. Viscous terms had almost no contribution to the total aerodynamic forces in both the drag and the lift directions.

“To my Mother”

Acknowledgements

I would like to express my deepest appreciation to my advisor, Professor Yiannis Andreopoulos, for his guidance and support. I am also grateful for his patience and constant encouragement throughout my research activity.

I owe special thanks to Professor Latif Jiji, who during my master's studies taught me not only subject, but also how student matters. And he has been a source of inspiration since then. I would like to thank Professors Feridun Delale, Peter Ganatos, Rishi Raj and Gary Benenson for their support, advice, and willingness to help, and being positive part of my academic experience.

I would especially like to thank Mr. Louis Hernandez for his support and always being available to help at any time and for any task. And special thanks to Mr. Bob Suhoke for his continuous support and technical help and advice throughout my research.

I thank my friends and colleagues Dr. Alexis Pierides, Dr. Savvas Xanthos, Dr. Mazen Diab, Dr. Pablo Bueno and Mr. Dogus Akaydin for their friendship, support, and willingness to help. I also would like to thank my students for teaching me that you learn more from different point of views than similar ones.

Finally, I would like to thank to my parents, family, and friends for their understanding, patience and encouragement when it was most needed.

Contents

List of Figures

List of Tables

Chapter 1 : Introduction

1.1 Motivations

It has been always a major challenge in experimental fluid mechanics to present a full picture of the dynamics of the fluids. This challenge becomes even greater when the flow becomes turbulent or when another dynamic element (i.e. moving solid boundary or other fluid) is added to the system under investigation.

A full picture of the flow dynamics requires a four-dimensional description of each element in the flow[1], in the three-dimensional space and time. Achieving the experimental technique that can accurately measure the velocity for each flow element has been the Holy Grail in experimental fluid mechanics.

The present experimental setup is meant to partially realize this goal. Time Resolved Particle Image Velocimetry (TR-PIV) with a continuous wave (CW) laser is introduced here to be used with gas flow at low to moderate Reynolds number. This is an experimental technique that can measure velocity of the flow in terms of both space and time, where both resolutions are only limited by the frequency of the high speed camera and the available laser light required for imaging. Classical PIV systems with pulsed laser provide only spatial information of the velocity, since it's limited by the laser frequency of 15 Hz. Also the advancements of the laser technology recently introduced high speed pulsed laser with frequency of 10 kHz. This provided another solution to achieve same objective. However, the system has had its limitations, for instance, the frequency rate, therefore the time resolution

[1] Flow element is the smallest scale element determined by flow conditions, (i.e. Kolmogorov length scale is used to determine the size of flow element in turbulent flow).

and light output per pulse are limited. It is also require more complicated setup in terms of the required synchronization of the laser, camera system in addition to the transient process under investigation. Also economically, the newly developed high repetition rate laser costs are considerably high.

With TR-PIV with the CW laser, both temporal and spatial resolutions of the velocity for transient flow conditions can be obtained. This would open up the door for more analysis to be done on the fluid flow as the velocity and its derivatives in terms of both space and time become known. This would include crucial physical terms such as the flow acceleration, its time rate of change, and the time rate of change of vorticity and strain. The availability of such terms for global (planar) flow field is new for experimentalists, which would provide a new insight to understand fluid flow.

As an attempt to classify transient flow to two categories for the purpose of this thesis, the first category would concern any introduction of a dynamic boundary into the flow field such as moving solid object, while the flow is turbulent or laminar.

The second category is turbulent flow in general, in which classical PIV systems provided us with a velocity picture that allowed experimentalists to study steady state cases, as well as the measurements of turbulence in statistical terms, where the average velocity values and the fluctuation quantities are used. However, the need to treat turbulence as time dependent process would greatly increase the understanding of the phenomena, which may result in potential engineering gains. A good example would be the turbulent boundary layer flow, where many aspects of this flow and how it evolves in time are still unknown.

In fact, many modern aerodynamic applications belong to the first category. For instance, recent technology advances created a great interest in flight that mimic insects and birds flight, where flapping wings can be used to improve flight control, maneuverability and overall aerodynamics. More important, the introduction of Micro Air Vehicle (MAV) and some Unmanned Arial Vehicle (UAV), which operate at low to moderate Reynolds number, showed an interest on designing based on unsteady conditions (i.e. impulsive or periodic flapping motion) to sustain flight conditions. At these Reynolds number levels, improvements in the aerodynamics are considerably desired, for instance, a moderate wind gust condition would produce a stall condition that can drive the vehicle out of control. This situation is particular to these new types of air vehicles, since all fixed wing air vehicles are designed for higher speeds to sustain these conditions.

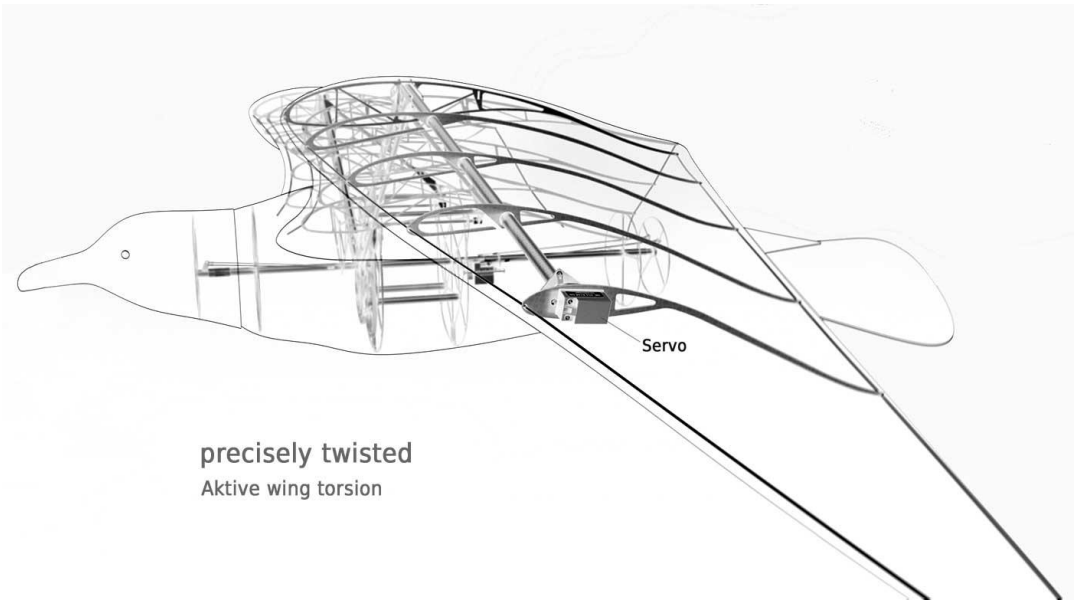

Figure 1-1: "SmartBird" by Festo Corp. (The twisting of each wing side is controlled by servo motor 2011)

On the other hand, early studies by Ellington et al. (1984 and 1999) and Willmott et al., (1997) indicated the large difference of the aerodynamics generated of the flapping flight of

birds compared to classical fixed-wing aerodynamics. These differences are mostly pointing toward improvements in the aerodynamics characteristics, such as higher lift coefficient and delay of the stall angle of attack. More recently, the same conclusion also came to be true for insects' flight (Dickinson et al. 1999, and Sane 2003). This type of flow can be studied using techniques such as PIV, which provides global velocity information for the flow. TR-PIV would be more suitable to such application where the flow is characterized by unsteadiness.

PIV and TR-PIV like techniques become not only limited to the fluid mechanics community, but also to other fields such as experimental biology, where researchers heavily rely on this type of experimental techniques that resolve the velocity of the flow field. Particularly in experimental biology, large number of researches seen recently to heavily use classical PIV to look to the complex aerodynamics of flapping flight (Hedrick et al., 2004); (Spedding et al., 2003), (Hedenstrom et al., 2006 and 2007).

The second category, the turbulent boundary layer flow, has always been an interesting complex problem from both a physics and mathematics point of view. In engineering terms; it is also important to obtain better flow characterization, since great beneficial outcomes can be gained from understanding and controlling this flow. For example, drag and friction in general are a major concern for the industry, and any ability of their reduction would produce many engineering gains such as reduction in fuel consumption. In addition to this, in aerodynamics, flight and noise control are existing engineering problems where improved understanding and control of the turbulent boundary layer flow would also provide better solutions.

With the introduction of non-intrusive quantitative visual techniques such as PIV, a new look at the turbulent boundary layer flow is possible. The planar velocity information obtained by

the PIV of the turbulent boundary layer (TBL) is a relatively recent one. Before this, only qualitative visual information of the flow, and point measurements were the recognizable tool to investigate this type of flow. The limitations of these tools have added to the challenge, where the lack of flow information pushed for heavy mathematical, particularly, statistical presentation of the flow, to reach some generalized conclusion. An evident example of the benefits brought with the application of PIV in studying TBL is the recent results that showed large scales structures (Large scale motion or LSM), shown in figures 1-2 and 1-3, consisting of vortex packets to exist in the log layer. These structures are believed to be created as multiple hairpin packets travel at the same speed (Andreopoulos & Agui 1996, Kim & Adrian 1999, Zhou et al. 1999, Guala et al. 2006, Balakumar et. al 2007). Each of these structures has an outer length scaling in the streamwise direction of two to three times the boundary layer thickness (2-3δ).

More recent, larger structures referred to as superstructures (Hutchins & Marusic 2007), shown in figures 1-2 and 1-3, are identified also on the logarithmic region (Monty et al. 2009) with length scale more than six times the boundary layer thickness (> 6δ). Superstructures were identified also in pipe and channel flow and referred to as Very Large-Scale Motion (VLSM), however, in the case of bounded flow these structure found to be located on the outer layer (Bailey et al. 2010). These structures carry for 40 to 65% of the kinetic energy and 30 to 50% of the Reynolds stress (Balakumar et al. 2007), however, the mechanisms of the creation of both LSM and superstructure are yet to be known. As mentioned previously that the use of PIV and TR-PIV was a major contributor tool for these recent findings, and we believe the use and the availability of TR-PIV can provide further understanding of the creation of these structures. Although, understanding the creation mechanisms of these

structures are not a focus topic of the present work. TBL flow is utilized in part I of this thesis to as a test bed evaluate and characterize the current technique.

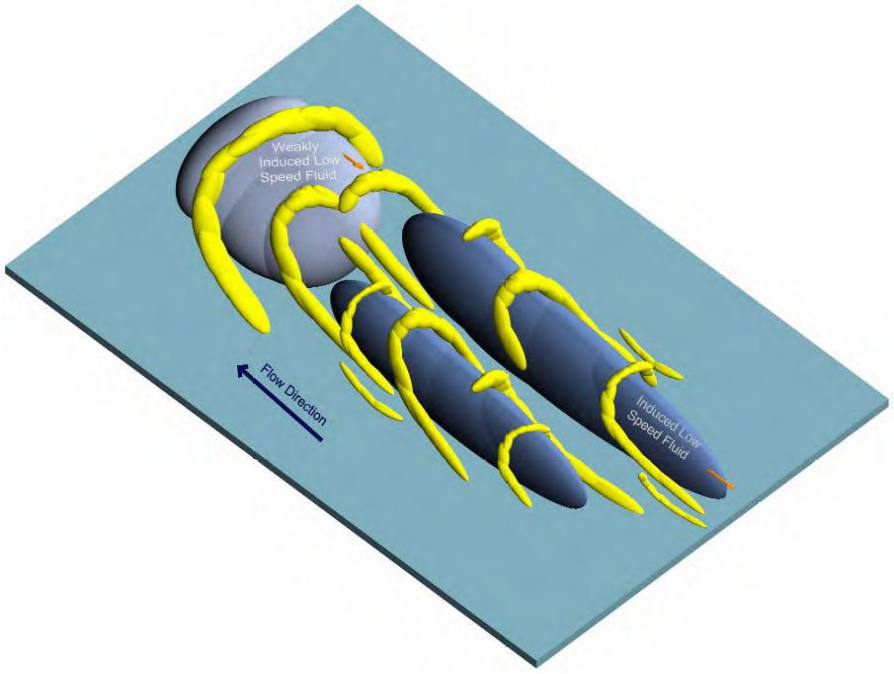

Figure 1-2: Several LSM creating Superstructure in TBL flow (Tomkins & Adrian 2003)

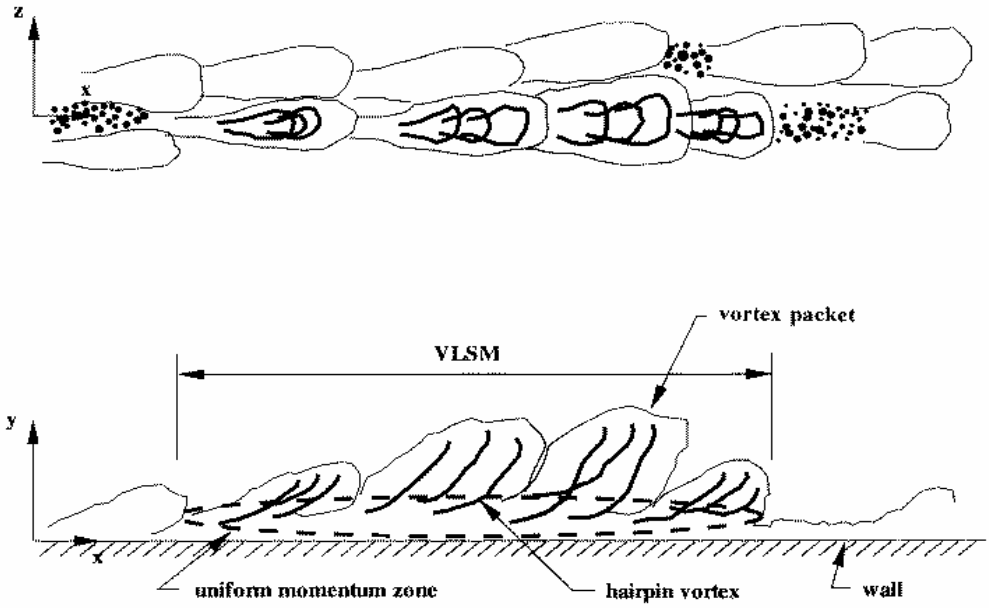

Figure 1-3: Top and side view of VLSM consist of multiple LSM of moving vortex packets (Balakumar & Adrian 2007)

Another potential benefit of acquiring time resolved velocity information, is that time resolved analysis of the flow can be applied to develop and better evaluate new models to describe transient flows for CFD methods which deal with unsteady and turbulence flow problems. With the increasing computational ability of present computer systems more and more CFD models are being developed to solve application-oriented turbulent flow problems with high spatial and temporal resolutions at high Reynolds numbers for large scale applications. Therefore producing temporally resolved velocity information would provide an important validation tool for these CFD models.

In terms of the PIV techniques, TR-PIV increases the dynamic velocity range (DVR) for the measurements, by allowing correlating not only a pair of consequent images but also two images with the desired Δt to resolve all the velocity ranges different images. For example, in high velocity gradient flow field, where the velocity magnitudes significantly vary in value within the same flow field, the images can be recorded at high frame rate, and small velocities can be computed using the correlation of images with small Δt, where large velocities can be obtained by correlating images at larger Δt.

Another benefit of the use of TR-PIV data is to validate velocity vectors by comparing the velocity values in consequent PIV realizations at the same spatial location and filter out the spurious vectors. Vector validation is an essential step to successfully and efficiently obtain correct velocity information; this is due to the large number of velocity vectors in the flow field multiplied by PIV acquisitions for each experiment. It's also as important in practical terms to automate the validation process to a large degree. In classical PIV, the spatial neighboring vectors are commonly used to validate the local velocity vector, with TR-PIV, another reliable validation filter can also be applied.

Another advantage of the present techniques is the use of CW laser which reduces the cost of the PIV system not only compared to other commercially available TR-PIV systems with high-repetition-rate pulsed laser, but also to the classical PIV with the Pulsed laser. As the CW laser becomes an established mean for illumination, the system cost would be significantly reduced, hence the cost of the CW laser (Diode-Laser) is drastically less than the double-head-Nd-YAG pulsed laser used for classical PIV system, and much less than the high repetition rate Nd-YLF laser currently available for commercial TR-PIV systems. According to R. J. Adrian (2004) in his paper titled "Twenty Years of Particle Image Velocimetry", one of five desirable developments to PIV he referred to in his conclusion remarks quoted as follow: "Means should be sought to reduce total system costs by reducing the costs of light sources and cameras". A significant reduction of the cost due to the use of CW laser would give the opportunity to many other researchers to apply a successful robust PIV system to their research. It's quite important to mention here that the present CW laser at the available power (less than 10 watt), which we propose for TR-PIV use, is limited to low to moderate Reynolds number in gases where the Nd-YLF has broader use to include higher Reynolds number flow as well. However, we believe the flow speeds considered for use here still include a broad spectrum of flow applications. At the same time the wide use of PIV would reflect on the advances on fluid mechanics research and many engineering applications.

1.2 PIV History and Recent developments

Particle Image Velocimetry was first developed by R. J. Adrian in 1984 as "*quantitative measurement of fluid velocity at a large number of points"* referring to its ability to obtain planar velocity measurements simultaneously. Advances in the camera system, specifically the shutter control, moved the system forward from one-frame double-exposure, relying on

auto-correlation methods for vector computations, to double-frame double-exposure images that allowed the use of cross-correlation methods. The move to digital image recording (C. E. Willert and M. Gharib, 1991) and (J. Westerweel, Ph.D. thesis, 1993) was particularly a significant step as it moved the computation process to be executed by computer systems directly.

More advances in the digital camera resolution improved the technique spatial resolution significantly; some systems currently offer 11-MegaPixel-CCD to be used for PIV.

The Interframe time also improved drastically by the introduction of on-chip storage CCD. This allowed storing the first image on the same chip, therefore faster acquisition for the second image. This technology allowed for interframe time to be in order of 100's of nanoseconds.

The ability to compute the velocity vectors has also improved significantly with the continuous increase of the capabilities of the computer systems and many improvements of the correlation algorithms focused on PIV systems. The increase of accuracy of detecting the correlation peak increased the number of vectors per image resulting in higher spatial resolution.

On the optical side, Stereo-PIV, which refers to stereographic imaging for the flow field shown figure 1.4, allowed to measure the three-component-velocity vector inside the planar field by the use of two cameras with stereographic view to the sheet as shown in figure 4 (Y. G. Guezennec et al. 1994; T. Dracos et al. 1993; H. G. Maas et al. 1993; N. Kasagi and K, Nishino, 1993).

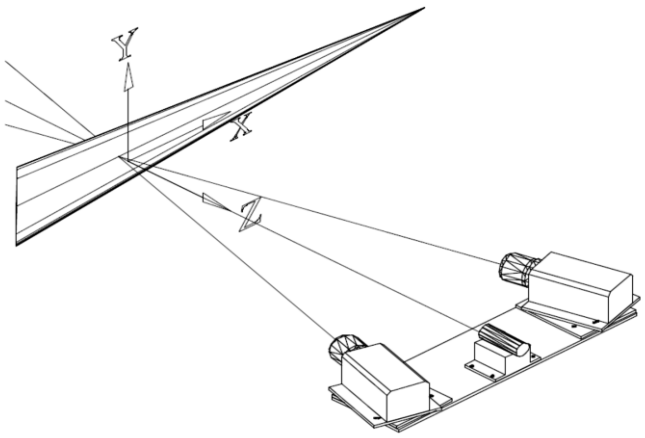

Figure 1-4: Stereo-PIV: two-camera system to resolve three-component velocity field (planar laser sheet represented by triangle in X-Y plane)

Also on the optical side, other systems specialized in specific type of flows, such as micro-PIV (J.G. Santiago 1998) is used for micro scale flow using microscopic lens for magnification.

Also, concurrently to the present work, TR-PIV using high repetition rate Nd-YAG and Nd-YLF pulsed laser and high speed CMOS camera was developed (M.P. Wernet 2007); (Troolin et. al 2006) this provided high temporal resolution velocity images, the system is limited by the repetition rate of the laser which reached 10 kHz and the laser power level.

And recently, two different volumetric PIV systems developed, the first is Tomographic-PIV (G. Elsinga, Ph.D. thesis, 2008) uses images obtained by four-camera system and volume illuminated field to reconstruct the 3D mapping of the particles, followed by correlating the particles' pattern to obtain the displacement in the flow volume. V3V or 3D3C (3-dimensional 3-components) system (K.V. Sharp et al. 2009) is also developed for three dimensional velocity measurements. The system became commercially available by TSI Inc. in 2010. In 3D3C, Volume illumination (140X140X100 mm^3) and three-camera system is used to resolve the velocity in 3D volume. The system is limited to liquids, where relatively large particles

are suitable, while the system is not used for gas flow due to the scarcity of the light signal produced by small seeding particles.

1.3 Objectives

This work is divided into two parts; the main objective of the first part of this thesis is to develop an evaluation and assessment procedure. This allows understanding of the quality of the measurements and the limitation of the use of TR-PIV with CW laser. This objective is achieved by using the technique to measure the characteristics of the turbulent boundary layer flow and comparing the results with similar flow results from the literature some of which were performed in the same facility. In addition, the quality of the imaging and the effect of using different component to the system will be investigated.

In the second part, an application of measuring an unsteady turbulent flow interacting with moving solid boundary, in this part the transient force generation on a flow actuator during impulsive deployment inside a turbulent boundary layer is investigated, where the aerodynamics in this transients condition are shown to be significantly different to aerodynamics of steady state condition. In addition Strouhal number effect on the aerodynamics is also investigated. In this part, TR-PIV, flow visualization, and other aerodynamics experiments are carried out to understand this transient phenomenon in terms of the relation of vortices generated at the actuator edge and the increase of the aerodynamic forces.

1.3 Thesis Outline

- Part I: Evaluation and Characterization of TR-PIV with CW laser in Turbulent Boundary Layer.

- Chapter 2: Description of the experimental facilities (including the wind tunnel facility at CCNY, all laser and camera systems and several other experimental components used in the present work). In addition to this, a description of experimental approaches applied for PIV acquisition method is included.
- Chapter 3: Turbulent Boundary Layer Experiments are conducted in two sets to study the effect of several parameters of the system components such as lasers and cameras settings on the results. In addition to the investigating the effect of other experimental parameters such as the exposure time and the flow speed.

➢ Part II: Investigation of transient Force Generation on flow actuator during impulsive deployment inside TBL.

- Chapter 4: Introduction includes a description of the experimental procedures and objectives of the transient deployment of an actuator embedded in TBL experiment.
- Chapter 5: Detailed experimental work to direct measurements of lift and drag forces and coefficients in addition to measuring the actuator's dynamics during the transient deployment. Also this chapter includes investigation of the effect of the Strouhal number on the aerodynamics.
- Chapter 6: Detailed description of flow visualization experiments and TR-PIV measurements of the flow around the actuator during its impulsive deployment. We will also attempt to give three-dimensional image for the flow topology and describe the flow evolution in time. In addition to this, we discuss the contribution of the vorticity terms to the unsteady aerodynamic loading.
- Chapter 7: Split-View TR-PIV technique with CW Laser to obtain three-component velocity field around the actuator during the impulsive deployment.

- Chapter 8: Summary and recommendations for future work.

Part I: Evaluation and Characterization of TR-PIV with CW laser in Turbulent Boundary Layer.

Chapter 2 : Experimental Setup & Facilities

2.1 Wind tunnel facility

Wind tunnel facility at Experimental Fluid Mechanics and Aerodynamics Laboratory, shown in figure 2.1and 2.2, is an open-return-suction-type with cross-section of 1.20 m x1.20 m and 8.40 m testing length (Honkan and Andreopoulos 1997). The flow is driven by a seven-blade-axial-fan at the end of tunnel that can provide air flow up to 11.5m/s in the working section. The motor driving the fan is 20 hp, 1750 RPM, 460 V frequency controlled AC motor that can be remotely controlled to change the flow speed by changing the AC current frequency. The fan was built in a separate housing with sound absorbing diffuser to reduce acoustical noise; the housing is also mounted on eight springs to minimize vibrations produced by the fan assembly.

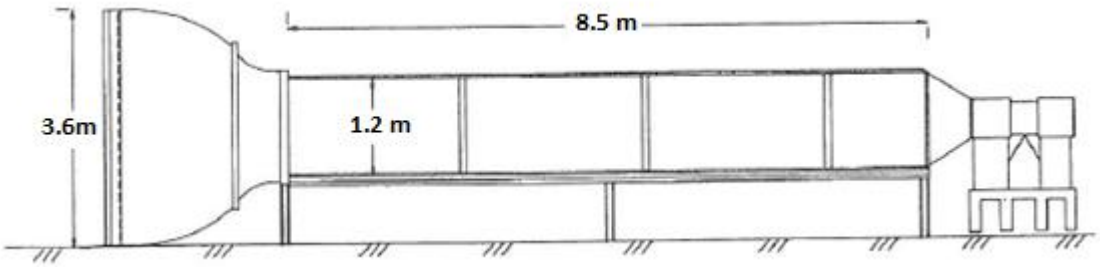

Figure 2-1: Schematic of wind tunnel facility at Aerodynamic lab at CCNY

The right side wall (in the flow direction) is made of 1-in clear Plexiglas to allow optical access. A honeycomb structure and a diffuser are built at the entrance to ensure uniform laminar flow in the working section. A higher speed flow can be produced in the tunnel by manipulating the tunnel cross section area; however, in the present work a constant cross

Figure 2-2: Photograph of the wind tunnel facility

section area alongside the testing area is maintained to produce zero-pressure-gradient boundary layer (ZPG-BL) with laminar constant freestream.

2.2 Particle Image Velocimetry

2.2.1 Basic Principle

Particle Image Velocimetry or PIV is a non-intrusive technique that was first developed as an experimental technique to measure the velocity vectors in a thin sheet (planar field) by measuring the displacements of the numerous small particles that faithfully follow the flow motion (Adrian 1986). The displacement **(x)** of the particles are measured by comparing the particles position in two subsequent images with known time difference Δt between the images $\mathbf{V} = \mathbf{x} / \Delta t$.

From this simple idea, and with the great advantage of the non-intrusive nature of the technique, the PIV considered the first robust technique that allowed experimentalists to obtain the global velocity information for fluid motion.

Identifying the same particle in each frame was previously used in Particle Tracking Velocimetry (PTV) to measure the velocity, however, low particle-density images was required, and the output velocity field contained few patchy velocity vectors. To produce a complete velocity field, PIV relied on imaging much higher particles density flow field. This made it impossible to identify each particle in both frames; because of number of similar size particles occupy the entire flow volume at the same time. For this reason, identifying a pattern of a group of particles instead of an individual particle, as shown in figure 2-3, is used to track the motion of the flow using correlation methods. These correlation methods, which are used to compute large number of velocity vectors, are proven to be a computationally costly, and in many cases are challenging. This necessitates applying preprocessing and post processing techniques to produce valid velocity image for the flow field.

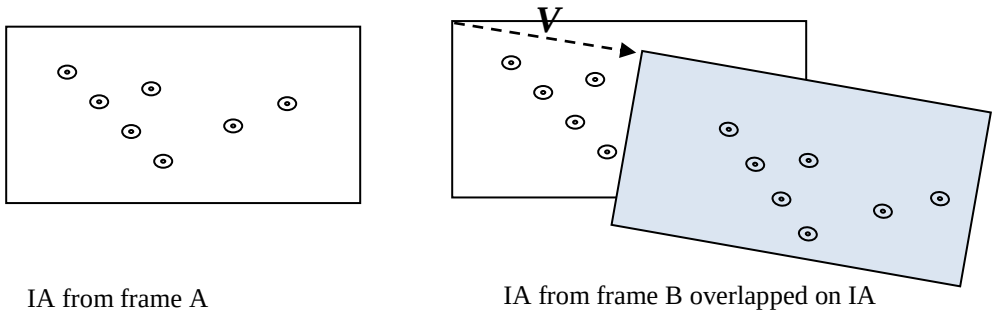

Figure-2-3: PIV method to compute velocity vector by measuring the difference in position vector of group of particles inside specified Interrogation Area (IA) in two

2.2.2 System Components

The basic digital PIV system includes the following components:

1. A light source for sheet illumination (visible Laser light).
2. Camera system capable of capturing subsequent images with small time difference.
3. Seeding particles to scatter the light.
4. Computer system to digitally register the images and perform the computational tasks.
5. Optical arrangement to create the light sheet.

Each of these components is explained in details in this chapter in terms of the settings used in the present work.

2.3 Laser Systems

Three Laser Systems have been used as a light source to illuminate the flow. All Lasers working in the green spectra: Laser 1 is used for classical PIV acquisition, Laser 2 and 3 are CW (continuous wave) lasers, both are used for TR-PIV experiments. In the following section, detailed description of all laser systems and specifications is discussed:

2.3.1 Laser 1

Laser 1 is an Nd-YAG double-head Q-Switched laser that produces 532nm at the rate of 15 Hz per head of with energy up to 190mJ. Nd-YAG is a solid state pulsed laser and the beams from the two laser heads are combined into a collinear beam. Each produces < 10 nanosecond laser pulse in Q-Switched mode. The short duration of the pulse provides an image of almost a still flow in each of the camera frame. The small exposure time, which equals to the pulse duration, does not contribute to the uncertainty of the measurements at the speed used in the present work. This made Laser 1 acquisitions to be used as a benchmark in many cases in the present study to investigate the effect of the duration of the exposure on the flow measurements.

Laser 1 is manufactured by BigSky, and it was purchased as part of a standard Stereo-PIV system from TSI Inc., together with a synchronizer, which is used to time the laser pulses and the cameras exposure. A light-Arm (figure 2.4) is used for the purpose of manipulate the laser beam without losing the collinearity of both lasers beam. However, this collinearity required to be reestablished every time the laser head is moved relative to the light arm.

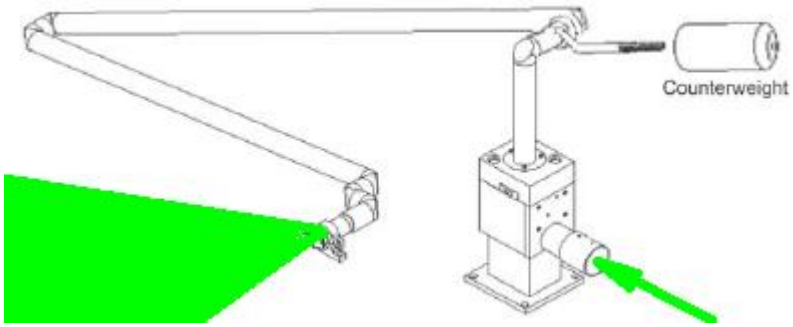

Figure 2-4: laser beam enters the light arm from one end, and on the other end laser sheet optics are mounted

2.3.2 Laser 2

Laser 2 is an Argon Ion laser which produces up to 2 watt continuous wave (CW) beam at 514nm wavelength. The laser was built by Spectra-Physics and purchased by CCNY as part of an LDV (Laser Doppler Velocimetry) setup. In the present study this laser system was used to provide illumination needed in the TR-PIV. The laser beam was manipulated to create a laser sheet inside the wind tunnel by appropriate optical arrangement (see section 2.6 for details). The low output power of the Ar+ (Laser 2) proved to be challenging to obtain PIV measurements at full range of the wind tunnel operating speeds (more details in chapter 3). The system also requires high maintenance level to maintain output power at 2W; in addition to this, the system used high flow rate (open-cycle) water system for cooling.

2.3.3 Laser 3

Laser 3 is Diode Laser Model Millennia VS 110R that produces up to 5.5 watt at 532nm CW beam. The laser is made by Newport corp. The output power can be remotely controlled, and it is equipped with a closed loop power control to optimize the current supply to maintain the desirable power output. The system is cooled with closed cycle water cooling system housed in a separate unit. The laser head unit is small in size attached to the power unit with 3 meters fiber optics cable, which provided convenience in mobilizing the laser beam without lose in power due to the addition of optical components (mirrors). Table 2-1 shows the summary of the lasers system bulk characteristics.

	Nd-YAG (Laser 1)	**Ar+ (Laser 2)**	**Diode Laser (Laser 3)**
Max. output power	**190 mJ/pulse**	**2 Watt**	**5.5 Watt**
Emission	**Pulsed (>10 ns)**	**CW**	**CW**
Beam Diameter	**8 mm (at 532 nm)**	**1.4 mm**	**2.3 mm**
Wavelength	**532 nm (with second harmonic generator)**	**514 nm**	**532 nm**
Cooling System	**Water (Closed Cycle)**	**Water (Open Cycle)**	**Water (Closed Cycle)**
Beam Divergence	**<0.5 mrad**	**<0.5 mrad**	**<0.5 mrad**
Power Stability	**± 5 %**	**± 0.5 %**	**±1%**

Table 2-1: Lasers Specifications

2.4 High Speed Camera Systems

Two high speed cameras have been used throughout this research. The first Camera System which became available in 2008, will be referred to as Camera1. The second Camera system, which will be referred to as Camera2, became available to this research in 2010. More details

about both camera systems and general comparison of both technologies are presented in this section.

2.4.1 Camera 1

Imacon 200, made by DRS Technologies, is an Ultra High Speed Camera that can acquire up to 8 frames at a maximum rate of 200MHz. The camera uses 18mm-MicroChannel Plate image intensifiers coupled to four one-Megapixel-CCDs. Each CCD is capable of capturing two separate images per run. CCD channels mounted around a specially designed beam splitter (see figure 2.5). This beam splitter divides the available light into four separate paths for the individual channels. The exposure time of the individual image intensifiers can be controlled electronically by switching the voltage applied to the Micro Channel Plate at very high speed, using a crystal controlled 200MHz oscillator which gives the camera 5ns temporal resolution between frames on the same CCD.

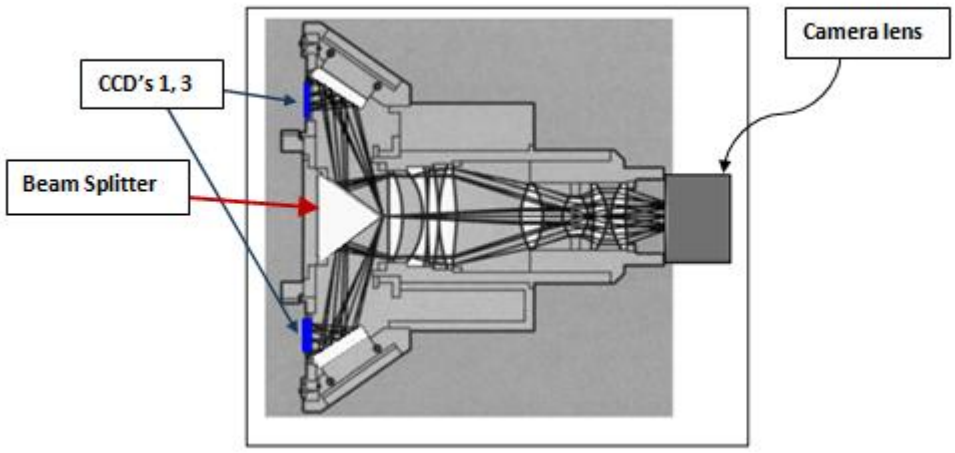

Figure 2-5: Section view for camera1 shows the optics arrangement to distribute the image over four CCD's using beam splitter (only two CCD's can be seen in this view)

2.4.2 Camera 2

Phantom 710, made by Vision Research, is a high speed camera with acquisition rate up to 7500 fps at full resolution of 1280x800 pixels and memory capacity of 8 GB of high-speed dynamic RAM. This high capacity is much needed for acquiring large number of images especially when used for turbulence statistical measurements. Phantom high speed camera uses CMOS chip which is different chip technology for image acquisition.

CMOS (complementary metal oxide semiconductor) chip is a relatively a modern technology. In CMOS chip, a complementary transistor built in the chip itself allow low power high gain amplifying, which also shorten the signal trace distance. The transistor allows also for all the function to be built on the physical pixel. This makes the output of the pixels into digital bits, so no post acquisition digitization is needed as in the CCD chip. Table 2-2 shows a summary of the camera systems characteristics and specifications.

	Imacon 200 (Camera 1)	**Phantom 710 (Camera 2)**
Spatial Resolution	**1200 x 980**	**Up to 1280 x 800**
Max. Speed (fpr)	**Up to 200 MHz at full resolution**	**Up to 1.4MHz (128 x 8)**
		Up to 7500 (1280 x 800)
Depth	**10 bit**	**8 bit to 12 bit**
Min. Interframe times	**5ns**	**300ns**
Min Exposure time	**5ns**	**300ns**
Sensor	**CCD**	**CMOS**
Images acquired per run	**8**	**>30,000**
Pixel Size ($\mu m^{2)}$	**6.45**	**20**

Table 2-2: Camera systems specifications

2.5 Flow Tracer particles

Flow tracer is a central element in PIV measurements; the choice of the particle depends to a great extent on the flow medium. The basic presumption is that the tracer particles can follow the flow faithfully. One way to achieving faithful condition here can be by having a particle with frequency response that is higher than the highest flow feature that represents any significant energy in the flow measured.

From looking at the motion of the particle with respect to the flow, it is anticipated that the main source of relative motion between the particle and the flow can be calculated using the analogy of the velocity induced by the gravitational forces and the buoyancy U_g. This velocity can be calculated from Stokes' law of drag for spherical particle at very low Reynolds number.

$$U_g = d_p^2 \frac{(\rho_p - \rho)}{18\mu} g \qquad \textit{Eq. (2-1)}$$

where d_p is the particle diameter, ρ_p, ρ are the particle density and the flow density respectively, μ is the dynamic viscosity of the fluid, and g is the gravitational acceleration. In our case the relative velocity of the particle and the moving fluid (U_s) can be estimated in a similar manner to (2.1) as follow.

$$U_s = d_p^2 \frac{(\rho_p - \rho)}{18\mu} a$$

where **a** is the relative acceleration of the particle to the moving flow. For the case of air flow, the density of the particle is much greater than the air density:

$$\frac{U_p(t)}{U} = \left[1 - e^{\left(-\frac{t}{\tau_p}\right)}\right]$$

Where τ_p is the relaxation time for the particle with constant acceleration given by:

$$\tau_p = d_p^2 \frac{\rho_p}{18\mu}$$

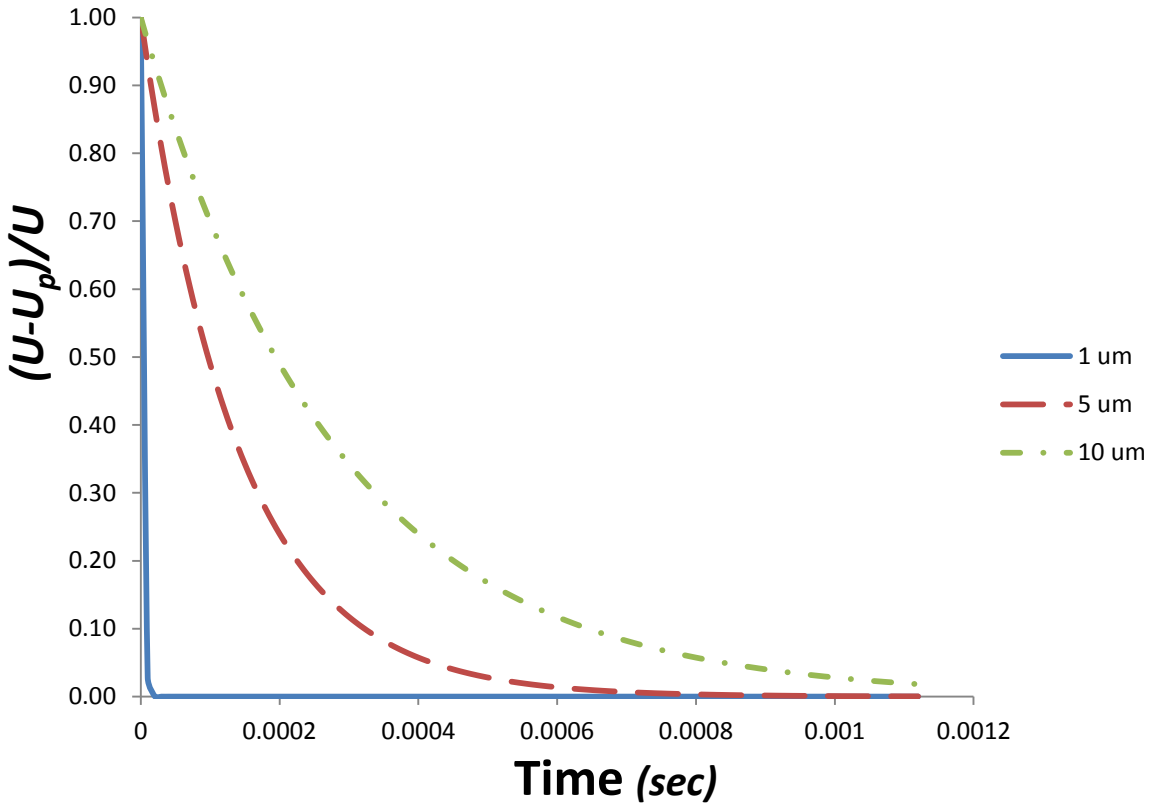

Figure 2-6: the effect of the particle size on relative motion between the particle and the flow

Figure 2.6 shows the response time of the relative motion of the particle decreases significantly by the decrease of the particle diameter. A particle with a nominal diameter ≈ 1 μm seemed to be an appropriate choice for the presented flow conditions. Note that the above analysis is not applicable for significantly high acceleration values, in addition to that; the analysis is also based on the applicability of Stokes' Law of Drag, and the response time is evaluated based on constant acceleration. Therefore in the case of non-constant acceleration, the above exponential decay for the response time would not be appropriate to follow.

However, the flow cases considered in the present work are well within the range of acceleration where this analysis is applicable.

A particle size of one micron can be obtained by atomizing vegetable oil using a high pressure air jet. In the present work olive oil is used to produce tracer particles, due to the fact that it's organic and non-toxic. This also makes it suitable for the experiments done in an open wind tunnel facility. The required particle size of 1μm diameter has been obtained by atomizing the oil when we use Laskin nozzles to generate micron size droplets (TSI Particle Atomizer).

The atomization process uses air under high pressure (60 to 80 psi) to be injected into the olive oil using six small pipes with Laskin nozzles at the liquid end (see figure 2-7). The high speed air flow coming out of the Laskin nozzles, and because of the high shearing effect, creates air bubbles inside the oil with atomized olive oil droplets inside them. The air bubbles then move upward, where they come out from a 2-inche-diameter outlet pipe.

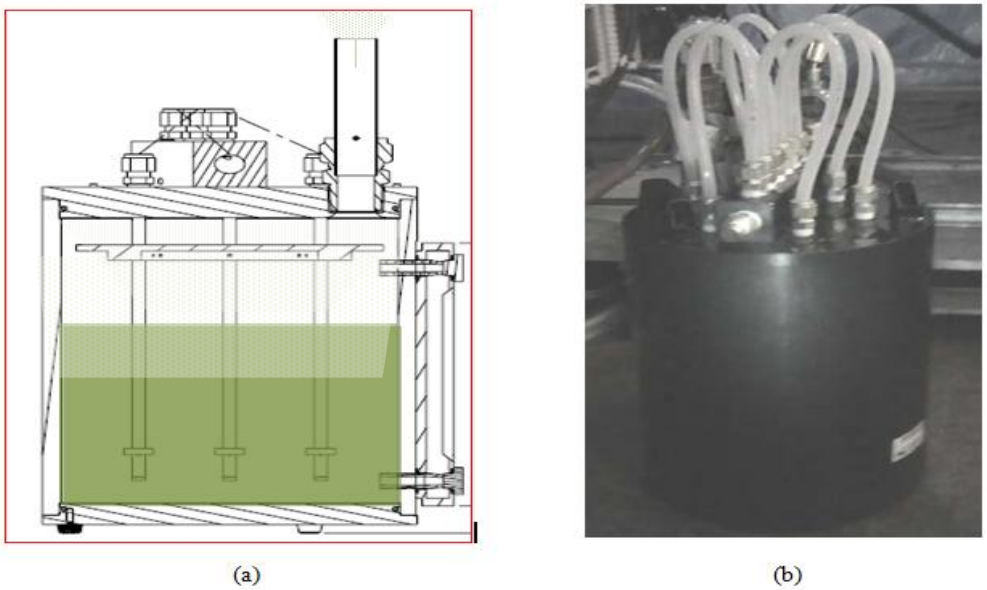

Figure 2-7 Particle Tracer Atomizer with six Laskin nozzles by TSI Inc. (a) section view, (b) actual photograph

2.6 Laser Sheet Optics

The quantitative nature of the PIV measurements requires determining the exact location of the particle in space, and because the camera lens in PIV has a wide depth of field. A reliable method of identifying the exact location of particles in space is to limit the illumination to a thin sheet (planar). This way, the normal distance to the image plan is preset, avoiding uncertainty associated with this direction.

A system of two lenses is used to create the desired sheet, the first is a cylindrical lens that is used to create a light sheet with thickness equal to the beam diameter, the focal length of this lens determines the spread angle of the triangular sheet as seen in figure 2-8a.

Second, a spherical lens is used as collimator to decrease the laser sheet thickness (shown in figure 2-8b) to a desired thickness. The choice of the lens depends on the beam diameter, the desired sheet thickness, and the distance to the field of view (FOV), where FOV is usually located at waist (minimum thickness). In figure 2-4b the side view of the sheet is shown as it converges at the focal length of the spherical lens

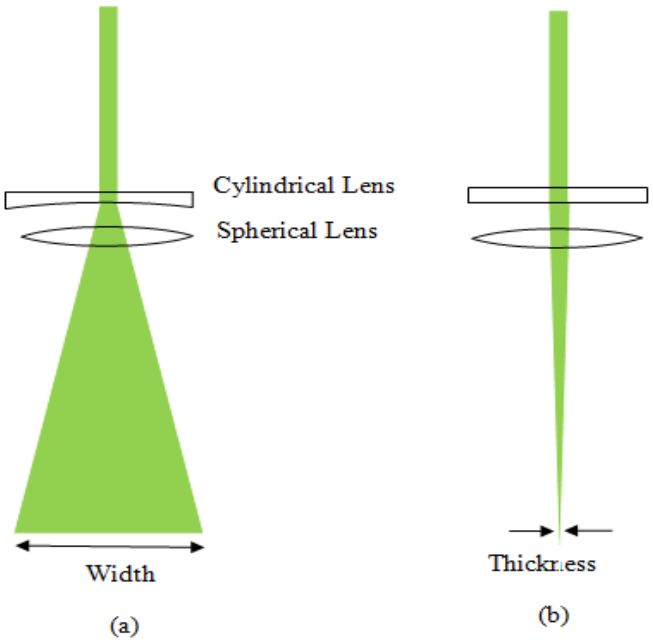

Figure 2-8: Sheet Optics, (a) Front view: the cylindrical lens is used to create a sheet of light, (b) Side view: the spherical lens is used to have a narrow sheet of light.

It's important in the present work to efficiently use of the light produced by the CW laser to obtain high signal to noise ratio in the PIV processing. For this reason a groups of five different optical arrangements of the light sheet optics were used to illuminate the desired flow field.

Chapter 3 : Testing in Turbulent Boundary Layer

3.1 Experimental Approach

In this chapter, we will evaluate the TR-PIV system in terms of the system components such as the camera and the CW laser and their parameters. This system has been utilized to carry out measurements in a canonical Turbulent Boundary Layer (TBL) flow at different Reynolds numbers. The measurements have been obtained in the streamwise-wall-normal direction. Several quantities are considered in this investigation, such as the mean flow parameters, statistics of velocity fluctuations and turbulent quantities, in addition to time resolved measurements of the flow; these quantities will be used for evaluating of the technique, where well documented results of this canonical flow are available in the literature as well as for the same facility.

The following is an outline of this chapter to achieve the objective mentioned above:

1. PIV measurements using Nd-YAG laser and Camera 1 (Imacon 200). In this section Camera 1 is used in the classical PIV mode with low frequency of acquisition rate (15 Hz). The results are used to characterize the camera performance.

2. Initial TR-PIV measurements, which will also be referred to as SET1, using Camera1 and Laser2 to be compared to first step results, followed by evaluation of the challenges and the major parameters to be investigated for the technique.

3. TR-PIV data are collected using Camera2 and Laser3, which will also be referred to as SET2. In this set of data, obtaining high quality data was the main objective. The experiments were performed at two different Reynolds numbers. The results are compared to previous TBL results from literature, some which were obtained in the same facility by hot wire and Laser Doppler Velocimetry (LDV).

3.2 Turbulent Boundary Layer over Flat Plate

3.2.1 Introduction

Turbulent Boundary Layer flows have been under intense investigations for decades, its importance to everyday engineering application forced scientists and engineers to keep looking deeper in this type of flow to gain profound understanding. This understanding has been considered by Lighthill (1995), Prandtl (1904) to have an impact on fluid mechanics similar to the effect the Einstein's (1905) had on physics.

A canonical Zero-Pressure Gradient Turbulent Boundary Layer (ZPG-TBL) flow is considered here, as it's been well studied and documented theoretically as well as experimentally. In the following section, a brief introduction to some of the scales and physics will be provided.

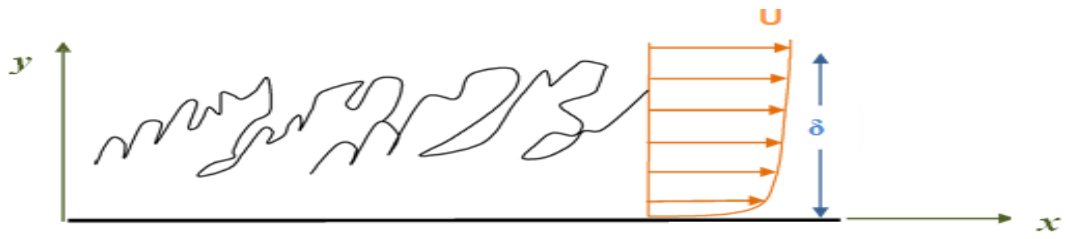

Figure 3-1: Turbulent Boundary Layer

3.2.2 Theoretical Background

When a laminar flow approaches a flat plate, a small layer starts to grow over the flat plate due to no slip condition at the wall surface. This layer becomes unstable and subsequently transitions to turbulence when Reynolds number is high enough ($\approx 5x10^5$). This layer exhibits very chaotic dynamics that is difficult to be explained with one model, partly due to the change of significance of the each scaling parameters on the flow properties. For instance close to the wall, a very small layer is developed; this layer referred to as viscous wall region, where the main scaling parameters are the wall friction and the fluid kinetic viscosity. Similarly further away from the wall the viscosity and the wall friction effect diminish greatly, and the flow characteristic parameters such as the freestream velocity become more influential. Some of these major quantities can be given in non-dimensional form:

- Inner wall scaling:

  Length: $\delta_v \equiv \nu/u_\tau$ (Viscous length scale) Velocity: $u_\tau \equiv \sqrt{\frac{\tau_w}{\rho}}$ (Friction velocity)

  Wall units: $y^+ \equiv \frac{u_\tau y}{\nu}$

  Wall shear stress: τ_w

  Non-dimensional velocity based on wall friction velocity: $U^+ \equiv U/u_\tau$

- Outer Layer Scaling:

  Length: δ (Boundary Layer thickness) Velocity: U_e (freestream velocity)

3.2.2.1 Inner Layer (Prandtl, 1925)

This layer can only be resolved in terms of wall units:

$U^+ = f(y^+)$ this layer exhibits universal profile for U^+ , as it is independent of the external flow. Although, it's not $f(\delta)$, it occupy $y/\delta < 0.1$ (Pope 2000); in this region the shear stress τ is approximately constant.

This layer can be subdivided into:

- Viscous sublayer $y^+ < 5$ where the shear stress is only caused by viscosity.
- Buffer Layer $5 < y^+ < 30$
- Log Law region $y^+ > 30$ *to* $y/\delta < 0.3$, this layer starts inside the inner layer and it extend over the overlap layer, and it ends in inside the outer layer, the flow in this layer exhibits a universal U^+ profile.

3.2.2.2 Overlap Layer

This is a layer comes between the inner layer where viscosity is dominant, and the outer layer where the viscosity has no role. As noted by C.B. Millikan (1937) the inner and the outer layer can only smoothly overlap if the velocity profile is logarithmic.

$$U^+ = \frac{1}{\kappa} \ln y^+ + B$$

where κ and B are constants, typically $\kappa = 0.41$ and $B = 5.1$, small changes can be seen to these constant, usually attributed to the pressure gradient.

The above equation is usually used as starting point to evaluate u_τ through an iterative process, consequently τ_w can be evaluated.

3.2.2.3 Outer Layer

In this layer the flow velocity starts to depart the universal logarithmic law. This part of the outer layer is called the defect layer. The flow in this layer will be influenced more by the freestream velocity U_0. In fact U(y) can be looked at in non-dimensional $(U_e\text{-}U)/u_\tau$ as a function of y/δ (Von Karman, 1930). Cole's (1956) saw the change of velocity in the outer layer as a deviation, which had a wake-like shape:

$$U = U_{\log law} + \Delta U\, f(y/\delta)$$

This introduced the Cole's Law of the wake:

$$U^+ = \frac{1}{\kappa} ln\, y^+ + B + \frac{2\Pi}{\kappa}\, f(y/\delta)$$

Where Π is the wake strength parameter; a non-dimensional quantity with a value depends on the flow.

3.4 TBL Experiments SET1

The first set of experiments was carried out as a preliminary evaluation of the proposed technique as well as for identifying the main parameters and major challenges. In this set of experiments (SET1) the Nd-YAG laser (Laser 1) and the CW Ar+ laser (Laser 2) are used along with Imacon camera (Camera 1) to obtain PIV data both classical mode (with Laser 1) and time-resolved mode (with Laser 2) to evaluate the effect of the exposure time on the PIV measurements. Table (3.1) shows a list of the experiments in SET1. In SET1, timing of the camera shutter between each two frames (one pair of PIV) was chosen to be 400 microsecond. This value was suitable to accommodate to the velocity range in this boundary layer flow with freestream velocity of 5.5 m/s.

This set of experiments took place in the wind tunnel facility described in chapter 2 as shown in figure 3-2. The field of view was located at a distance of 2.1 meters from the beginning of the testing section of the WT. A trip wire of 1mm diameter was placed at the beginning of the testing section to insure transition to turbulence at this position. It's important to note that all the data collected for this set of experiments and for experiments in TBL in general, which is used to calculate the mean and turbulent flow quantities, were divided into subsets. These subsets are then selected in a random fashion with large Δt to avoid any statistical dependence (similar to Classical PIV acquisition).

	Nd-YAG 5.5	**CW-5.5-100-2w**	**CW-5.5-50-2w**
<U> free-stream	5.5 m/s	5.5 m/s	5.5 m/s
Flow Field Dimensions (mm^2)	68.4x55.9	70.8x36.2	70.8x36.2
Camera	Camera1	Camera1	Camera1
Laser	Laser1 (Nd-YAG)	Laser2 (CW-Ar+)	Laser2 (CW-Ar+)
Interframe (Δt)	200μs	400μs	400μs
Exposure Time	10ns	100μs	50μs
PIV Acquisition Rate	15 Hz	1000Hz	1000Hz
PIV Realizations	300	300	300

Table 3-1: SET1 Experimental Parameters

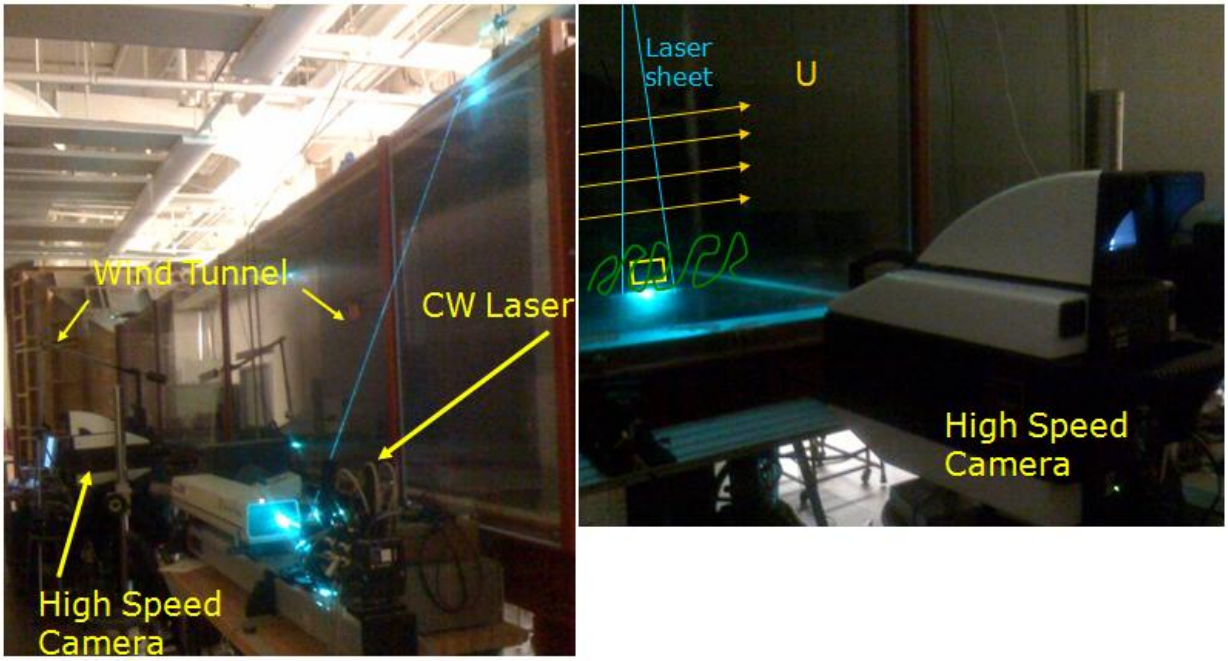

Figure 3-2: a) Experiment setup outside the wind tunnel, b) Camera1 and a drawing to show the FOV at the light sheet inside the wind tunnel

3.5 Camera1 Performance Evaluation (Imacon200)

3.5.1 Timing Strategy:

Camera 1 was built with very unique architecture (see figure 2.1), that it uses four intensified CCD's (ICCD's) placed in a polar arrangement. Each ICCD is capable of taking two consequent images with Δt as low as 5 ns, so the camera with 4 ICCD takes 8 images because of a malfunction of ICCD number four, only three ICCD's were used in the present work. Because of this camera architecture, the images were obtained in a specific order, for example Image number 1 and 4 are obtained by channel 1 (table 3.2 shows the order of the images taken by three ICCD's).

ICCD name	Channel 1	Channel 2	Channel 3
Image number	Image 1 and 4	Image 2 and 5	Image 3 and 6

Table 3-2: Channel/Image naming reference

Because of the different view for each ICCD, a parallax error always existed for images taken with different channels, this error proved to be difficult to correct for the purpose of PIV processing. So the strategy adapted here was to use two images obtained by the same CCD channel for each PIV pair. This limited the acquisition on each case to only four PIV realizations in normal condition and three in the present case; however, we were able to completely evade any error due to the parallax.

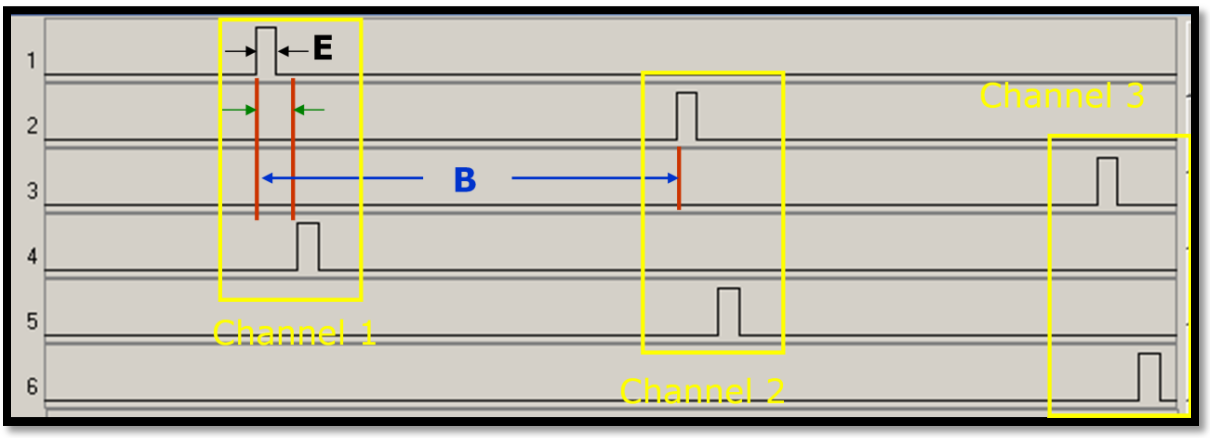

Figure 3-3 Timing of the acquisition (x-axis) against the image number(y-axis), three channels were used to obtain 3 pairs of PIV fields

In figure (3.3) Δt is the time difference between PIV image 1 and 4 (of channel 1), E is the exposure time, and B is the time between two pairs of PIV. B can be set independently of E and Δt; therefore it can be set to be zero, as in the case of the pulsed laser images to obtain exactly the same flow field images.

3.5.2 Channel Performance

All three channels were evaluated based on their performance in terms of PIV results. Initially the gain levels and pixels sensitivity are corrected using white card correction.

3.5.2.1 Pixel Sensitivity Correction:

In the white card correction, all three channels are exposed twice to two different light levels of uniformly-illuminated white board. The two exposures are set to produce an intensity gain of 25% and 75% of the maximum gain of the pixels. To achieve a uniform sensitivity for all pixels for each CCD channel, a pixel sensitivity factor is calculated for each pixel using the following formula.

$$S_{ij} = \frac{I_{ij}^1 - I_{ij}^2}{A_1 - A_2}$$

Where S_{ij} is the pixel sensitivity factor for the pixel at row i and column j, I_{ij}^1, I_{ij}^2 are the intensity value for the same pixel for the 75% and 25% intensity level images respectively, and A_1 and A_2 are the average intensity of the all the CCD channel for the 75% and 25% intensity level images respectively.

3.5.2.2 Channel Testing in Terms of PIV results for TBL:

After the initial correction was done, an actual PIV testing was needed to fully understand the limitations of camera1 to be used in the present setup. For this purpose, we used the same experimental settings as in table 3.1 (Experiment: Nd-YAG-5.5), where Nd-YAG double-head-pulsed Laser was used for illumination. In this experiment purposely, all three channels were set to take the same exact images, where B, the time between two pairs of PIV, in figure 3-3 is set to be zero and E, the exposure time, starts at the same time for 1, 2 and 3. This will produce the same exact images in both frame 1 and 2 for all three channels.

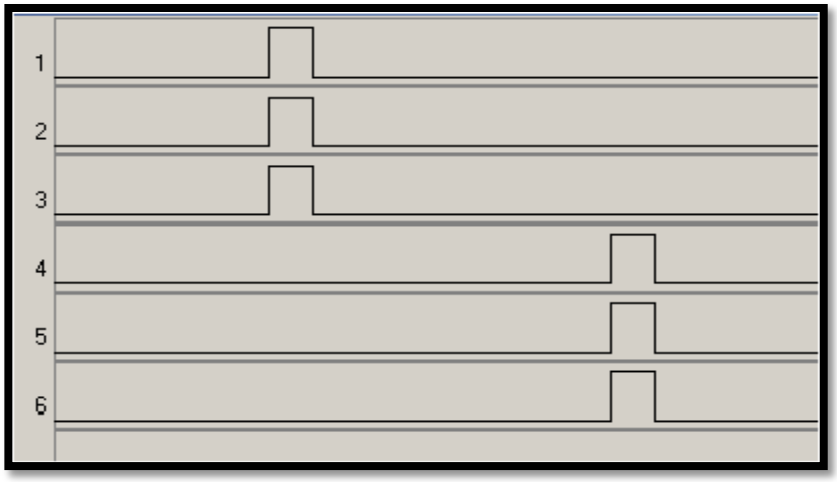

Figure 3-4: Timing for Experiment Nd-YAG-5p5_1. The timing of the images (x-axis) is set to be exactly the same for all the PIV pairs to evaluate the channels performance.

More than hundred frames were obtained, processed and averaged to produce the mean velocity profile to make a quantitative comparison between three channels (figure 3.5).

The first row in both table 3-3 and 3-4 show the PIV processing and post processing details for this case used here.

Figure 3-6a shows sample of instantaneous velocity contours obtained by the camera CCD channels 1, 2 and 3 (top down) at the exact time. In these plots the similarity of the result is clearly seen. Similarly, figure 3-6b shows the similarity of the results for the average velocity contours obtained by the three channels with the same order. This was an important indication for successful treatment of the non-uniform gain problem mentioned earlier.

Experiment Name	Interrogation area (pixels)	Spatial Resolution	Overlap	SNR Threshold
Nd-YAG-5.5	1st pass: 64x64 2ND pass: 32x32	3.4x3.4 mm^2 1.7x1.7 mm^2	50%	1.3
CW-100-5.5	1st pass: 128x128 2nd pass: 32x32	6.8x6.8 mm^2 1.7x1.7 mm^2	50%	3.0
CW-50-5.5	1st pass 128x128 2nd pass: 32x32	6.8x6.8 mm^2 1.7x1.7 mm^2	50%	3.0

Table 3-3: PIV Processing for SET1

Experiment Name	Validation Engine	Universal Validation Filter	Local Validation Filter	Vector Replacement Method
Nd-YAG-5.5	Gaussian	Standard Deviation < 3	Median 3x3	Recursive Median
CW-100-5.5	Gaussian	Standard Deviation < 3	Median 3x3	Recursive Median
CW-50-5.5	Gaussian	Standard Deviation < 3	Median 3x3	Recursive Median

Table 3-4: PIV post processing and vector validation parameters

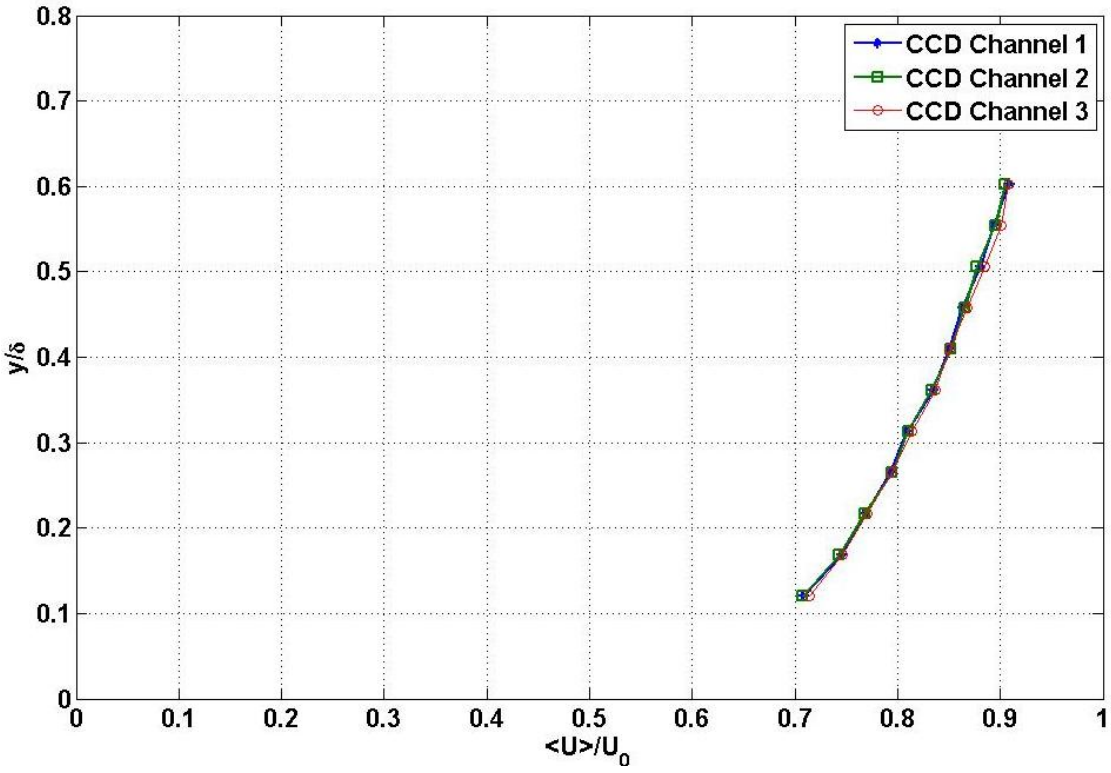

Figure 3-5: mean velocity profile for channel 1, 2 and 3 of camera 1

In figure 3.7, the velocity field from channel 1 was used as a reference field to obtain velocity residual fields. This velocity residual field is equal to the difference between channel 1 and channel 2 ($\vec{V}_{diff_a} = \vec{V}_2 - \vec{V}_1$), and the difference between channel 1 and channel 3 ($\vec{V}_{diff_b} = \vec{V}_3 - \vec{V}_1$).

In the first and second columns in figure 3.7 $\vec{V}_{diff_a}$ and $\vec{V}_{diff_b}$ are shown, respectively, first in terms of velocity vectors field, where the arrow size is x10 the residual velocity value. In the second row, a histogram of the velocity residual values are shown for $\vec{V}_{diff_a}$ and $\vec{V}_{diff_b}$, respectively, where it can be seen that more than 85% of the residual are less than one pixel in the first case ($\overrightarrow{V}_{diff_a}$) and more than 95% of these velocity residual are less than one pixel, which equal to 0.06 mm, in the second case ($\vec{V}_{diff_b}$). In the third row of the same figure, a

closer look to the residual velocity count, where it's apparent for both cases that most of the residual values are less than one half pixel in magnitude.

Figure 3.8 shows similar histograms for the residual velocity of the average field with the velocity obtained by channel 1 also used as a reference. On top is $<\vec{V}_{diff_a}>$ on the bottom $<\vec{V}_{diff_b}>$. As can be seen the error of the velocity measurements is further reduced (by one order of magnitude ≈ 0.1 pixels) in the average case. The green line in all figures shows the cumulative count of the residual velocity values.

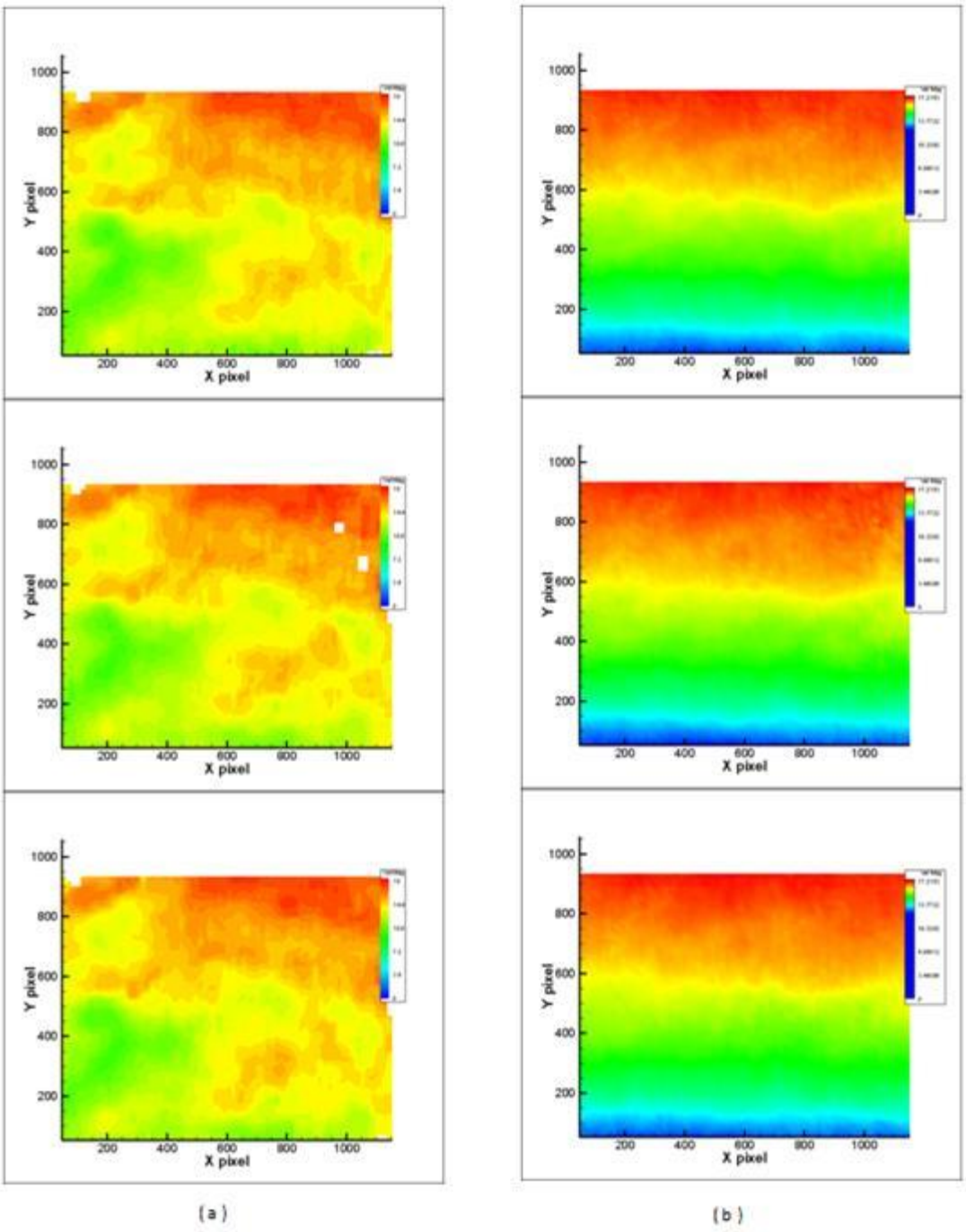

Figure 3-6: (a) instantaneous velocity field from channel 1 on top, channel 2 center and channel 3 on bottom, (b) average velocity with same order (continuous coloring)

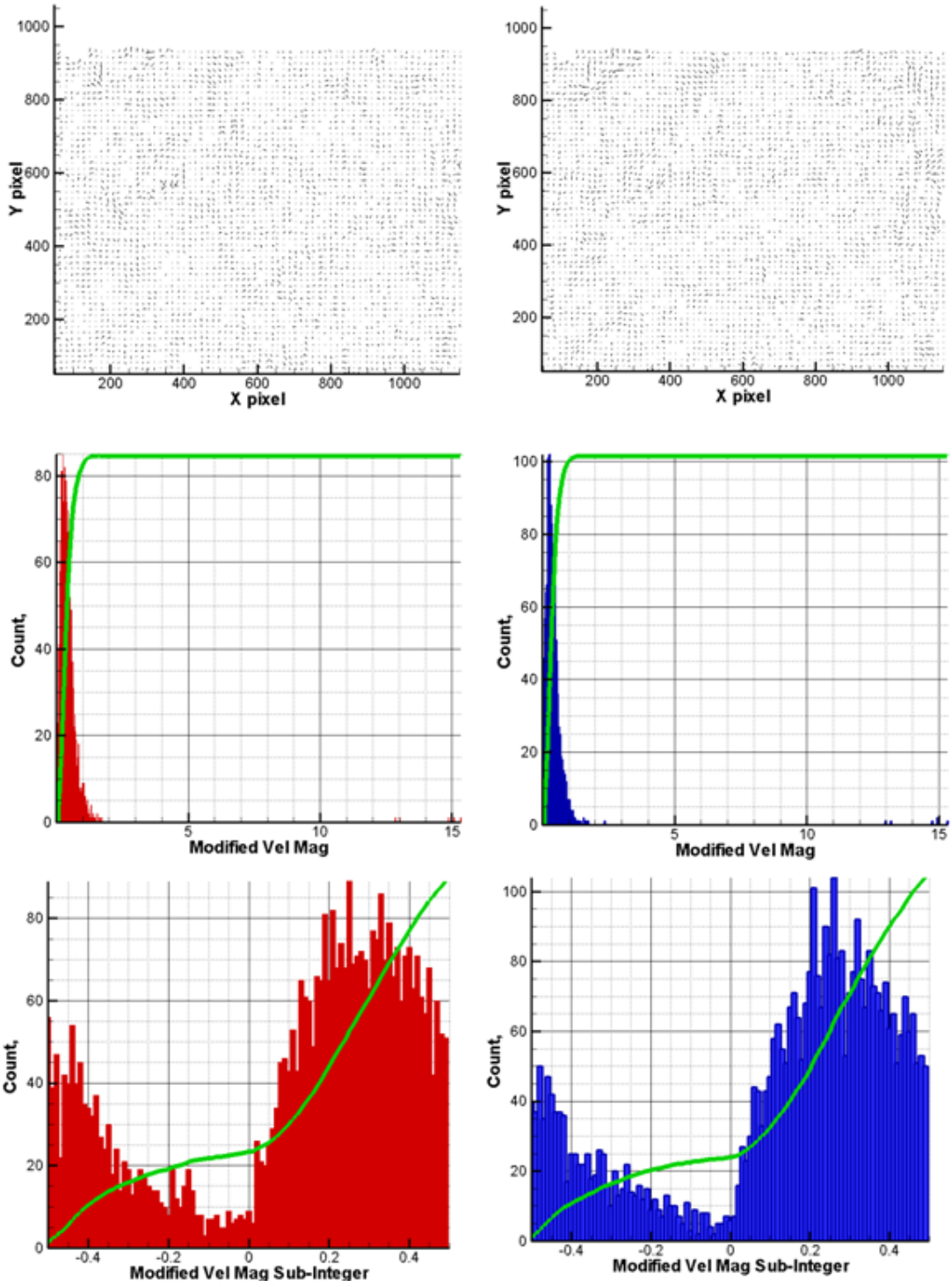

Figure 3-7: Residual of instantaneous velocity field obtained by channel 2 (left), channel 3 (right), both fields subtracted from same instantaneous velocity field obtained by channel 1's.

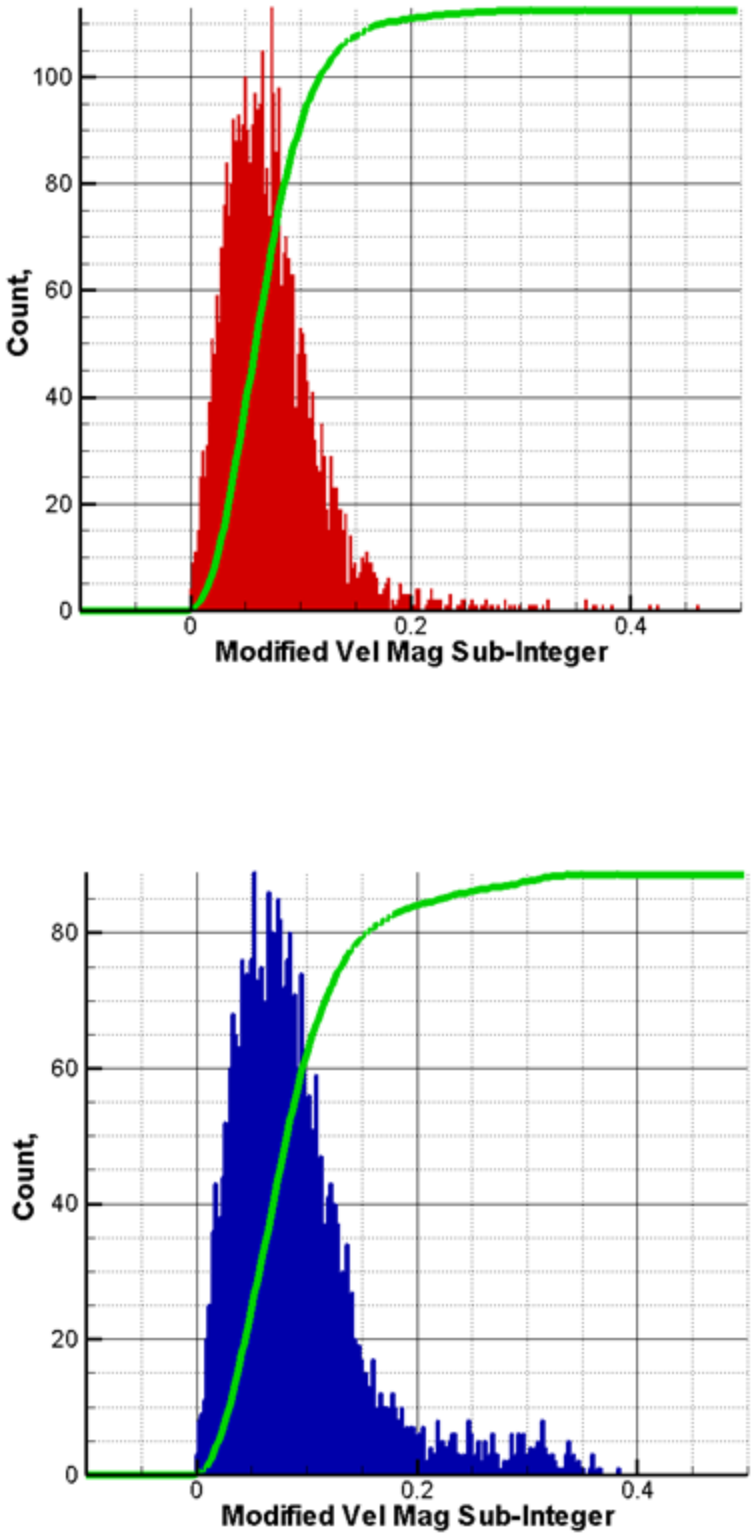

Figure: 3-8: Residual of average velocity field from channel 2 (top), channel 3 (bottom), both fields subtracted from channel 1's average velocity field.

Summary

Using the multi CCD camera (Imacon 200) can create parallax error and an error due to the difference in the gain level of CCD pixels. The former proved to be difficult to eliminate for the purpose of the PIV technique, therefore different timing strategy was adapted to acquire the PIV images pair on the same CCD channel. The later error was drastically reduced by releveling the gain level of the CCD's and readjusting the pixels gain by the pixel sensitivity factor calculated for each pixel.

The non-uniformity of light intensity in each individual CCD was corrected by applying white card correction to obtain each pixel sensitivity factor.

In the availability of high power laser (as in Nd-YAG), all three channels (CCD's) performed characteristically the same in the TBL experiment, the difference between different PIV realizations was computed to be in order of 1 pixel in instantaneous cases and 0.1 pixel in the average realization of ≈100 images.

3.6 Results of Boundary layer Experiments SET1

In this section, we will discuss the results of SET1 experiments. These experiments are carried out to investigate the effect of the exposure time, used in the Laser1 (AR+ CW laser) cases, on the PIV results. This was achieved by comparing the results of the Nd-YAG laser discussed in the previous section to the results obtained using the CW laser and the same camera1 (Imacon 200). The first case the exposure time was < 10 ns (Nd-YAG laser pulse duration), the second and the third case were obtained with the CW laser for 50 μs and 100 μs exposure time. Summary of the PIV processing and post processing for SET1 experiments are shown in table 3-3 and 3-4. It's important to note here that due the low light level produced by the Ar+ laser the flow field obtained here was for about 60% of boundary layer thickness.

First, the results are used to obtain the mean velocity values for each experiment plotted in figure 3-9. These mean velocity profiles were also compared to the universal Law of the wall (discussed in chapter 2) in the logarithmic region.

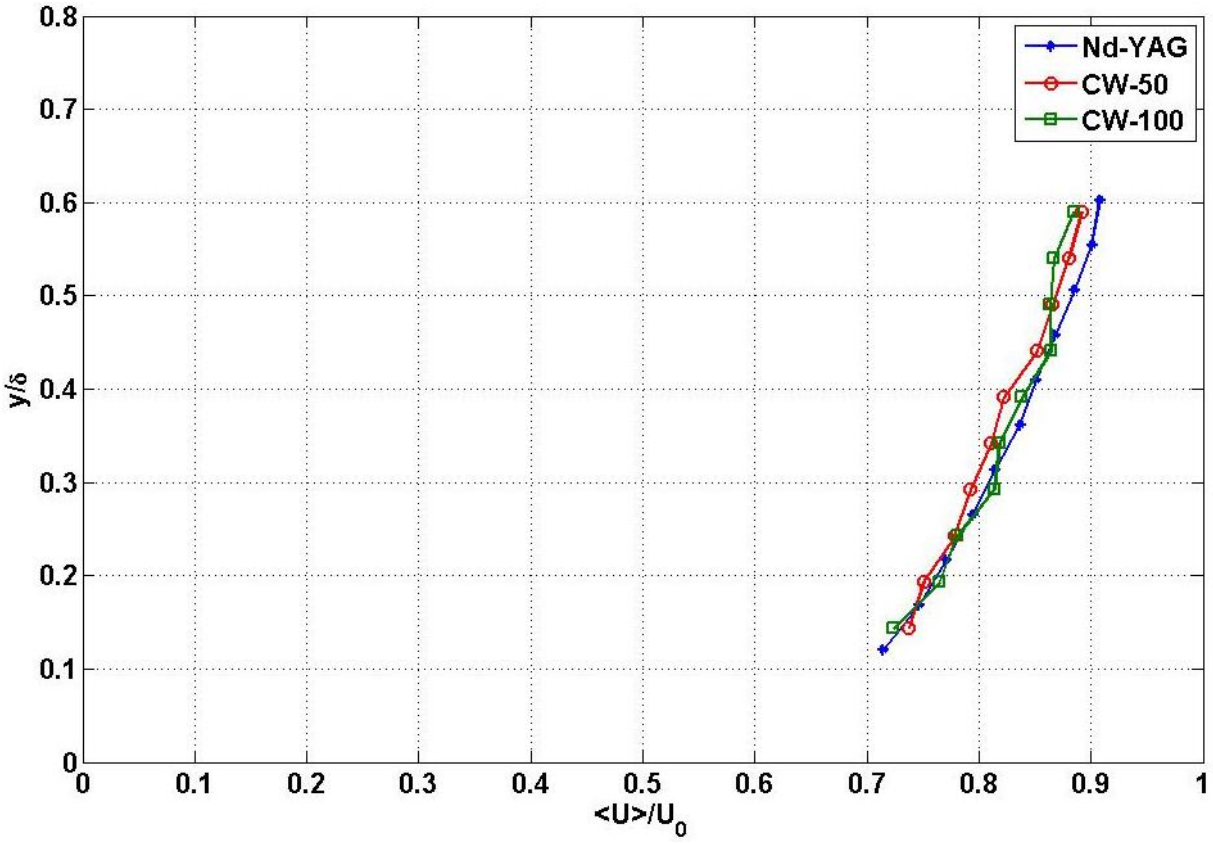

Figure 3-9: Mean Velocity Profile normalized by freestream velocity

The results obtained using Nd-YAG pulsed laser showed strong agreement with the Law of the wall in the logarithmic region (figure 3-10); however, the results obtained using the AR+ CW laser more scattering in this region. It's difficult to identify the exact the reason behind this scattering, however, the most obvious reason was the low signal to noise ratio (SNR) seen in all the images. The low SNR was direct result of the low light power of the 2 watt AR+ laser. The mean flow results was seen to have better agreement and less scattering when we used 100 us exposure time compared to the 50 us exposure time.

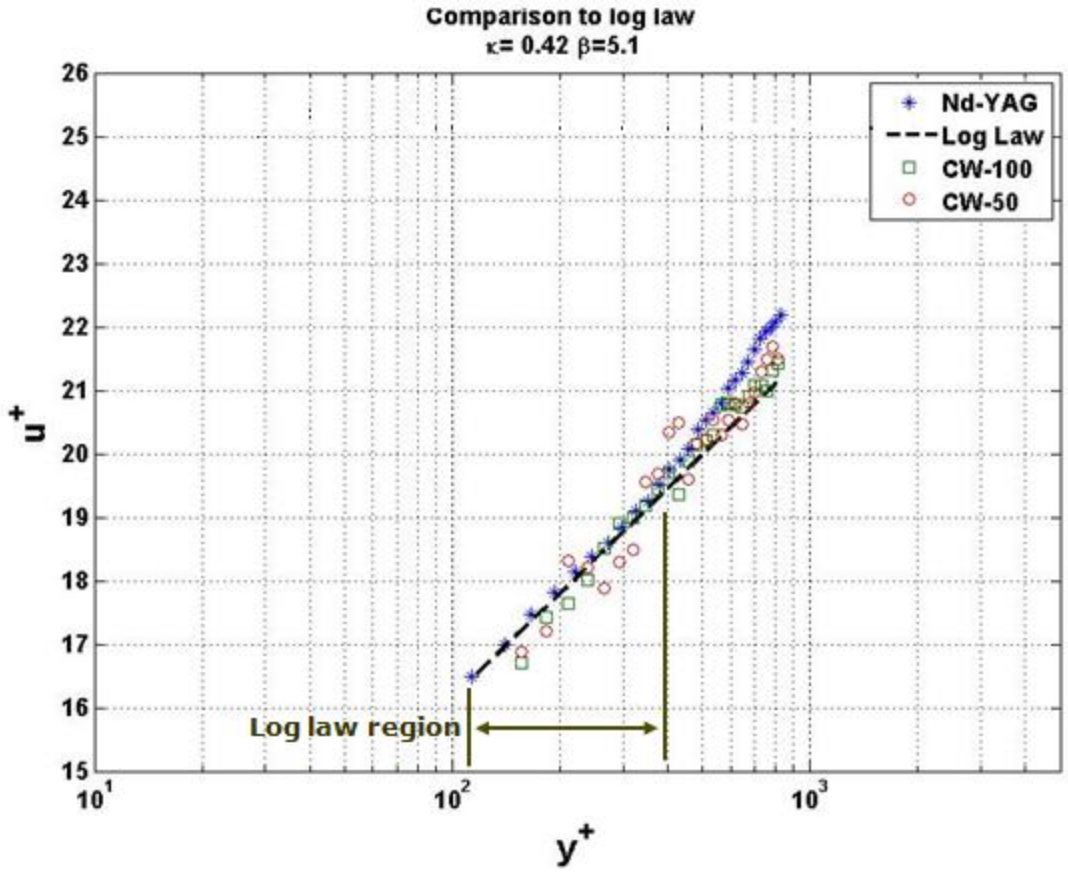

Figure 3-10: comparison to Universal Log Law

It's important to mention here that the threshold for the SNR[2] used for all the long exposure time cases PIV processing to avoid a large number of spurious vectors is set to 3. This very high SNR affected the vector count in each PIV realization; figure 3-11 shows the drop in the vector count for 300 PIV realizations in all three experiments.

The vector count shown in figure 3-11 was an indication of the quality of the instantaneous PIV that has a particular importance for this technique. The quality of the instantaneous images when the CW laser was used was drastically reduced in the case of 50 us exposure time, and was moderate but also low in the case of 100 us exposure time, in contrary, the pulsed laser case had a very high realization ratio.

[2] SNR in PIV processing defined by R. Adrian to be the ratio of the maximum correlation to the second highest correlation peak, It's recommended for the value to be 1.3 (Keane et. al 1990)

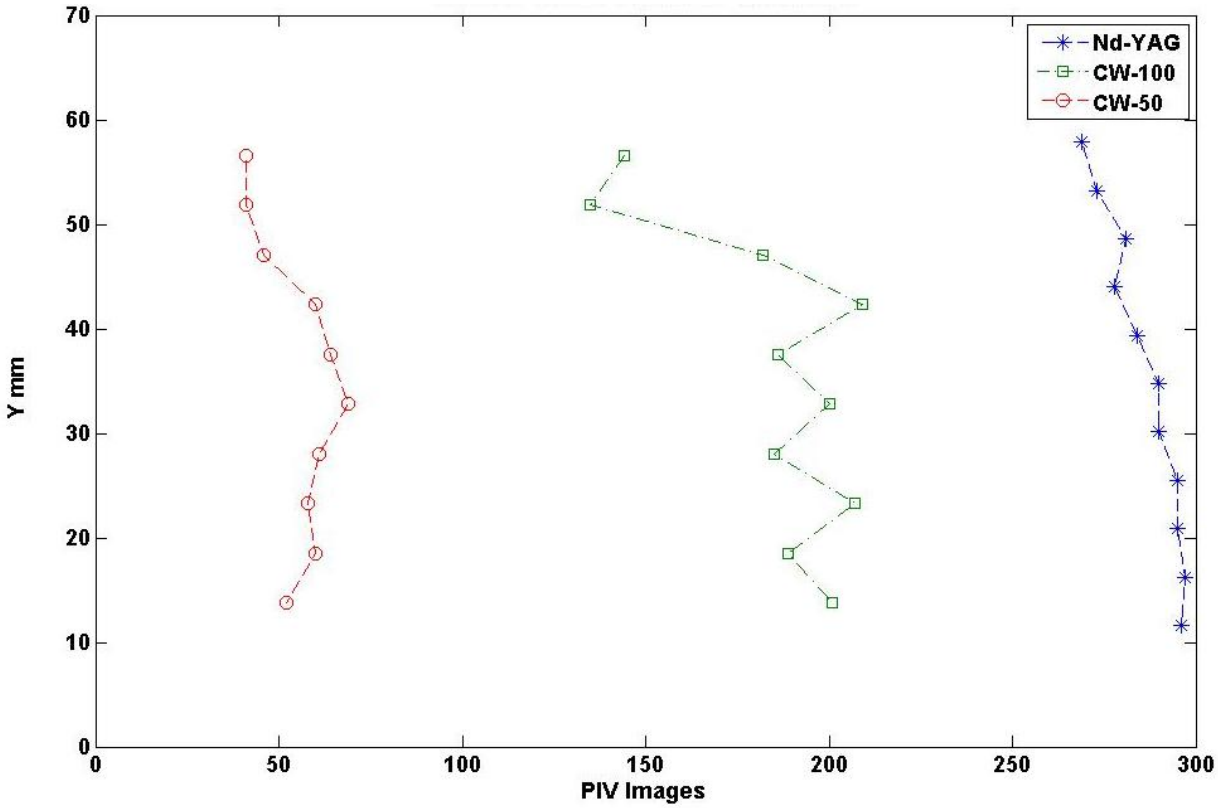

Figure 3-11: Valid PIV Vector-count out of 300 PIV realizations)

The PIV results can also be evaluated by comparing turbulence quantities such as Reynolds stress and u_{rms} results to the results from the literature. It is important to mention here that because of the low count of the overall vectors in the 50 us exposure time case; it is unreliable to compute the statistical averages of the turbulence quantities.

Figure 3.12 shows the profile of Reynolds shear stress $-\rho\overline{uv}$ normalized by the mean wall shear stress ρu_τ^2 plotted against the distance from the wall (y^+) in inner layer scaling. In figure 3-13 shown u_{rms} squared normalized by the friction velocity (u_τ) squared, the magnitude of the quantities in the Nd-YAG case show good agreement with Honkan & Andreopoulos 1997, but large scattering is seen in the CW-100 case.

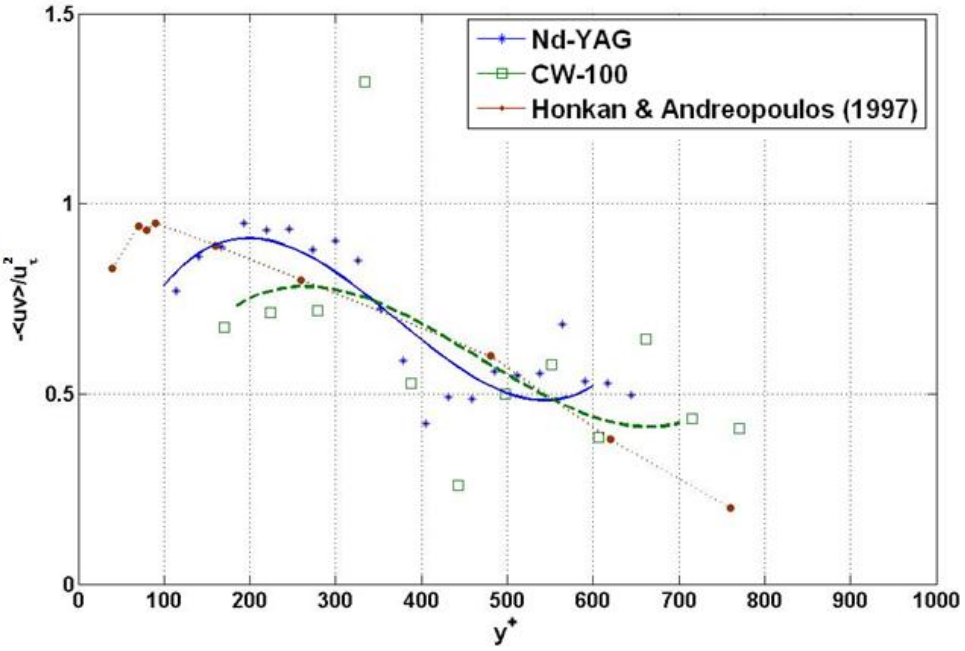

Figure 3-12: Reynolds shear stress normalized by the wall shear stress

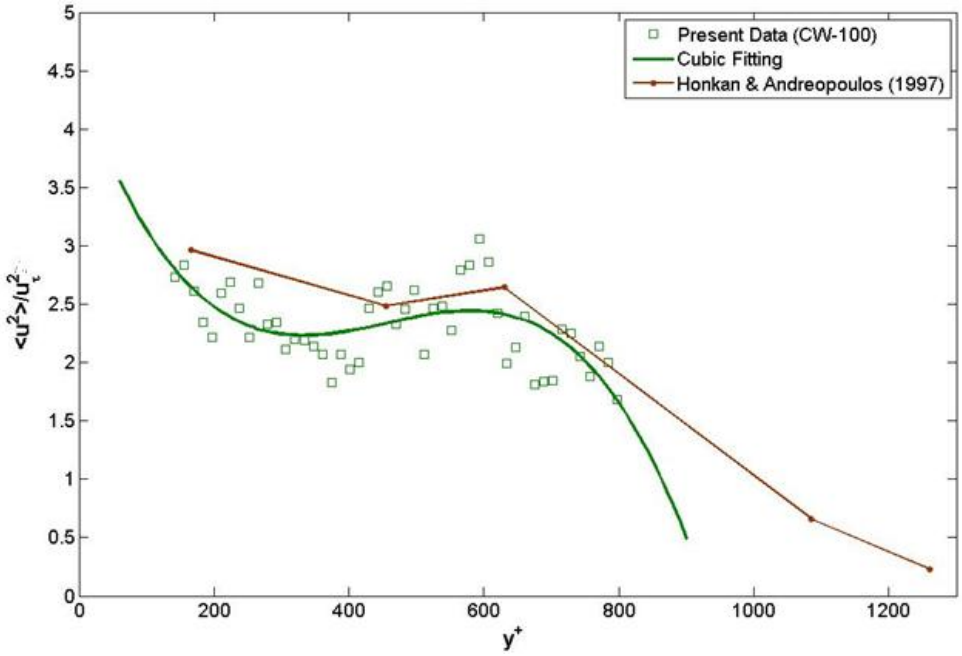

Figure 3-13: u_{rms} squared normalized by the friction velocity squared against wall units

Summary

- Experiments SET1 were carried out to evaluate PIV with CW laser and compare it to classical PIV with Nd-YAG laser.

- The mean velocity values obey logarithmic profile in the log law region. The 50us-exposure images produced much fewer validated vector counts compared to the 100us-exposure case.
- Turbulence quantities in the CW-100 case produced considerably good values in magnitude with strong scattering around the trend seen in other results, which indicated low accuracy compared to the classical PIV case.
- Laser light was scarce in both CW-cases, which limited the spatial resolution, PIV vector count, the FOV size, and the dynamic range of the velocities to be measured.

3.7 TBL Experiments SET2

In this section, a significant upgrade was carried out to the equipment. Both main components of the technique camera1 was replaced by phantom v710 (Camera2) and laser 2 was also replaced by CW Diode laser (Laser 3). Summary of both components specification listed in tables 2.1 & 2.2.

The new laser is a green diode laser with power of 5.5 watts, which is more than double what was used in Laser2 (2 Watt) that allows for less constraints in the experimental setting in terms of speed flow, FOV size and also reduce the exposure time needed for higher quality PIV results.

The major advantage of the new camera was to be able to acquire significantly larger sequence of images (up to 32,000 images verses 8 images in camera1). One main concern was to be taken into consideration is the change of the camera chip technology from CCD to CMOS. The early CMOS-chip based cameras generally produced higher level of noise compared to CCD-chip based cameras. However, this concern was proven to be insignificant from the data taken on the same wind tunnel facility during a presale testing for the camera. The advancement in the CMOS

chip technology has substantially reduced the noise level in the CMOS cameras, which made it especially compatible to PIV techniques, whereas in our case the light signal is low, so it's imperative to use a camera with low noise level.

3.7.1 Experiments Description

In these experiments, Velocity measurements in TBL were to be carried out in the same wind tunnel facility. This set of experiments took place at 1 meter from the beginning of the testing section (further upstream from SET1). Two different velocities were used in the wind tunnel 5.5m/s and 11m/s. In these experiments the data where acquired at three different exposure time in each case to evaluate its effect on the final PIV results. Table 3-5 lists the specifications of SET2 experiments.

Exp. Name	CW-5.5-150-5w	CW-5.5-100-5w	CW-5.5-50-5w	CW-11-150-5w	CW-11-100-5w	CW-11-50-5w
U_∞	5.5 m/s	5.5 m/s	5.5m/s	11m/s	11m/s	11m/s
FOV (mm^2)	100Wx115H					
Magnification	0.12					
Camera	Camera2 (Phantom v710) 1280x800 pixels					
Laser	Laser3(<5.5Watt-CW-Diode)					
Δt	200μs					
Exposure Time	150μs	100μs	50μs	150μs	100μs	50μs
PIV Acquisition Rate	5kHz					
PIV Realizations	500	649	757	500	500	500
Camera Lens	85mm					
f#	1.4					

Table 3-5: Flow parameters and experimental settings for SET2

In SET2, the focus was given to optimize the setting and the components to obtain high quality images, considering the limited light energy of the CW laser. Some practical considerations were taken that improved the condition of the light scarcity such as:

- The higher laser power.
- The use of faster camera lens with f number (*f #*) of 1.4. This allowed for the camera sensor to receive a considerably more light than in *f#* 2.8-lens case (for the same focal lens the amount of light gained is inversely proportion to the square of the *f#* ratio).
- Taking background images and subtracted from flow images has drastically decreased the noise in the PIV images.
- Small tilting of the camera sensor plane with respect to the flow has decreased flare produced by the wall reflection in the images, which shown in figure 3-14; therefore maximize the correlation peak for vectors close to the wall. This tilt should be small enough so that the entire FOV stays in focus, and also not to create a large perspective effect.

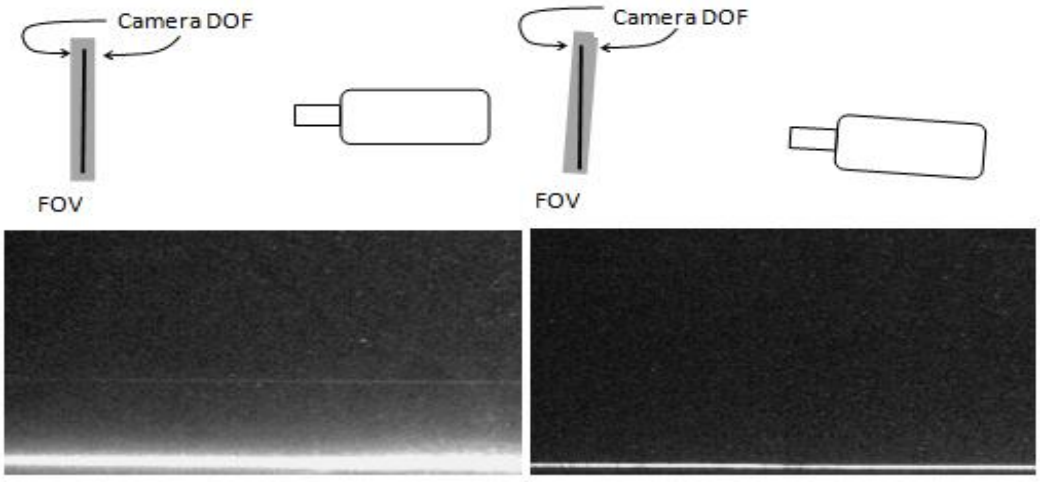

Figure 3-14: Small tilt in camera plane can reduce the strong flare from the wall reflection

3.7.2 PIV Processing of SET2 Experiments:

Table (3-6) and (3-7) show the processing parameters of all PIV (more detailed information about PIV processing used here is given in Appendix A). The processing was done using Insight 3G V9.1 software from TSI Inc. Post processing was implemented using the same software in addition to Matlab R2009a and Tecplot V10.0, some preprocessing was done using Matlab R2009a and ImageJ 1.38x.

Experiment Name	Interrogation area (pixels)	Spatial Resolution (mm^2)	Overlap	SNR Threshold
CW-5.5-50	1^{st} pass: 32x32 2^{ND} pass: 16x16	2.48x2.48	50%	1.5
CW-5.5-100	1^{st} pass: 32x32 2^{nd} pass: 16x16	2.48x2.48	50%	1.3
CW-5.5-150	1^{st} pass 32x32 2^{nd} pass: 16x16	2.48x2.48	50%	1.3
CW-5.5-50	1^{st} pass: 32x32 2^{ND} pass: 16x16	2.48x2.48	50%	1.5
CW-5.5-50	1^{st} pass: 32x32 2^{ND} pass: 16x16	2.48x2.48	50%	1.5
CW-5.5-50	1^{st} pass: 32x32 2^{ND} pass: 16x16	2.48x2.48	50%	1.5

Table 3-6: PIV processing parameters used in SET2 experiments

Experiment Name	Validation Engine	Universal Validation Filter	Local Validation Filter	Vector Replacement Method
Nd-YAG-5.5	Gaussian	Standard Deviation < 3	Median 3x3	Recursive Median
CW-100-5.5	Gaussian	Standard Deviation < 3	Median 3x3	Recursive Median
CW-50-5.5	Gaussian	Standard Deviation < 3	Median 3x3	Recursive Median

Table 3-7: PIV post processing and vector validation parameters

All the PIV experiments were subjected to background image subtraction to reduce the noise in the images due to the background light scattered caused by the laser illumination. These background images were acquired using the same exposure time (i.e. the background images for 50us exposure time experiments were also acquired with exposure time of 50us). In all cases Multi-pass processing and image deformation method was used for processing with SNR that varies from 1.2 to 1.5.

In post processing, threshold value of three times the standard deviation was universally applied for vector validation over the entire field. A median filter with tolerance of 2 pixels was used for local validation with the neighboring 3x3 vectors. Also, a median recursive filling was used to fill invalid vectors only if the valid second peak failed the post processing tests. And finally the interpolation was applied to for fill the vacant velocity vectors position bases on the mean value of the neighboring vectors. Figure 3-15 shows typical processing flow chart used for these experiments.

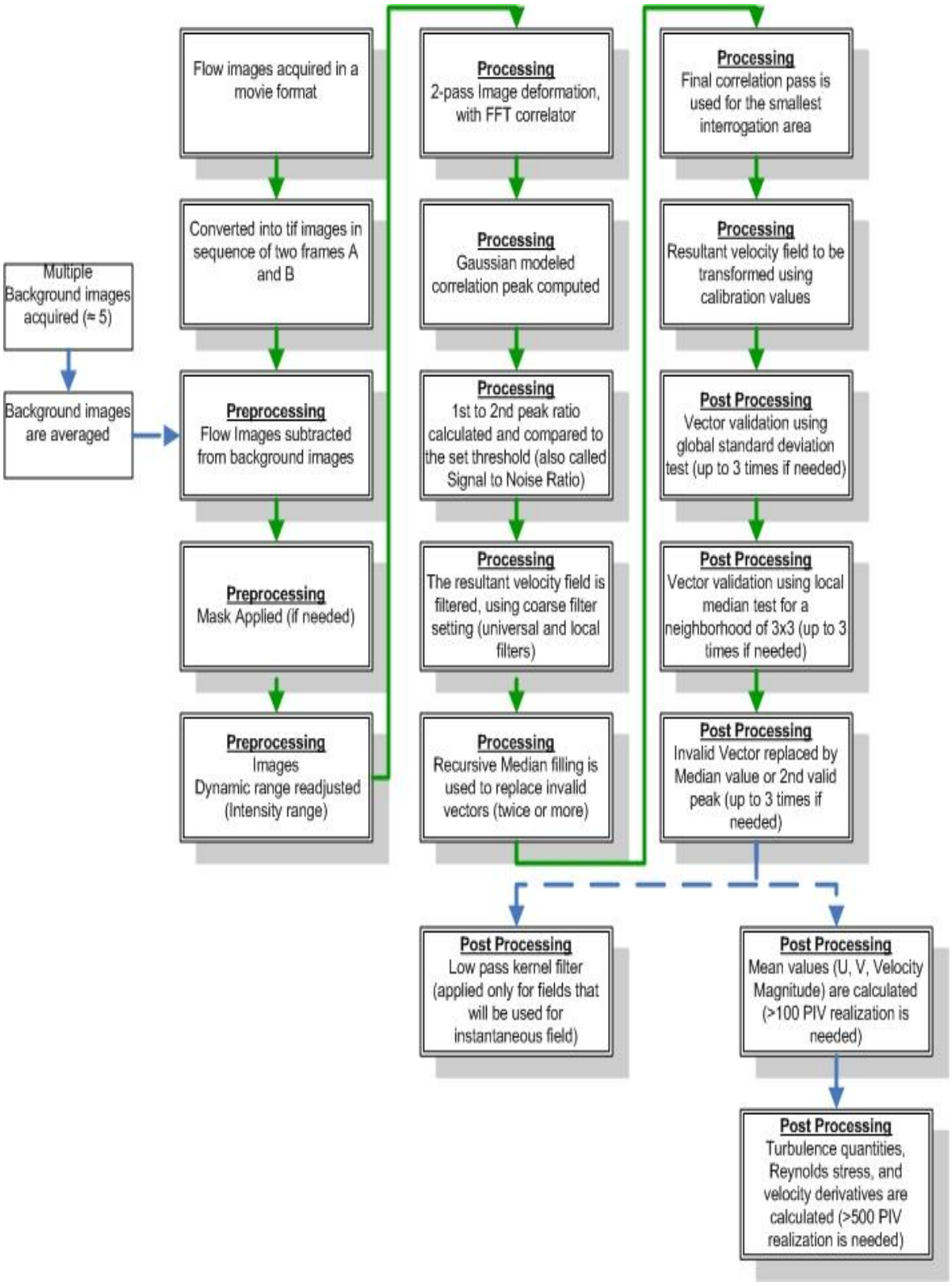

Figure 3-15: Flow Chart for typical PIV Processing used

3.8.3 Results of SET2 Experiment:

All experiments in SET2 took place at the same location in the test section of the wind tunnel at two different Reynolds numbers. Table 3-8 shows the bulk flow parameters of the incoming TBL.

	Freestream Velocity	BL Thickness	Momentum Thickness	Shape factor	Friction Velocity	Friction Coeff.	
Exp. Name	U_∞(m/s)	δ (mm)	θ (mm)	δ^*/θ	u_τ (m/s)	C_f	Re_θ
CW-5.5-***	5.4	53	5.3	7.4/5.3	0.221	0.0033	1910
CW-11-***	10.7	47	4.7	5.4/4.7	0.398	0.0026	3330

Table 3-8: bulk flow parameters (SET2)

In figure (3-16a) and (3-16b), the mean velocity profile obtained in the experiments with freestream velocity of 5.5m/s and 11m/s, respectively, is shown for three different exposure time cases (50μs, 100μs, and 150μs). In figure (3-17), the mean velocity is compared to the universal Law of the wall in the logarithmic region. The friction velocity u_τ is found to be equal to 0.223 m/s for freestream velocity of 5.5 m/s experiments, and equal to 0.398 m/s for cases with freestream velocity of 11m/s.

As can be seen from the mean profile for the low Reynolds number case the mean profile seemed identical, but it did not appear the same way in the higher Reynolds number case, where small discrepancies can be seen with the change of the exposure time.

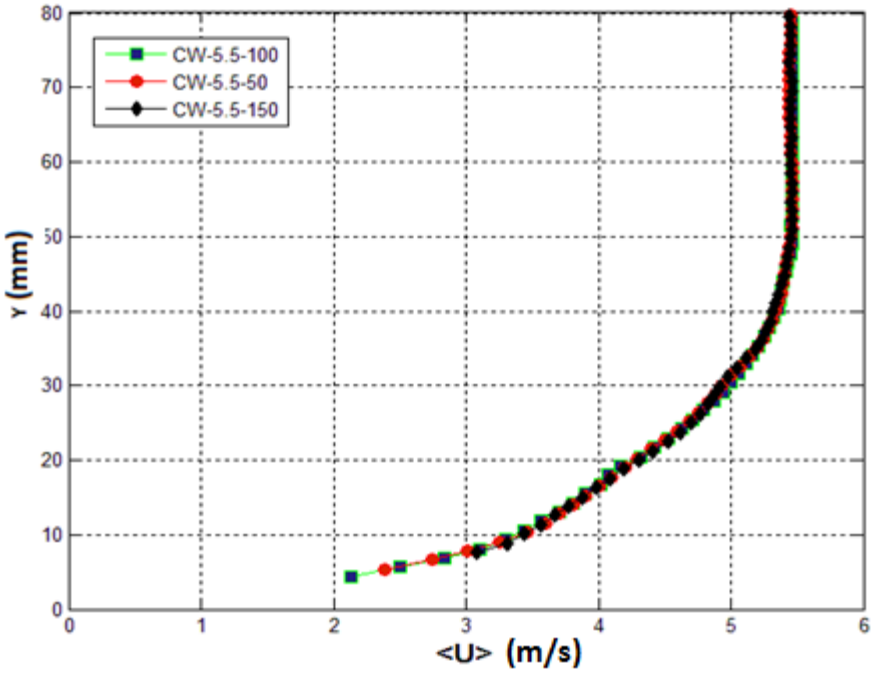

(a)

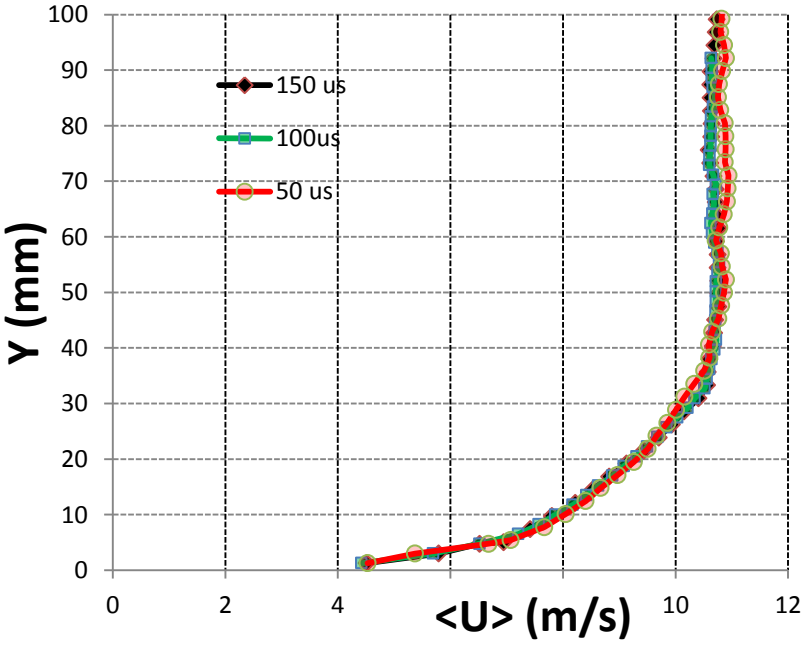

(b)

Figure 3-16: U (x-component velocity) profile against Y (wall normal direction) for (a) Re_0 = 1910, (b) Re_0 = 3330

In figures (3-16a) & (3-16b), the flow mean velocities in all cases converged to the same values, however, in the 150μs exposure time case, more PIV realizations were needed for the mean value to converge to the same value seen in the other two cases (50μs and 100 μs). It's important also to note that in the case of 150us exposure time at 11m/s, a strong particle streaking was noticeable in the raw images (more analysis on streaking and particle imaging will be discussed later in this chapter). This streaking would have an effect on the uncertainty of the correlation displacement value, and therefore on the velocity value, in addition to the true location of the velocity vector.

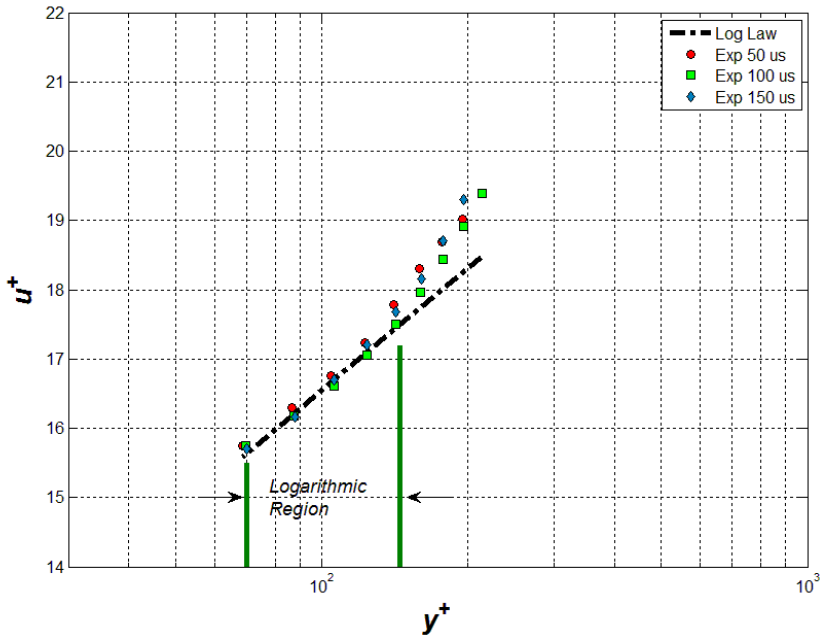

Figure 3-17: Comparison of TBL results to the log law in the logarithmic region (freestream velocity= 5.5 m/s)

One practical method to evaluate the results, considering all the different elements that affect the system, is to obtain statistical quantities of velocity fluctuations (turbulence quantities) and compare them to results from the literature, because these quantities are more susceptible to small precision error. The fluctuating velocity components, defined as:

$u'(y,t) = U(y,t) - < U(y,t) > and\ v'(y,t) = V(y,t) - < V(y,t) >$, are computed, and normalized by the friction velocity u_τ and plotted against the wall normal distance normalized by the boundary layer thickness δ, and then compare them to similar literature results of turbulent boundary layer data.

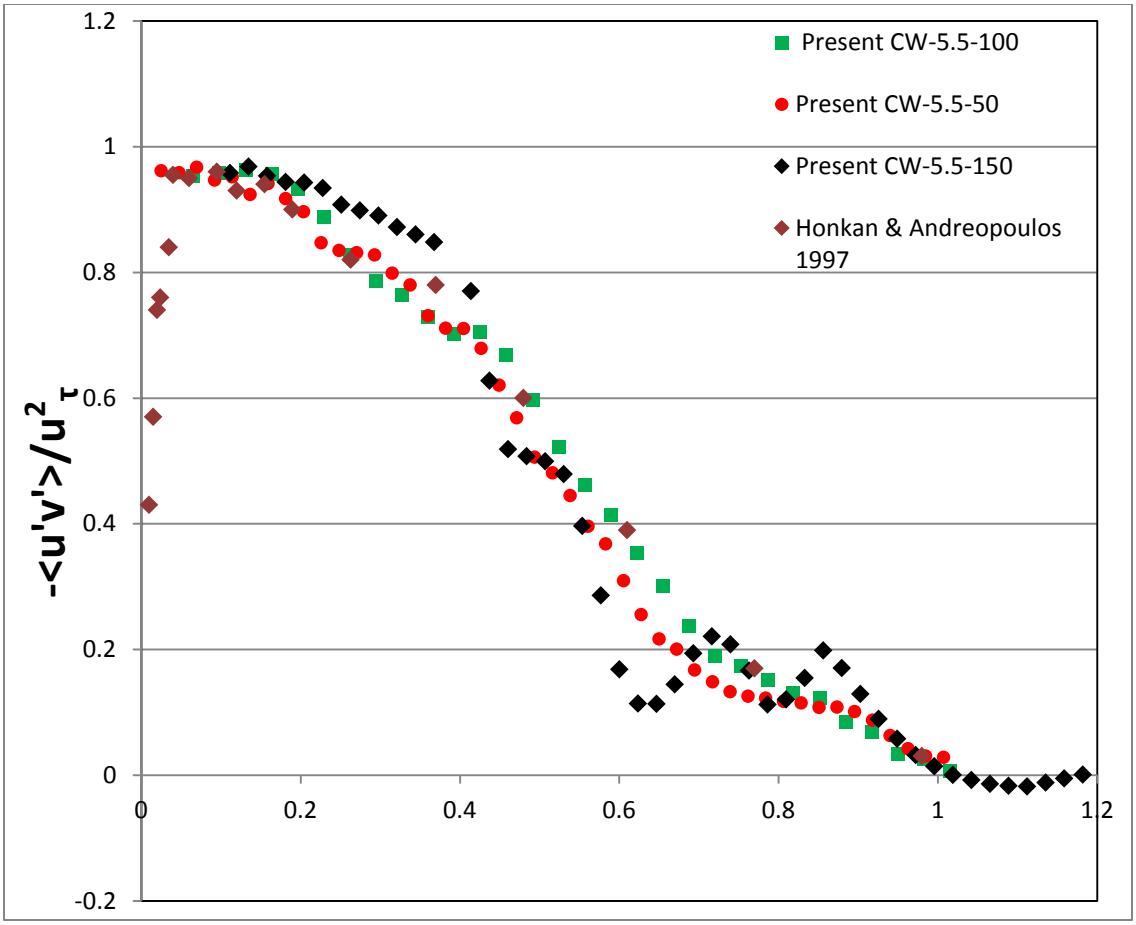

Figure 3-18: Reynolds stress -ρ<u'v'> normalized by the wall stress ρu_τ^2 against wall normal distance normalized by δ (boundary layer thickness) (U_∞=5.5m/s)

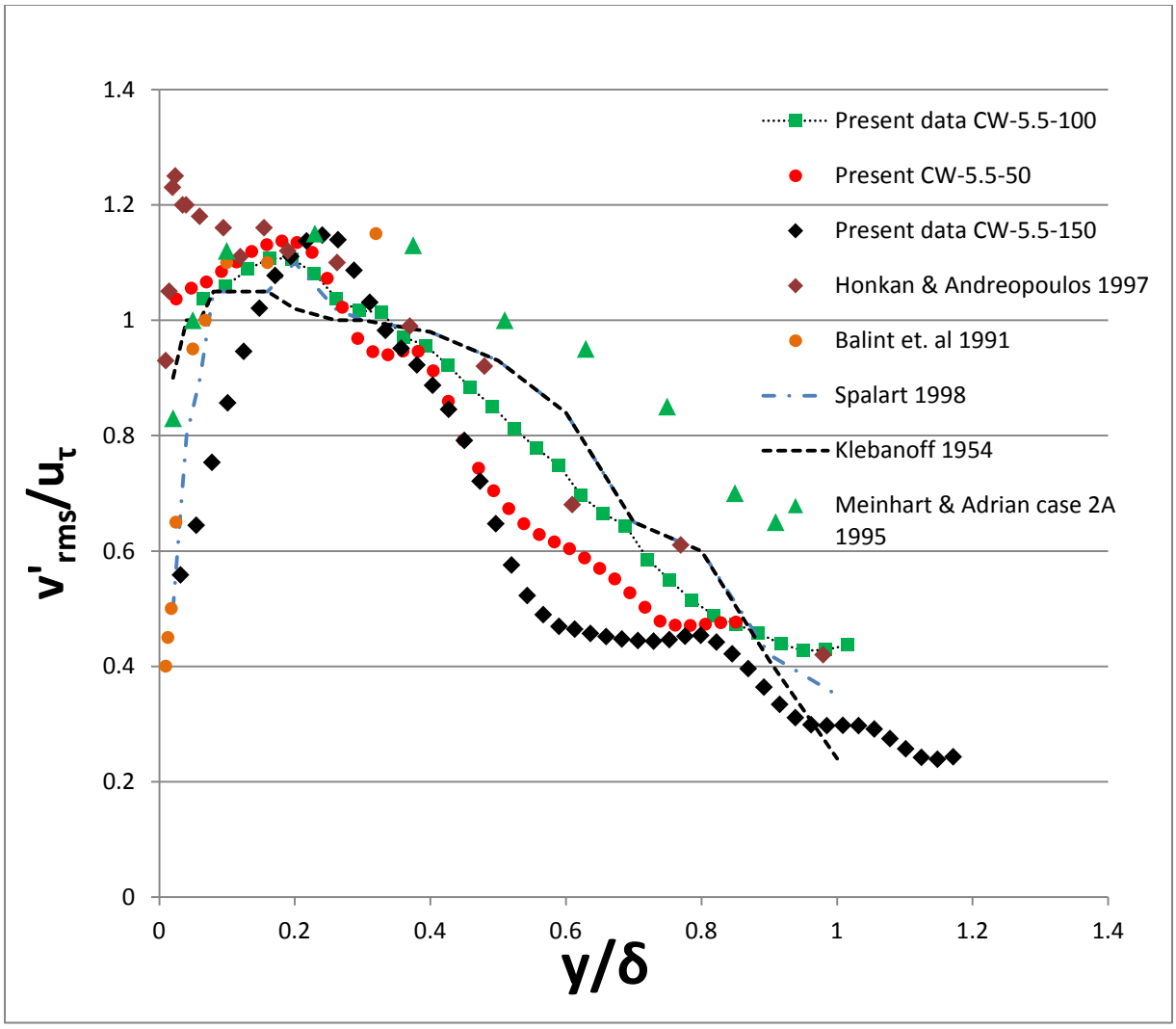

Figure 3-19: v_{rms} squared normalized by the friction velocity squared against wall normal distance normalized by δ (boundary layer thickness), (U_∞=5.5m/s)

Figure (3-18), (3-19) and (3-20) shows the Reynolds stress $\rho\langle\overline{u'v'}\rangle$ normalized by the wall shear stress ρu_τ^2, rms velocity u' and v' normalized by the friction velocity u_τ, respectively, plotted against the distance from the wall (y) normalized by the boundary layer thickness (δ). These results, which represent the 5.5 m/s freestream experiments, are compared to other results from Honkan and Andreopoulos 1997 (hotwire on the same WT facility) and other literature results (Balint et al. 1997 (hotwire), Spalart 1988 (DNS), Klebanoff 1954, Meinhart and Adrian 1995 (PIV)). In these plots strong agreement is seen with the data in the literature in all the 100us

exposure time cases. Also good agreement is seen for the 50us case where the light signal is weaker in particular close to the wall as the wall flare reduced the SNR for this region. However, some deviations in these rms values are seen in the case of 150 us, which are directly result of the increasing particle streaking due to the larger exposure time. Tthese deviations are more pronounced in the outer layer where the flow/ particles velocity are larger.

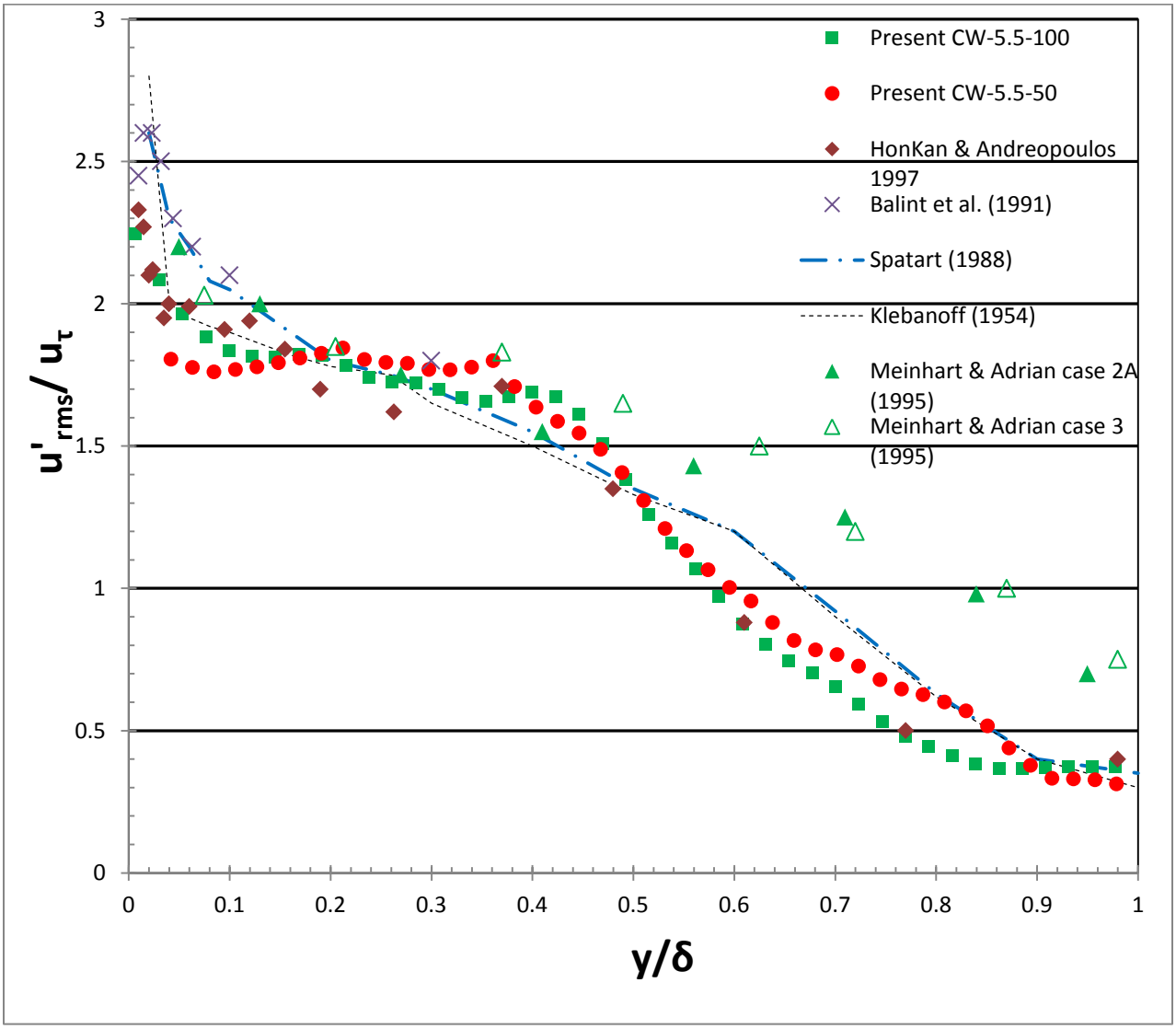

Figure 3-20: u_{rms} squared normalized by the friction velocity squared against wall normal distance normalized by δ (boundary layer thickness) (U_∞=5.5m/s)

Figure (3-21) shows the fluctuating velocity u' normalized by the friction velocity u_τ in the case of 11m/s freestream velocity. Despite the fact that the trend is preserved, it is noticed that the magnitudes u'/u_τ show overestimation compared to the literature, this overestimation is on average 20% inside the boundary layer, and it appears larger at the edge of the boundary layer. In for the case of 50 us the error on the results, this difference appeared to be less than the case of 100us exposure time.

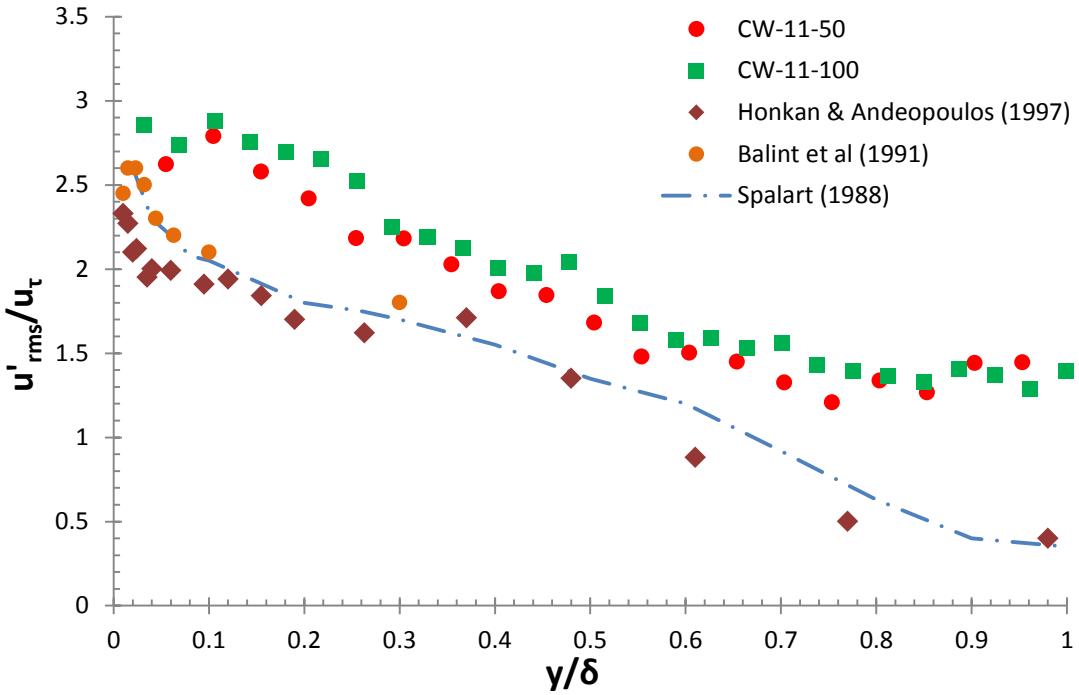

Figure 3-21: u_{rms} squared normalized by the friction velocity squared against wall normal distance normalized by δ (boundary layer thickness), (U_∞=11m/s)

Figure (3-22) shows the fluctuating velocity v' normalized by the friction velocity for the same freestream case of 11m/s. As it can be seen in the figure that the trend was also preserved in this case, but the magnitude shows an underestimation compared to the results from literature. The underestimation in v' results are seen to be larger than u' results, but they show better convergence in at the edge of the boundary layer, perhaps due to the fact that the streaking is large in the x-direction and considerably smaller in the y-direction.

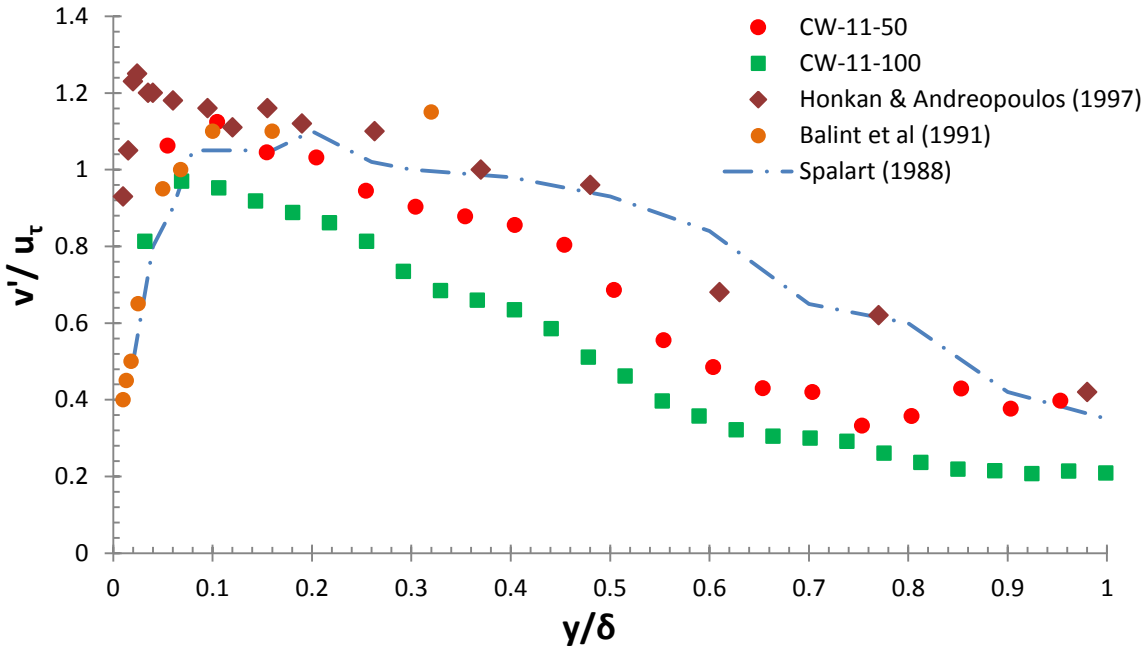

Figure 3-22: v_{rms} squared normalized by the friction velocity squared against wall normal distance normalized by δ (boundary layer thickness), (U_∞=11m/s)

3.8 Optimization of the exposure time

The duration of exposure is a major contributor to the uncertainty in measuring the displacement of the particle in TR-PIV with CW laser. A basic uncertainty analysis for the particle displacement, which is due to the duration of the exposure, is shown in table 3-9.

Figure (3-23) shows magnified regions taken from raw images, the image on the left is for 5.5m/s freestream velocity with exposure time of 50 μs and the right side image is for 11m/s freestream velocity with exposure time of 100 μs. From both images, the effect of the duration of exposure can be seen in the particle streaking in the flow direction on the right image.

Freestream Velocity	5.5m/s			11m/s		
Exposure time (μs)	50	100	150	50	100	150
Max. displacement uncertainty (mm)	0.28	0.55	0.83	0.55	1.1	1.65

Table 3-9: uncertainty (mm) based on freestream velocity and the exposure time

In this section, further investigation on the effect of the exposure time on the particle and some qualitative calculations can be used for experimental optimization of the laser light.

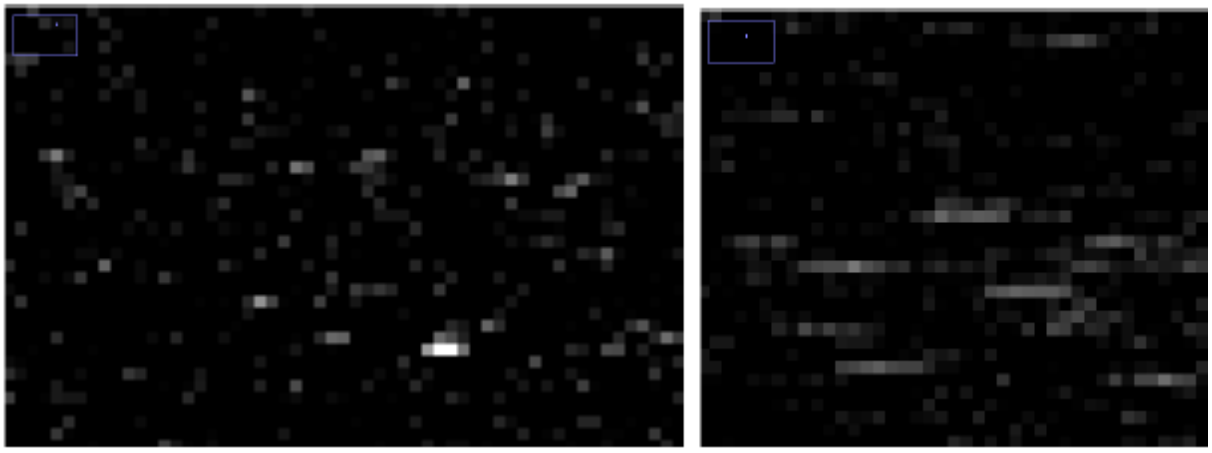

Figure 3-23: magnified regions taken from raw images, on left: particle image with 50 us exposure time and freestream velocity is 5.5 m/s, on right: exposure time used is 150 us and 11m/s freestream velocity

3.8.1 Particle Imaging:

The diameter of the particle image given approximately by the Airy function (Adrian 1985):

$$d_\tau \cong (M^2 d_p^2 + d_s^2 + d_a^2)^{1/2}$$

Where: $d_s = 2.44(1 + M)f^{\#}\lambda$ is the diffraction-limited spot diameter, M is the magnification, d_p is the finite particle diameter, and d_a is the diameter of the aberrated image, which can be neglected with the current available lens system for the non microscopic scale, and λ is the wave length of the light.

The average particle image was calculated for all exposure time (50us, 100us, and 150us) at 5.5m/s, and 11m/s freestream velocities. For these calculations a sample image with good particle distribution was selected for each case. These images were thresholded, in terms of intensity value, to limit the effect of the noise, and an average particle size was calculated for

each case. Figure (3-24) show a sample of the results shows the particle location and count number. In table (3-10) is a sample of output parameters calculated from the images, such as the location, width, length, area and circularity of each particle, where the circularity is defined here as:

Circularity = 4pi (area/perimeter^2), where a circularity value of 1.0 indicates a perfect circle. As the value approaches 0.0, it indicates an increasingly elongated polygon.

The average size of the particles and the circularity were important statistical quantities to study in this case. An increase of the statistical average of the particle size corresponds to the increase of the streaking of the particle imaging. Figure 3-25 shows this increase occurs with the increase of exposure time for both cases of freestream 5.5m/s and 11m/s. However, when the freestream velocity is doubled, the streaking effect was increased by smaller factor for all exposure times.

In figure 3-26, the effect of exposure time on the average circularity is shown for both cases. It is shown that the average circularity of the particle image is reduced with the increase of exposure time. However, the percentage of change is moderate in the case with freestream of 5.5m/s, but the average circularity of particle image is reduced to 0.5 in the higher freestream velocity of 11m/s at exposure time of 150 μs. This generally agrees with trend of the results obtained for the turbulence quantities shown previously.

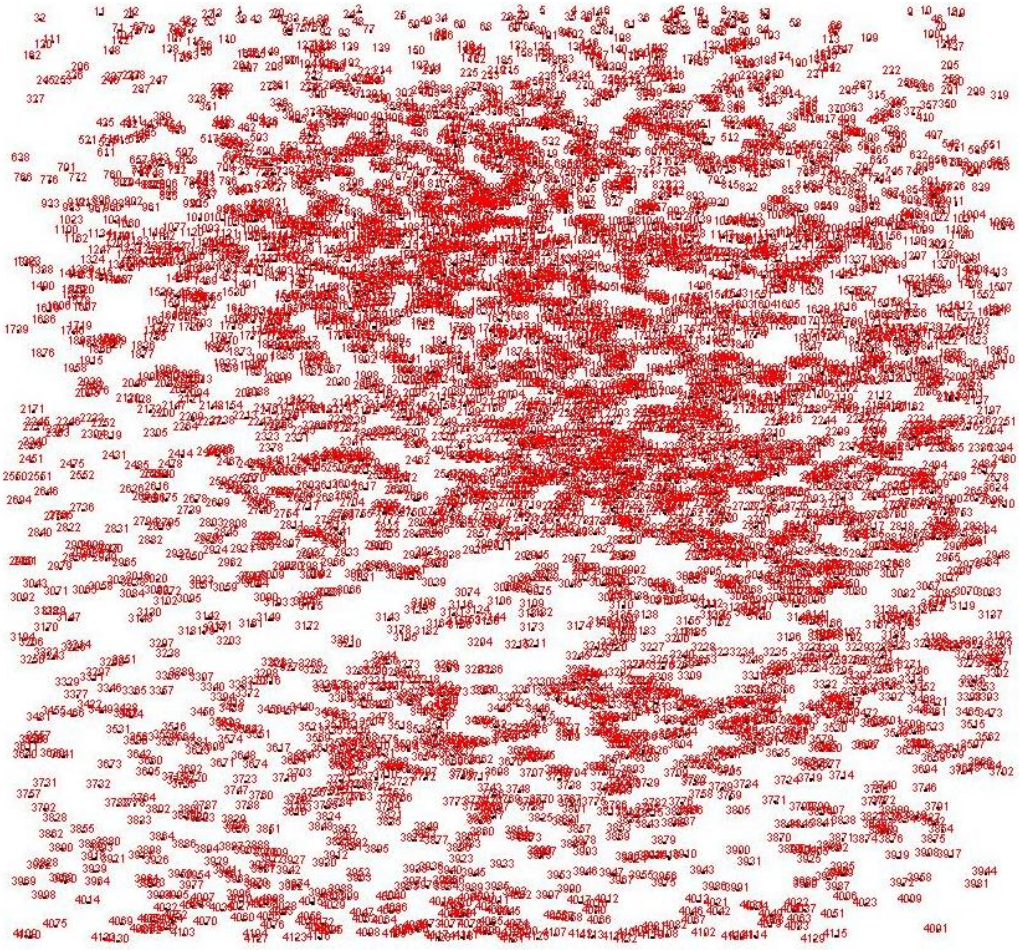

Figure 3-24: the output image after analyzing the raw PIV image, this image shows the particle location and number (created by ImageJ 1.38x by NIH

	Area	Mean	Min	Max	X	Y	XM	YM	Perim.	BX	BY	Width	Height	Circ.
1	2	255	255	255	494	14	494	14	5.657	493	13	2	2	0.785
2	3	255	255	255	590.5	13.5	590.5	13.5	6.828	589	13	3	1	0.809
3	3	255	255	255	720.5	13.5	720.5	13.5	6.828	719	13	3	1	0.809
4	2	255	255	255	763.5	14	763.5	14	4.243	763	13	1	2	1
5	2	255	255	255	738	14.5	738	14.5	4.828	737	14	2	1	1
6	2	255	255	255	790	14.5	790	14.5	4.828	789	14	2	1	1
7	3	255	255	255	850.5	14.5	850.5	14.5	6.828	849	14	3	1	0.809
8	2	255	255	255	884	14.5	884	14.5	4.828	883	14	2	1	1
9	2	255	255	255	1034	15	1034	15	5.657	1033	14	2	2	0.785
10	2	255	255	255	1047	14.5	1047	14.5	4.828	1046	14	2	1	1
11	2	255	255	255	382	15.5	382	15.5	4.828	381	15	2	1	1
12	2	255	255	255	409	15.5	409	15.5	4.828	408	15	2	1	1
13	2	255	255	255	476	16	476	16	5.657	475	15	2	2	0.785

Table 3-10: the outcome sample of results for particle image analysis (created by ImageJ 1.38x by NIH)

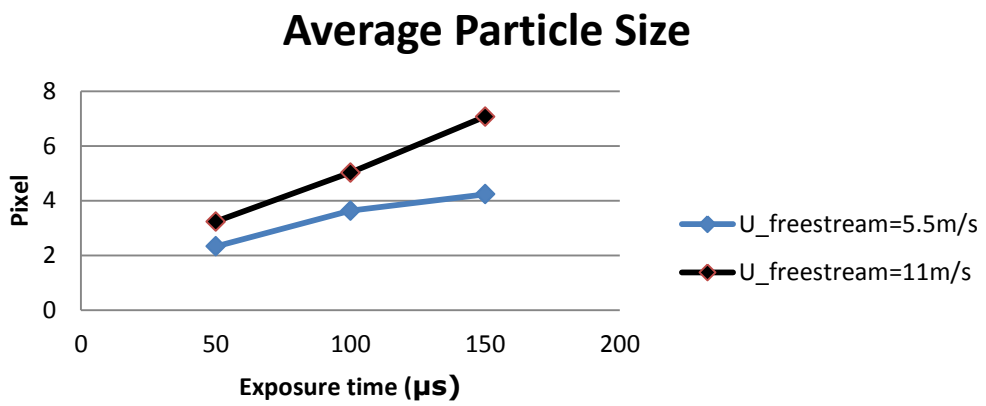

Figure 3-25: Average particle size in instantaneous images at different exposure time for two different Reynolds numbers

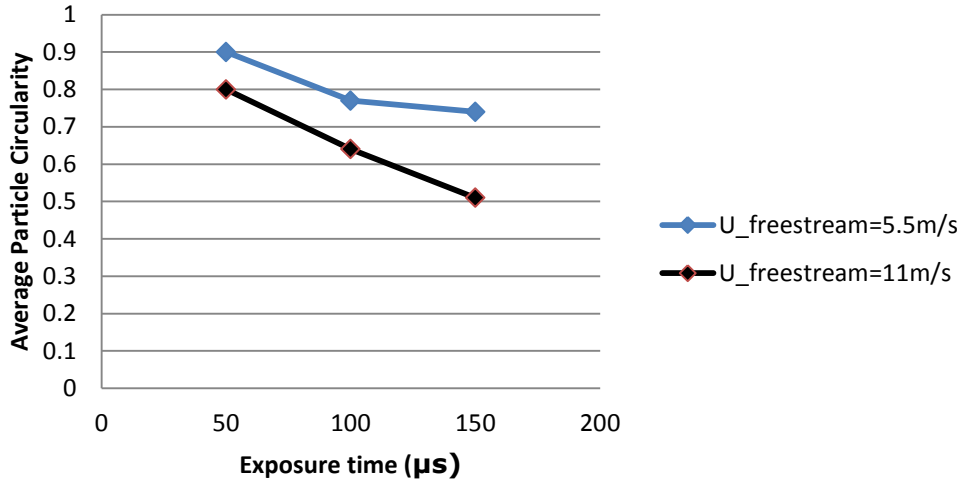

Figure 3-26: Average Particle Circularity Vs the Exposure time for two different Reynolds numbers

3.8.2 Light sheet optimization (Qualitative analysis for experimental setup)

One of the major parameter influencing the exposure time is what we refer to here as the availability of laser light. This parameter was found to be linearly proportional to the laser light power output, and inversely proportional to the laser beam diameter. A closer look to some parameter, we can develop the following calibration scaling equation.

$$P_{available} \propto \left(P_{output}, \frac{W}{L_1 + L_2}, \frac{4}{\pi d^2}, \frac{1}{t} \right)$$

P_{output}: laser output power

W: FOV width

L_1 and L_2: width of the laser sheet at the boundaries of FOV

α: laser sheet spread angle

d: Laser output beam diameter

t: Laser sheet thickness

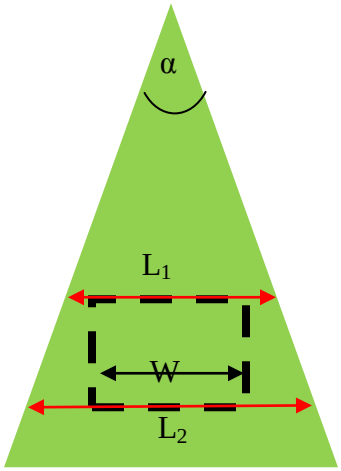

It's desirable P_{output} in the case of CW laser to always be maintained at maximum available power; however, heating surfaces might be a concern in some cases. The second part of the equation (L_1+L_2) can be optimized by choosing the appropriate cylindrical lens; however, the light in the laser sheet is not uniformly distributed. This is a result of the output beam profile, which has Gaussian profile with maximum intensity at the center. The beam diameter is fixed for each laser system, but it can be different from one system to another (i.e. d_{Laser1} =8mm, d_{Laser2}=1.4mm, d_{Laser3}=2.3mm). The optimization for the thickness can be done by choosing the right spherical lens and the location of the FOV with respect to the laser sheet optics.

Summary

- Second set of experiments (SET2) with freestream velocities of 5.5m/s and 11m/s were carried out to evaluate the techniques as higher power CW laser became available with Laser3.

- Time-averaged velocity magnitude was computed from the PIV results. All exposure time cases (50μs, 100μs and 150μs) showed similar results in 5.5m/s freestream experiments, however, small differences in the results was seen in the 11m/s freestream case.
- Statistics of velocity fluctuations, compared to the literature, showed strong agreement in the 5.5 m/s freestream case. However, with the increase of the freestream velocity to 11 m/s, bigger difference on the magnitude was seen for both 100μs and 50μs exposure time case. This difference is more pronounced at the outer edge of the boundary layer where the flow is faster, and bigger streaking effect is seen.
- Particle imaging along with laser light sheet require optimization to increase the signal quality of the raw images of PIV; some modifications in the experimental setup resulted of considerably better quality for the raw images.

Part II: Investigation of transient Force Generation on flow actuator during impulsive deployment inside TBL

Chapter 4 : Introduction

4.1 Previous Work

Flying using flapping wings became known from observations of birds and insects. One of the first attempts to implement the idea of generating thrust from flapping wings to fly was Leonardo da Vinci in 1490. Several attempts to try flying using flapping wing aerodynamics were made at the end of the 19th century (Lilienthal, 1889). However, most of these attempts had failed because of the insufficient knowledge of the physics involved to generate the required thrust. The complexity of the flow and the kinematics in such motion made it nearly impossible to understand aerodynamics with the early 19th century technologies.

Early effort to explain the physics of flapping wings was made by Knoller (1909) and Betz (1912). They noted that the flapping motion can produce both thrust and lift forces of the aerodynamic force.

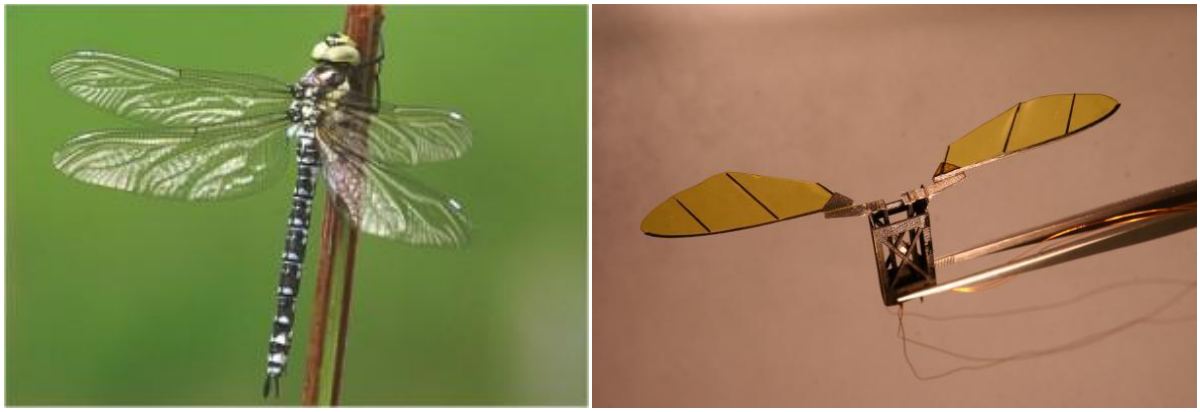

Figure 4-1: Left: Dragonfly, Right: micro scale vehicle (Source_ Michael L. Anderson and Nathanael J. Sladek Air Force Institute of Technology AFIT _1 Mar 2011)

In recent years, a new type of unmanned small aircraft is introduced. This aircraft, which referred to UAV (Unmanned Arial Vehicles), is primarily used for military surveillance. They are small in size and operate at low speed. More recently, these vehicles are built in smaller and smaller sizes to be referred to as MAV (Micro Arial Vehicle). In both cases, these vehicles are characteristically much smaller in weight and size compare to conventional aircrafts, and they operate at much lower Reynolds numbers (10^2 to 10^5), this have made them vulnerable to drastic change in their flying conditions (i.e. gusting wind). This made it essential to introduce the unsteady conditions to enhance their aerodynamics. Similar flying conditions exist already for the case of flapping flight for birds and insects.

Flying birds and insects in addition to fish swimming, with relatively low-aspect-ratio, showed a great enhancement in the aerodynamic efficiency in low Reynolds number. These enhancements were best seen in post stall angle. This is due to better performance at flow separation conditions, partly by making a good use of the vortical flow structure generated by flapping to enhance the aerodynamics of their motion. In the present work, a great emphasis will be given to understand aerodynamic forces due to instantaneous oscillatory motion of the wing, also to understand the structures created due to this motion that is thought to be responsible for alteration of the aerodynamics compared to fixed wing case.

Most of the previous work on the flow around moving wings was focused on flow control applications (Ho & Tai, 1998; Ho, Nassefa, Pornsinsirirakb, Taib & Ho, 2003) through vorticity manipulation (Triantafyllou, Techet, Zhu, Beal, Hover & Yue, 2003; Anderson, Stretlien, Barrett & Triantafyllou, 1998) or thrust generating configurations inspired by biological designs (Erlington, 1984; Birch & Dickinson, 2001; Erlington, Berg, Willmott &Thomas 1996) and the motion of birds (Maxworthy, 1981; Wang 2005) or fish and other

marine mammals. Flapping of wings (Freymuth, 1988), fins, tails or panels (Buckholtz & Smits, 2006) is a characteristic of their motion which generates not only lift and thrust for forward movement, but also provides remarkable maneuvers with rapid accelerations and decelerations. Unsteady hydrodynamics or aerodynamics associated with these flows is normally characterized by moving large-scale vortex structures (Triantafyllou, Triantafyllou & Gopalkrishnan, 1991; Gren & Smits, 2008; Ellenrieder, Parker & Soria, 2003) thus complicating the kinematics of flapping motion and the resulting unsteady vorticity production. In that respect an interesting problem in uncovering the physics of force generation is the role of large-scale vortex dynamics and the corresponding flow topology. Some of the unsteady flow features including the effects of rotation on leading edge and wake vortex dynamics have been described in the aforementioned publications.

4.2 Objectives & Approach

As an extension of this body of work involving oscillatory flows, focus is redirected toward transients associated with thin panels that rapidly emerge in time from a flat wall beneath a flow. In particular, a wind-tunnel experiment has been designed to establish the unsteady aerodynamic characteristics of flaps during their transient impulsive deployment as control surfaces under various flow conditions. To distinguish between the stationary and the rising panel, the latter shall be also referred to as an actuator. Control surfaces/panels may produce aerodynamic forces during their unsteady motion that are different than their corresponding values during static operation. It is envisioned that these wall-mounted devices can be embedded on the surface of an aircraft wing that are deployed on demand through distributed control. At the end of their control cycle they can be retracted so that they are not contributing to the overall drag.

The present flow field involves an impulsively rotating low aspect ratio flat panel in the presence of a cross flow and a solid wall (see figure 5.2). The effects of angular acceleration on the force generation of the rotating panels have been investigated as they interact with the incoming boundary layer and the free stream flow above. Although no previous work on this flow configuration has been identified, several insights on the flow structures can been obtained from observations of flapping motions induced by rotating wings undergoing oscillatory acceleration particularly under hovering conditions. Of interest are the low Reynolds number experiments of Suryadi et al. (2010) and Kim and Gharib (2010) in water which show a continuous pattern of shed vorticity in a vortex around the moving perimeter of the plate containing the leading edge (LEV) and side tip (TV) vortices.

Substantially enhanced drag forces have been observed experimentally and theoretically in flat plates normal to the flow undergoing longitudinal acceleration during impulsive translational motion (Sarpkaya, & Kline, 1982; Ringuette et al. 2007; Koumoutsakos & Shiels, 1996; Taira et al. 2007). Theoretical considerations show that the vorticity which is related to circulation is responsible for the generation of lift force exerted on solid bodies immersed in a fluid.

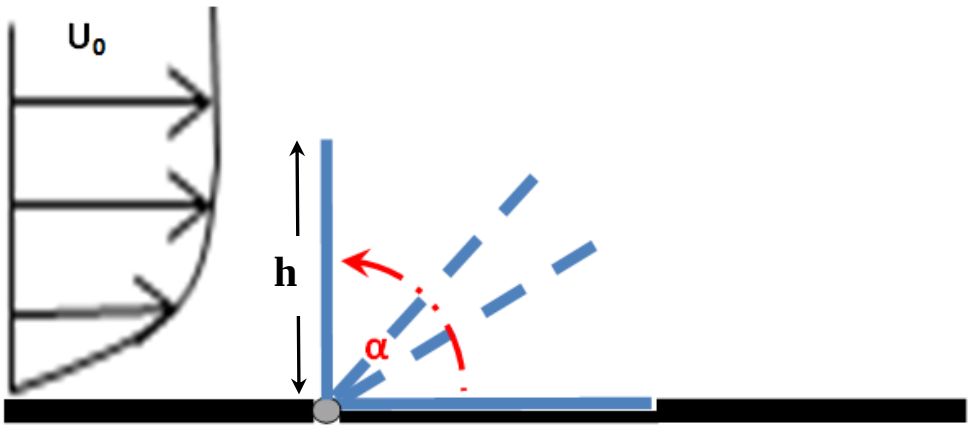

a)

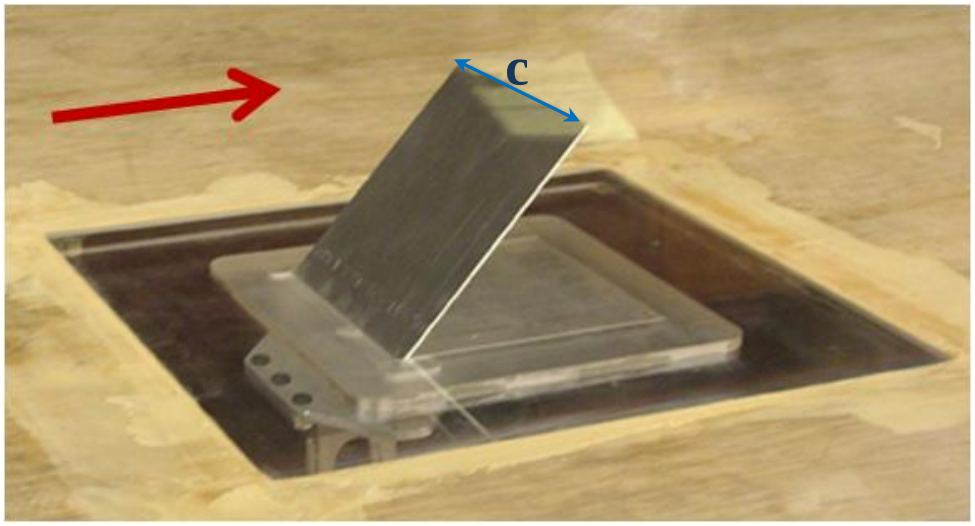

b)

Figure 4-2: a) Side view of the actuator (with height h=100mm, and span c=100mm), where it is deployed against the incoming BL flow, b) actual photograph for the actuator placed on the wind tunnel floor (red arrow shows the flow direction)

Wu et al. 2005 and 2006 have derived vorticity moments-based relations of forces of finite bodies exerted by viscous incompressible fluid flows using conditions that are shown to be satisfied under general circumstances. In particular, it has been shown that the unsteady aerodynamic forces (drag and lift) exerted by a fluid on solid bodies immersed in and moving relative to the fluid is

$$F = \rho \frac{d}{dt}\left[\int_{\partial B} r U_{bn} dS + \int_{\Sigma} r U_{\Sigma n} dS\right] - \rho \frac{d}{dt}\int_{V_f} r \times \omega dV - \rho \int_{V_f} \omega \times U dV - \rho \int_{\Sigma} r \times (n \times \omega \times U) dS + F_{\Sigma} \qquad \textit{(Eq. 5.1a)}$$

With

$$F_\Sigma = -\int_\Sigma r \times [n \times \mu(\nabla \times \omega)]dS + \int_\Sigma \mu\omega \times n\, dS \qquad \textit{(Eq. 5.1b)}$$

where ρ is the fluid density, r the position vector measured from any given origin, V_f is the fluid domain bounded internally by the body surface ∂B and externally by an arbitrary control surface Σ. Both surfaces ∂B and Σ are allowed to move with velocities U_{bn} and $U_{\Sigma n}$ in the normal to the surface direction.

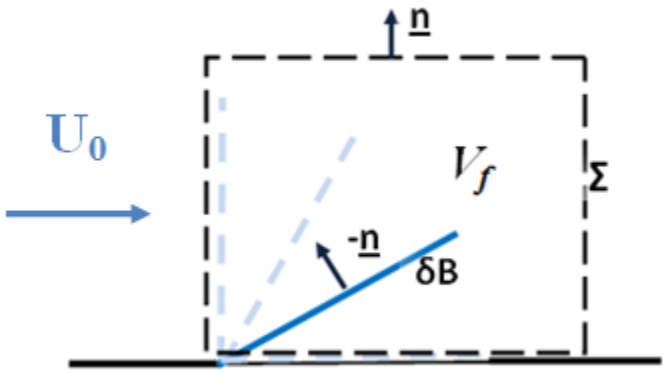

Figure 4-3: Schematic of control volume Ω. n is in the outward direction of Ω

It is very instructive to consider the underlying physics of the first relation. The first two terms in the brackets represent the inertia effects of the incompressible fluid in the volume $V_f = \frac{d}{dt}\int_{V_f} UdV$. The first of the subsequent two volumetric integrals represents the time-rate of change of the first moment of the vorticity field while the second is the Lamb force. The last surface integral represents the moment of the Lamb vector flux through the outer surface Σ. Finally F_Σ represent all viscous effects on Σ.

Wu's theory can be extended to include the flow above an infinite long wall like the present case by considering rectangular flow domains and control volumes. In either case the above

relation holds and indicates that the force on the body can be generated by the inertia of the fluid $\rho\frac{\mathrm{d}}{\mathrm{dt}}\int_{\mathrm{V_f}}\mathrm{UdV}=\rho\frac{\mathrm{d}}{\mathrm{dt}}\left[\int_{\partial\mathrm{B}}\mathrm{rU_{bn}dS}+\int_{\Sigma}\ \mathrm{rU_{\Sigma n}dS}\right]$ *(Eq. 5.3)*

or by the temporal variation of the moment of existing vorticity

$$\frac{1}{2}\frac{\mathrm{d}}{\mathrm{dt}}\int_{\mathrm{R_b}+\mathrm{R_f}}\mathrm{r}\times\omega\mathrm{dR} \qquad \textit{(Eq. 5.4)}$$

and the Lamb's vector accumulated over the entire flow domain. Although Wu's theory does not account for the generation of vorticity it is very useful in pointing out that the temporal variation of the whole vorticity field and the Lamb vector can generate a force on the immersed bodies.

The rotating motion of the flap inside the viscous fluid will generate vorticity at its surface by the action of pressure gradients which will be subsequently shed into the flow field. The Navier-Stokes equations written in rotational form for a coordinated system associated with the stationary wall in tensor notation are

$$\rho\frac{\partial U_i}{\partial t}=-\frac{\partial p}{\partial x_i}-2\rho U_k R_{ik}+2\mu\frac{\partial R_{ij}}{\partial x_j} \qquad \textit{(Eq. 5.6)}$$

where $\mathrm{R_{ij}}$ is the rotation-rate tensor $R_{ij}=\frac{1}{2}\left(\frac{\partial U_i}{\partial x_j}-\frac{\partial U_j}{\partial x_i}\right)=-\frac{1}{2}\varepsilon_{ijk}\Omega_k$, Ω_{k} is the vorticity and p is the total pressure. The term $2\rho U_k R_{ik}$ represents the Lamb vector. These equations when applied to the moving wall of the flap became

$$\left[\frac{\partial p}{\partial x_1}\right]_w=\left[-2\rho u_{bn2}R_{12}+2\mu\frac{\partial R_{12}}{\partial x_2}\right]_w=[\rho u_{bn2}\Omega_3]_w-\left[\mu\frac{\partial \Omega_3}{\partial x_2}\right]_w \qquad \textit{(Eq. 5.7)}$$

$$\left[\frac{\partial p}{\partial x_3}\right]_w = \left[-2\rho u_{bn2} R_{32} + 2\mu \frac{\partial R_{32}}{\partial x_2}\right]_w = [\rho u_{bn2} \Omega_1]_w - \left[\mu \frac{\partial \omega \Omega_1}{\partial x_2}\right]_w \qquad \textit{(Eq. 5.8)}$$

where u_{bn2} is the moving body velocity which is normal to its surface. The last term in each of the above equations represents the flux of the spanwise and longitudinal vorticity which enters the flow field. It is the unsteady character of this vorticity which can change the moment of the vorticity field and therefore an aerodynamic force can be generated.

Key flow parameters in the present flow are:

Reynolds number of the flow: $Re_h = U_o h/\nu$

Stokes number: $St = \omega h^2/\nu$

where ω is the frequency of deployment motion. The Stokes number expresses the ratio of the unsteady boundary layer thickness on the actuator, $\delta_a = (\nu/\omega)^{1/2}$, to the size of the actuator, h. If St is large the actuator is not strongly influenced by viscous effects, while if St is small the flow on the actuator is strongly viscous.

The Reynolds and Stokes numbers can be combined to form a Strouhal number:

$$Str = St/Re_h = \omega h/U_o = U_r/U_o$$

where U_r is the velocity at the apex of the actuator. The Str number is identical to what is known in unsteady aerodynamics as reduced frequency k, or it is the inverse of the Rossby number defined as $Ro = U_o/\omega h$ which is used in rotating flows.

4.3 Outline of Part II

- Chapter 5: Experimental work showing direct measurements of the time-dependent aerodynamic forces acting on the actuator during deployment inside turbulent boundary

layer. These experiments are performed in the wind tunnel facility at Reynolds number 23,000 & 68,200 with different Strouhal numbers.

- Chapter 6: Detailed Flow visualization studies and TR-PIV measurements are performed as an attempt to understand and explain the three-dimensional flow structure around the actuator at different Str. In addition to flow analysis to understand the effect of vorticity and its time rate of change on aerodynamics.
- Chapter 7: Split-View TR-Stereo PIV with CW laser setup is introduced to measure three-component-velocity vector. The setup is applied to measure the velocity for the present actuator deployment experiment.

Chapter 5 : Aerodynamic Forces (direct measurements)

5.1 Experimental Setup

A square-shaped actuator, with dimensions of 100mm x100mm (w x h), is embedded in the floor of the wind tunnel. The actuator is remotely controlled to rotate against the incoming flow (as shown in figure 5-1) between 0 to 90 degrees, and it is driven by a servo-motor (made by Ko propo) that can sustain relatively high torque (up to 17.6 Kg-cm) and rotates with high speed of (60 degrees/0.06 sec).

As the present work requires a time dependent measurements for the aerodynamic forces, a force balance (Pierides, 2010) was used to directly resolve the horizontal and the vertical components of the forces, which corresponds to the direction of drag and lift forces respectively. This decoupling of the measurements of the drag and the lift forces presented a crucial advantage, since each force signal can be acquired and amplified separately. This also provided the ability to improve the dynamic range of the data acquisition system, therefore the measurements precision.

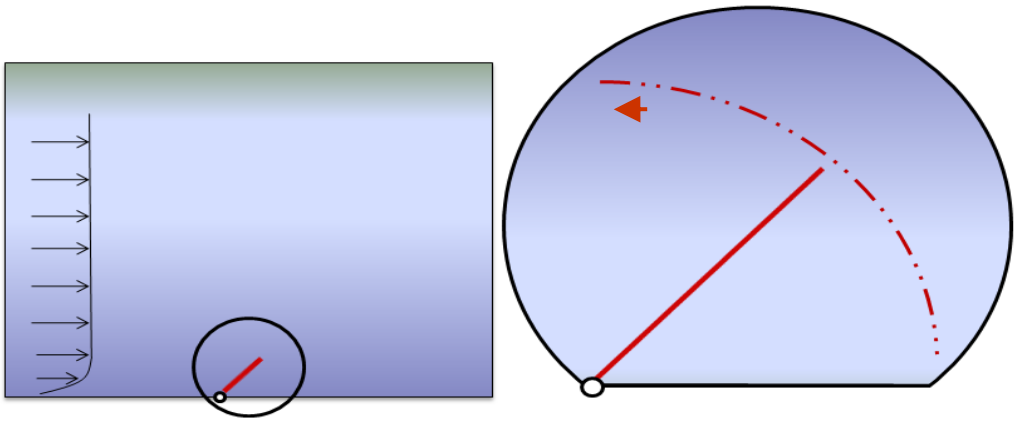

Figure 5-1: Side view shows the direction of the actuator deployment (rotation against the incoming flow)

The balance was designed to be mounted on a separate frame (figure 5-2.a), where it can be always detached from the wind tunnel to avoid signal contamination due to wind tunnel vibrations. The forces are measured by the means of three tension compression load cells made by Honeywell (Model 34-1000gr).

The first load-cell is used for direct lift measurements, however, due to the fact that only the moment results from the drag force can be measured here, two load-cells are used to measure this moment at two different locations, therefore, the time-dependant location of the center of pressure can be determined.

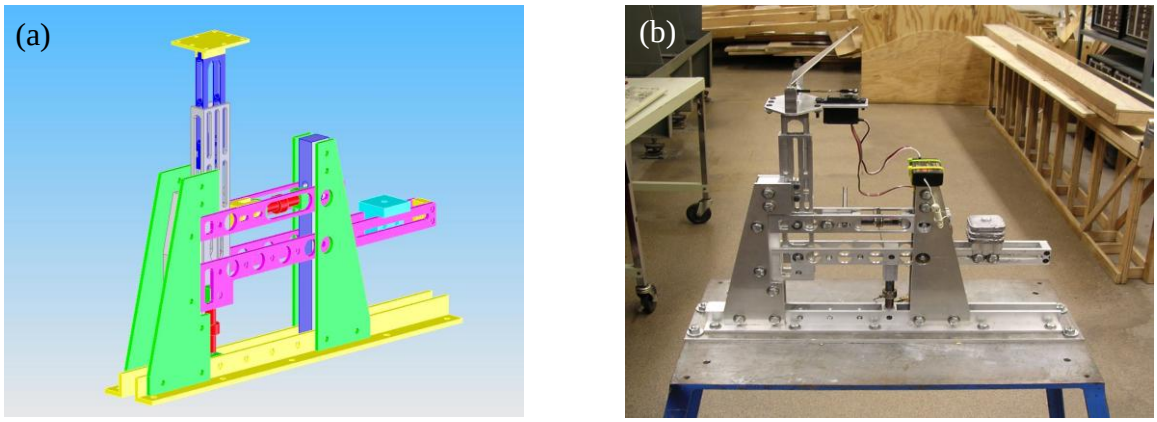

Figure 5-2: : a) 3D Model of the balance used to measure time-dependent aerodynamics forces, b) An actual photograph for the balance mounted on separate frame (Pierides, 2010)

Actuator's deployment control:

As mentioned previously the actuator is been driven by a servo-motor. This servo-motor connected to the actuator by a simple four arm mechanism that can amplify the rotation of the motor to the actual deployment angle of the actuator.

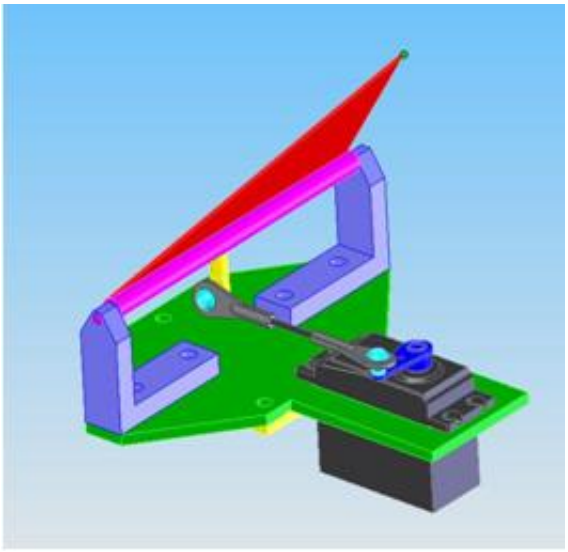

Figure 5-3: Actuator model shown connected to the servo motor with four-arm mechanism (Pierides 2010)

The servo motor is controlled by Pololu USB 16-channel Servo controller connected to PC computer. Using matlab code, the motor starting position, the final position and the speed can be

controlled. The motor can rotate within an angle of 90 degrees, which is amplified by the use of the four arm mechanism; the range has a precision of 1024 positions.

The speed of the servo motor is set on the computer program by specifying the time to reach the final position. The servo motor is also equipped with internal position encoder, where the signal shows in real time the actual position of the servo motor. This signal has a critical role as it is used to evaluate the actuator motion in terms of the acceleration and deceleration duration, in addition to identifying the inertial forces due to the actuator motion; and computing the actual deployment speed.

5.2 Inertia Forces

Due to the fact that that the measured forces actually represent the combined effect of aerodynamic forces in addition to the inertia forces, which a result of the motion of actuator (figure 5-4) according to equations (5-1) & (5-2), the actuator kinematics needed to be evaluated as well to compute the aerodynamics forces acting on the actuator.

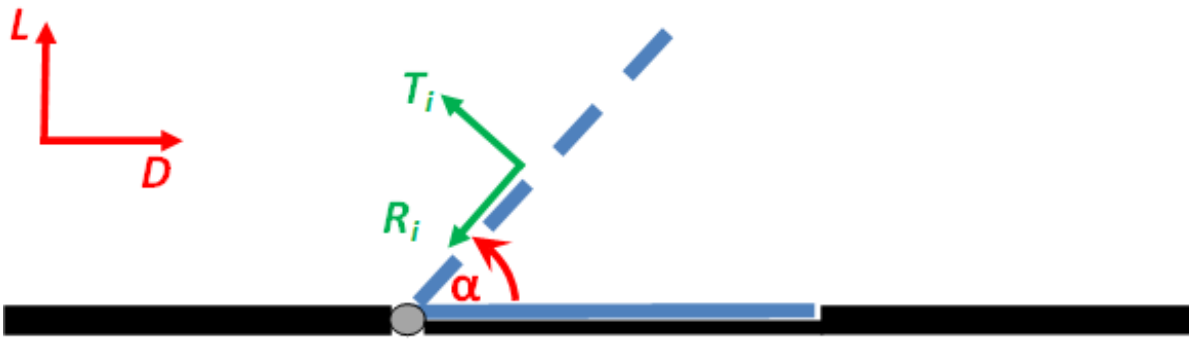

Figure 5-4: Measured forces acting on the actuator during deployment are aerodynamic forces lift (L) and drag (D), and inertia forces (T_i) in tangential direction and (R_i) in radial

Lift: $L = L_{measured} - (T_i \cos\alpha - R_i \sin\alpha)$ (Eq. 5-1)

Drag: $D = D_{measured} + (T_i \sin\alpha + R_i \cos\alpha)$ (Eq. 5-2)

Where $T_i = mr\omega^2$ (Tangential component of inertial force) (Eq. 5-3)

$R_i = mr\frac{d\omega}{dt}$ (Radial component of inertial force) (Eq. 5-4)

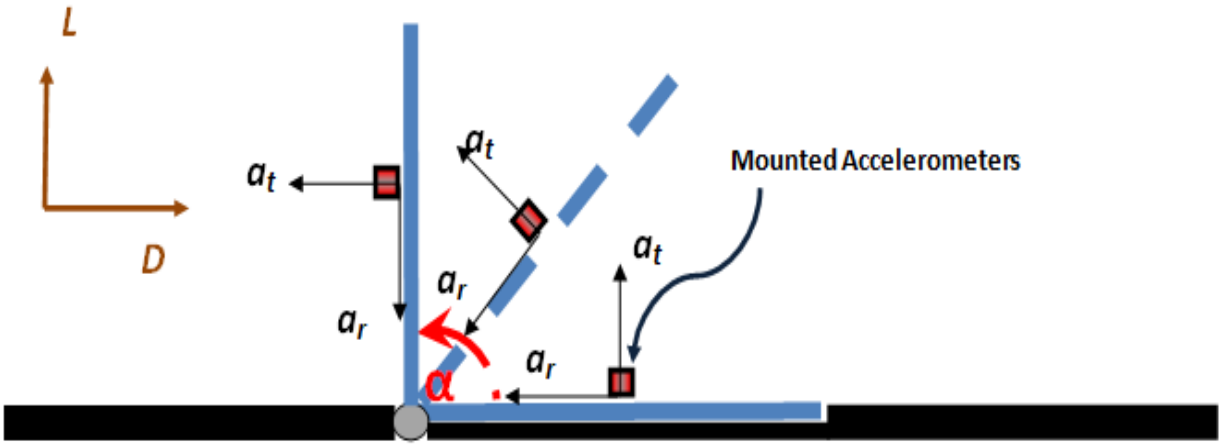

Figure 5-5: Tangential and Radial accelerometers are mounted on the center of the actuator to measure accelerations to compute the time-dependent inertia forces

Two accelerometers, type EGAX-25-C200001 manufactured by Entran, are mounted on the center actuator body to allow for measuring the actual kinetics of the actuator motion, therefore the tangential and the radial components of inertia forces can be computed from equations (5-3) & (5-4) respectively. Since the accelerometers are unidirectional in measuring the acceleration, two facts was needed to be considered here; first, both accelerometers were mounted in a way that each one can measure one acceleration component, the tangential acceleration (a_t) and the radial acceleration (a_r) (figure 5-5), second, while measuring the actuator kinetics during the deployment from 0 to 90 degrees, the gravitational acceleration (g) component is being recorded in the measurements also. This component, which changes from -1g to zero in the tangential accelerometer and from 0 to 1g in the radial accelerometer must eliminated from the raw signal

to obtain only the acceleration components that correspond the inertia forces. Meanwhile the encoder signal is used to resolve α (the actuator angle) where ω (angular velocity) is computed.

$$\omega = \frac{\partial \alpha}{\partial t}$$

Tangential acceleration: $a_t = r * \frac{\partial \omega}{\partial t}$, Radial acceleration: $a_r = \omega^2 * r$

And the measured acceleration normal to the actuator is: $a_{t,m} = a_t + g \cos \alpha$,

And radial direction of the motion is: $a_{r,m} = a_r + g \sin \alpha$

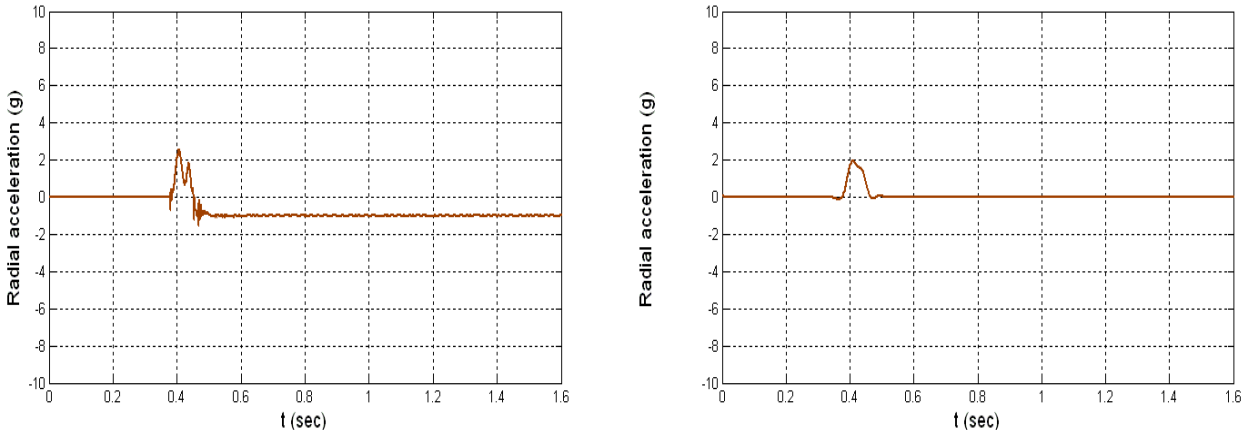

Figure 5-6: On left the raw signal of accelerometer (mounted in the radial direction), including the gravity component, on the right the gravity component is removed from the original signal and the signal is being filtered (Low pass, Type 1, Chebyshev filter)

The left side of figure 5-6 show typical raw signal output for the accelerometer, where the gravity component can be seen as the acceleration value changes at stationary position before and after the deployment; and on the right, the outcome signal after removing the gravity component and filtering the original signal.

Figure 5-7 and 5-8 show the tangential and the radial acceleration (in gravitational units), respectively. In these figures, the acceleration signals were acquired for different deployment angular velocities which range from 1 to 20 rad/sec, shown in terms of Str. (figure 5-7 and 5-8). These plots correspond to freestream velocity case of 3.7m/s and Re=23,000.

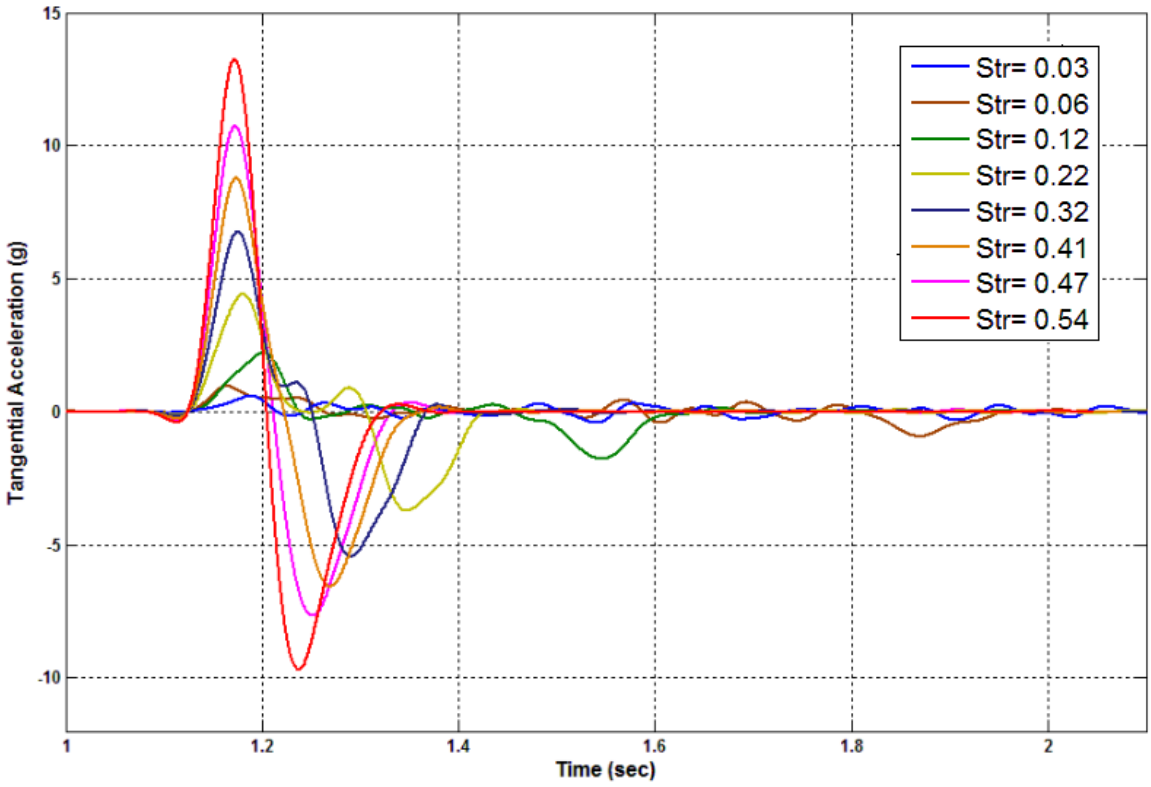

Figure 5-7: Tangential Acceleration against time for different Str at Re=23,000

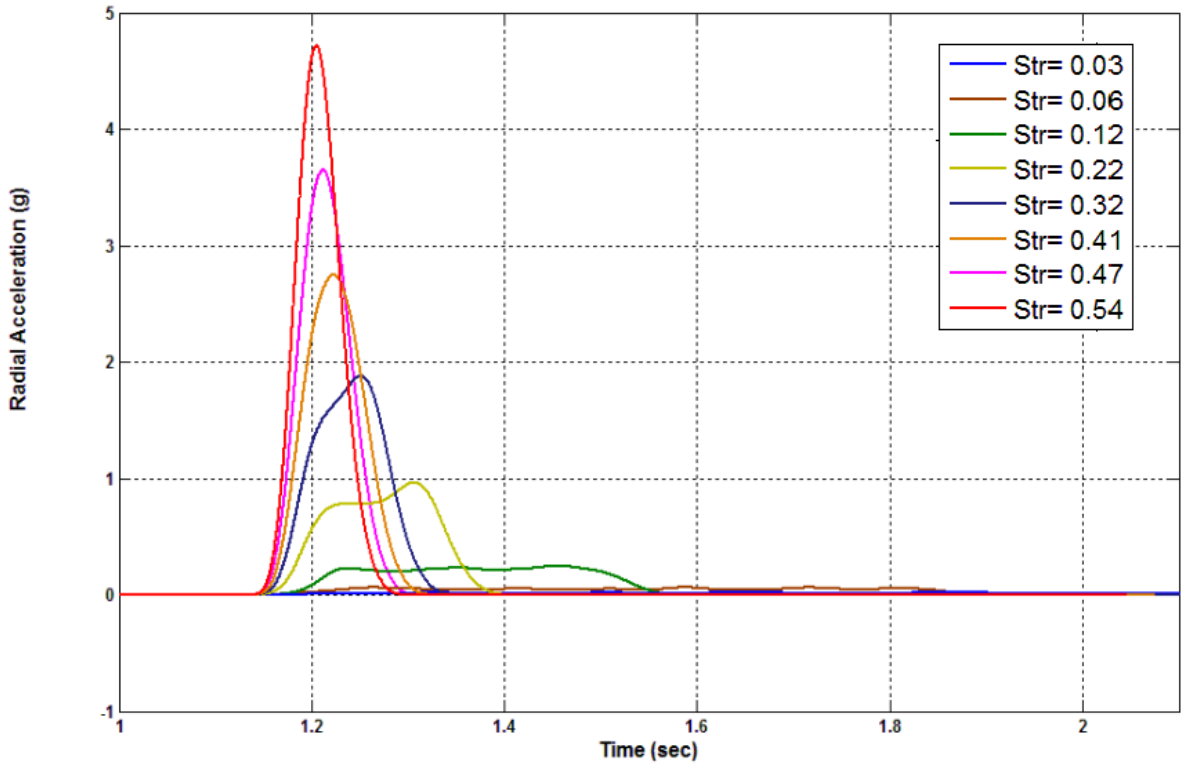

Figure 5-8: Radial Acceleration against time for different Str at Re=23,000

In figure 5-9, the angular position of the actuator is plotted against time at different angular velocity values. It's been noticed in this low Strouhal number cases, the angular velocity of the actuator is characterized by small initial period of accelerating motion then followed by constant angular velocity motion with zero acceleration and a final decelerating period before it stops. In the high Strouhal number cases, the constant velocity zone diminishes and the initial and final periods associated with acceleration dominate.

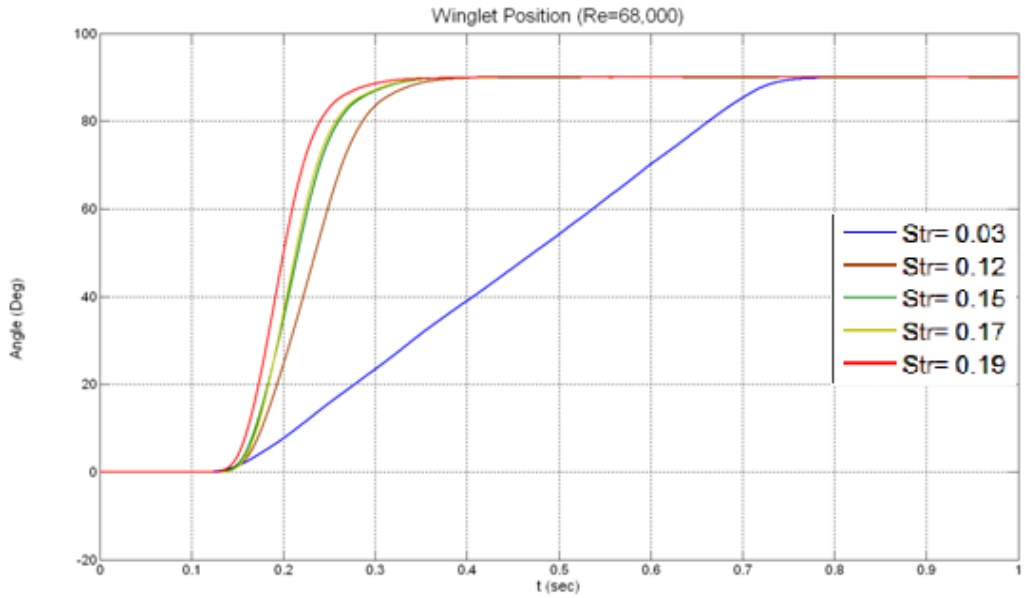

Figure 5-9: Encoder signal indicate the actuator position, at a range of angular velocity

Once the inertia forces are computed from the acceleration, these inertia forces are then subtracted the from the measured force data to obtain the lift and drag forces. Figures 5-10a and 5-10b show the inertia forces, measured forces and the resultant drag and lift forces.

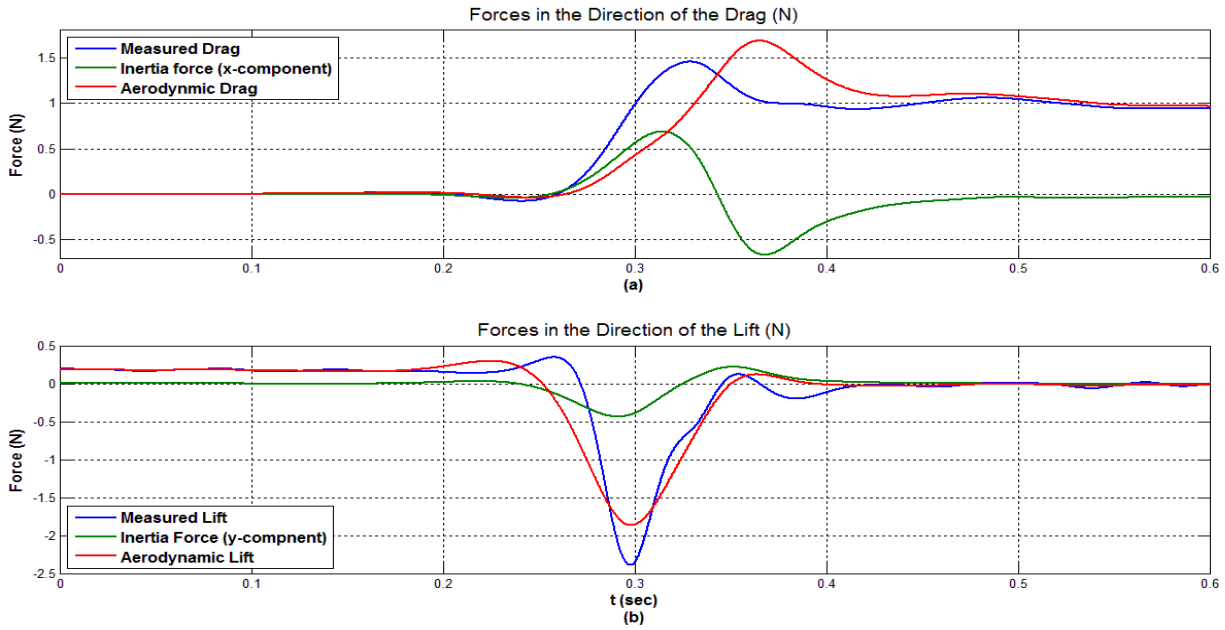

Figure 5-10: Inertia forces are subtracted from the measured force to obtain the aerodynamic forces (a. drag, b. lift). (Str=0.19, Re=68,000)

5.3 Data acquisition and processing

In the present experiments, all the output signals of the three load cells, the two accelerometers and the encoder signal were simultaneously acquired by single data acquisition system Model IOTECH ADC with a sampling rate of 10k per second during the deployment of the actuator. An analog low-pass filtering of the incoming signals was carried out before digitization with a cut-off frequency set at 500Hz.

All signals are processed and filtered using matlab. The filter used for all of the experiments was a second order, Low Pass, Type I, Chebyshev filter with 0.1dB of ripple in the pass band, a cutoff frequency of 10 Hz with of minimal phase shift. To illustrate the effects of filtering, the raw output data of the lift load cell, presented in Figure 5-11, are compared with the corresponding filtered ones.

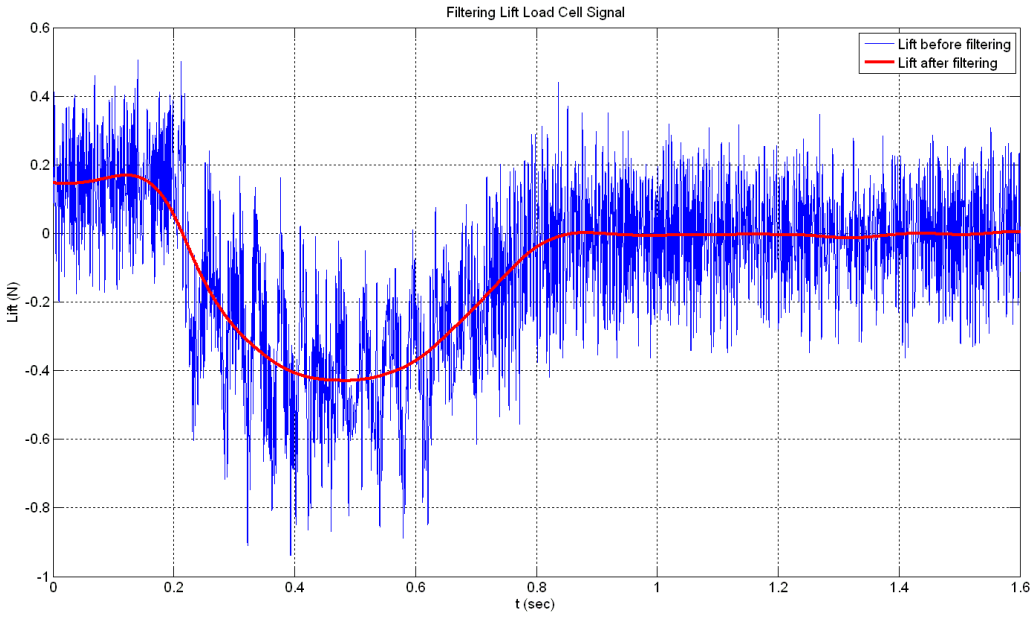

Figure 5-11: Sample of output raw signal in blue and filtered signal in red (the signal taken from lift load cell)

Several experiments were carried out in the wind tunnel facility, where the effect of Strouhal is investigated, in addition to the effect of Reynolds number and the boundary layer thickness, table 1 show a list of all experiments:

Experiment Name	U_0 (m/s)	δ/h	ω (rad/s)	Re	St	Str
D11-003	11	2.0	3	68,200	2,044	0.03
D11-012	11	2.0	13	68,200	8,176	0.12
D11-015	11	2.0	17	68,200	10,220	0.15
D11-017	11	2.0	19	68,200	11,577	0.17
D11-019	11	2.0	21	68,200	12,939	0.19
D3.7-003	3.7	1.4	1	23,000	2,044	0.03
D3.7-006	3.7	1.4	2	23,000	4,086	0.06
D3.7-012	3.7	1.4	4	23,000	8,176	0.12
D3.7-022	3.7	1.4	8	23,000	14,982	0.22
D3.7-032	3.7	1.4	12	23,000	21,792	0.32
D3.7-041	3.7	1.4	15	23,000	27,921	0.41
D3.7-047	3.7	1.4	17	23,000	32,007	0.47
D3.7-054	3.7	1.4	20	23,000	36,774	0.54

Table 5-1: Parameters in experiments of impulsive deployment of a square panel actuator within boundary layer of thickness 50mm and 74mm

5.4 Experimental results and discussion

5.4.1 The effects of Strouhal number

Several experiments were carried out to establish the effects of the actuator deployment speed while keeping the incoming free steam flow velocity U_o constant. In the first set in the

experiments (U_0 = 11m/s and δ= 5cm), Strouhal numbers from 0.03 to 0.19 were achieved in these experiments. The effects of the deployment speed is demonstrated in figures 5-12 and 5-13 where the drag coefficients ($C_D = \frac{D}{\frac{1}{2}\rho U_0 A}$) and lift coefficient ($C_L = \frac{L}{\frac{1}{2}\rho U_0 A}$), where A is the actuator surface area, are plotted as a function of time for various experiments at constant free stream velocity U_0 and different angular velocities of the actuator deployment ω. The deployment is always at constant angular speed ω except at the beginning and at the end of the transient time and therefore the time is proportional to the angular position of the actuator α since α=ωt.

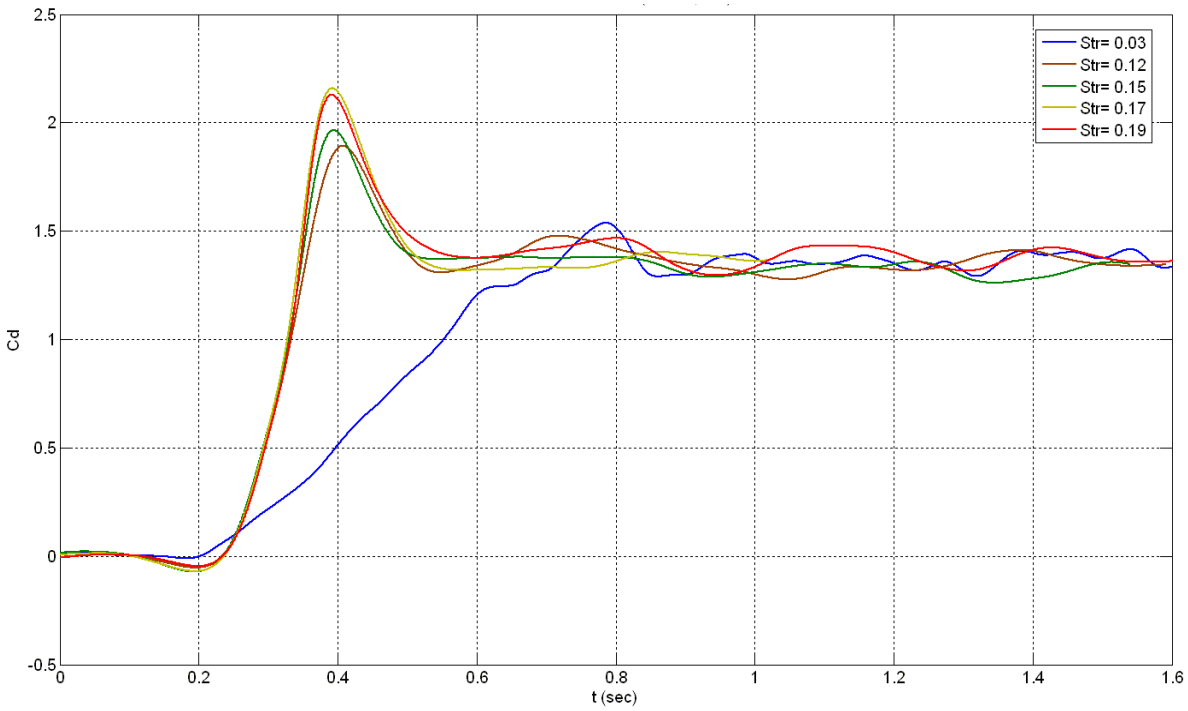

Figure 5-12: Coefficient of drag (C_D) during actuator deployment (0 to 90 deg), the increase of Str causes increase in C_D during transient deployment (Re=68,200)

The lowest Str case can be considered as a quasi-steady state experiment, since the deployment velocity is slow compared to the freestream velocity. The drag coefficient simply increases to the steady state value with minimal overshoot at the end of the deployment. As the Str and

deployment speed increase, apparent by the steeper and steeper angles at which drag is increasing with time, the maximum dynamic drag exerted on the winglet is also increased. As the drag force coefficient increases with increasing deployment angle α it reaches its maximum value at about 80 degrees. The ratio of the maximum dynamic drag force to that of the static force appears to increase with increasing Str number, which expresses the ratio U_r/U_0. Thus the greater the relative velocity of the actuator tip, the greater is the ratio of the forces and therefore the dynamic deployment effects. The data also demonstrate that the peak dynamic C_D is always greater than the static aerodynamic force coefficient, suggesting a surplus of control force during dynamic operation of the flaps.

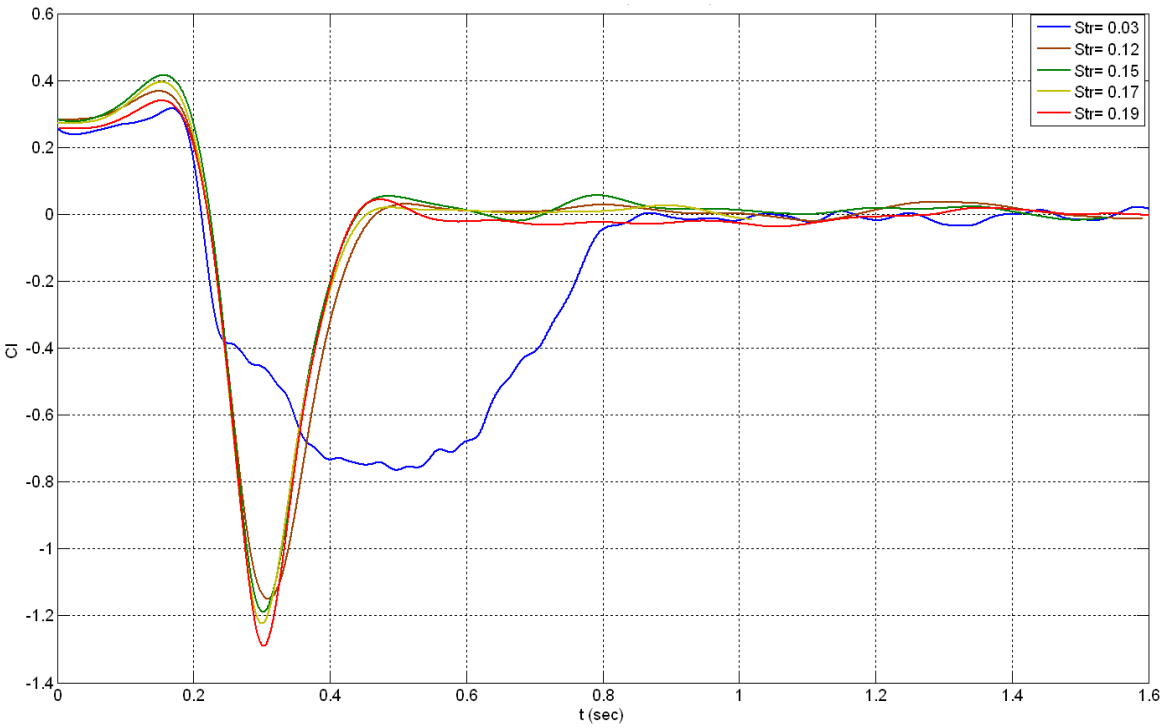

Figure 5-13: Coefficient of drag (C_L) during actuator deployment (0 to 90 deg), the increase of Str causes increase in C_L during transient deployment (Re=68,200)

Of equal importance to the drag, is the effect that the increasing deployment speed has on the coefficient of lift. Figure 5-13 shows the coefficient of lift with respect to time for the same

experiments, as the deployment speed for the winglet is increased from 3 rad/sec to 21 rad/sec. Figure 5-13 shows that the lift development with respect to the deployment angle is qualitatively different than that of the drag. It has a negative peak which increases in absolute value with increasing Str. At the end of the deployment, it reaches zero values in all cases and the dc offset observed before deployment is due to the pressure difference which exists between the working section wall and the ambient. It is also evident that the dynamic lift profile of all the lift curves is similar. If we consider the Str = 0.03 as a quasi-steady state lift profile, we can see that all other dynamic profiles are qualitatively the same.

In the second set of the experiments, whereas the increase of the Strouhal number was limited by the servo-motor capabilities, a lower Reynolds number (Re= 23,000) was selected to carry out the experiments, by lowering the freestream velocity U_0 =3.7, therefore higher Str for the actuator deployment can be obtained. The coefficients of drag and lift are shown in figure 4-14 & 4-15, respectively. The effect of Str number on the both coefficients continued to show the same behavior with peak value increases with the increase of Str number, with the increase of the coefficient of drag that can be more than 6 in highest deployment Str. Similarly, the coefficient of lift increased in the negative direction with the increase of Strouhal number to reach -3 in the case of Str=0.54.

Note that in both figure 5-14 & 5-15, the horizontal axis is been modified by multiplying the time scale by the Strouhal number and amplified by 10, this mainly was to fit the data in the same range, since the lowest Str (0.03) was occurring a much slower rate compared to the highest Str (0.54).

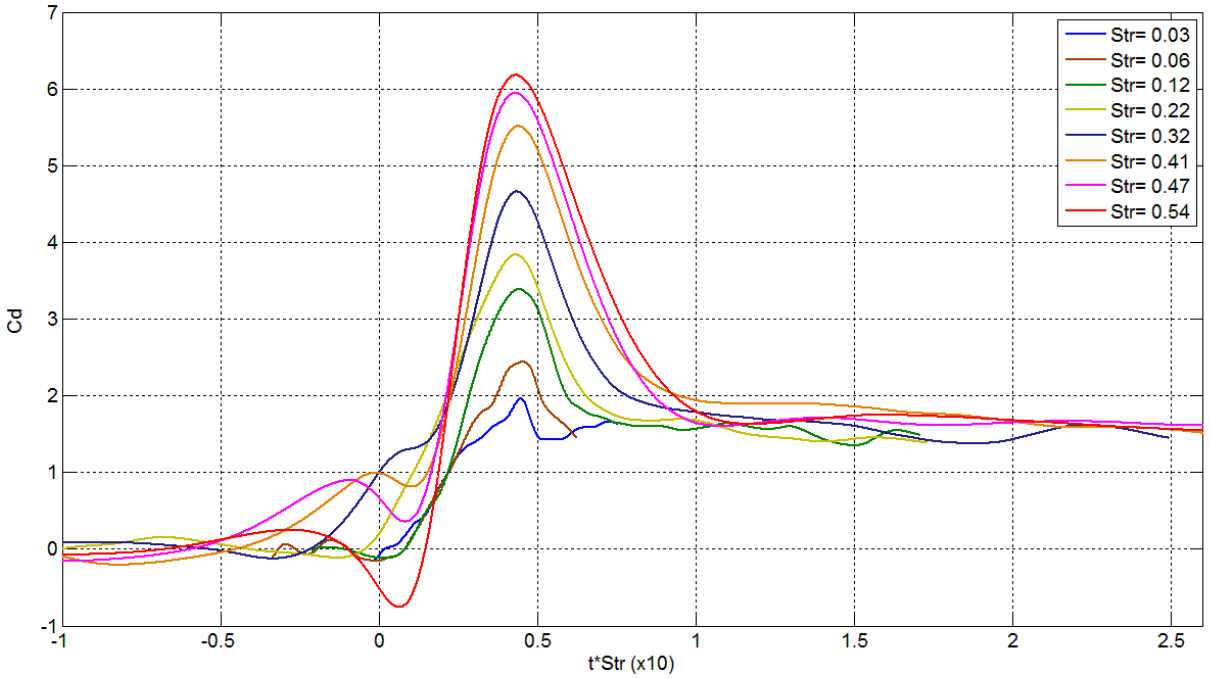

Figure 5-14: Coefficient of drag (CD) during actuator deployment (0 to 90 deg), the increase of Str causes increase in CD during transient deployment (Re=23,000)

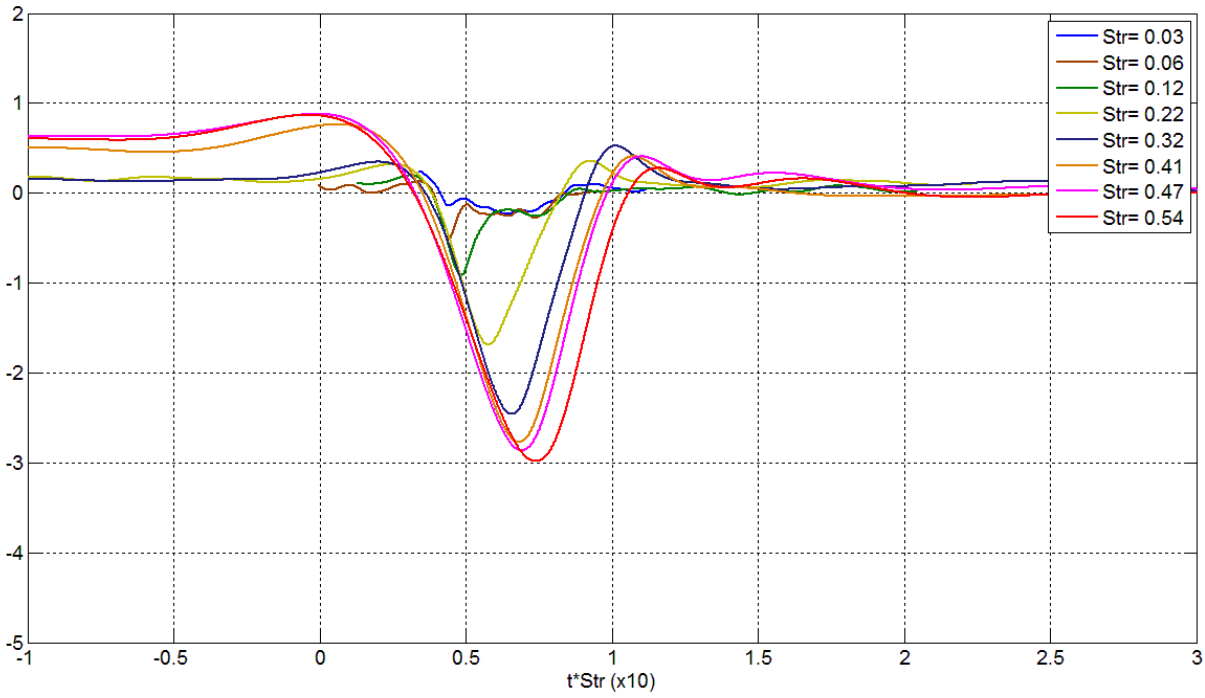

Figure 5-15: Coefficient of drag (C_L) during actuator deployment (0 to 90 deg), the increase of Str causes increase in C_L during transient deployment (Re=23,000)

5.4.2 The effects of the Reynolds number

A parametric study was carried out from the previous experiments to investigate the effects of the change of Reynolds number, and boundary layer thickness in addition to Strouhal number on the peak value of the coefficient of drag. Figure 5-16 shows an increase in the slope of the peak value with the decrease of Reynolds number; however, in both cases the increase of the peak value of the drag coefficient seems to increase linearly with the increase of Strouhal number.

It's important to mention here, that a significant decrease of the actual magnitude of the drag forces has been observed due to the decrease of freestream velocity and the corresponding increase of boundary layer thickness; however, a small increase in the coefficient was seen with the decrease of Reynolds number.

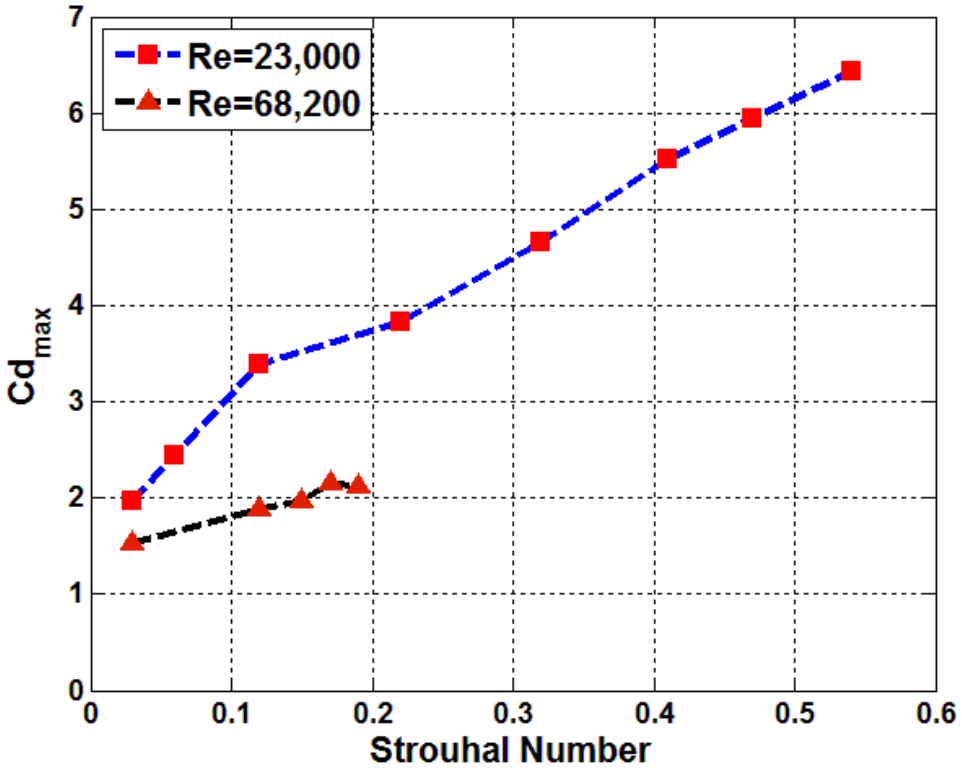

Figure 5-16: Peak value for the coefficient of drag at different Str, for two different Re (68,200 & 23,000)

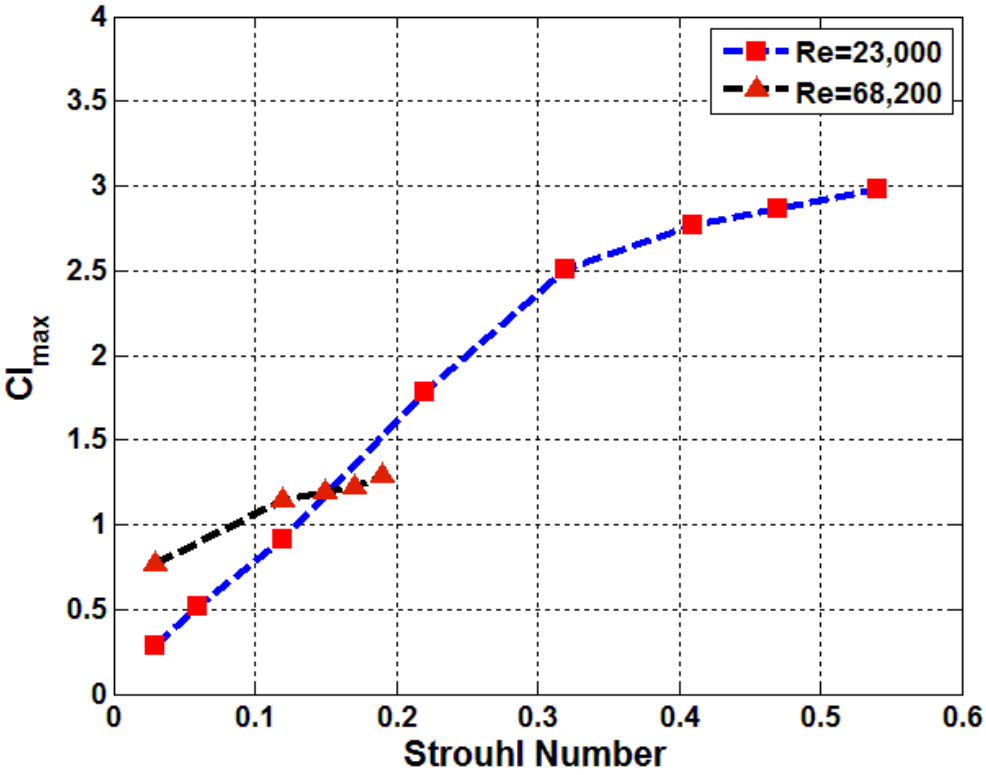

Figure 5-17: Peak value for the coefficient of lift at different Str, for two different Re (68,200 & 23,000)

Figure 5-17 shows similar behavior for the peak value of the lift coefficient, in both Reynolds number the max. The value of the lift coefficient increases with the increase of the Strouhal number, and this increase appears to be linear at first; however at higher Strouhal number the peak value appear to change slope toward weaker relation with the increase of the Strouhal number.

5.4.3 The effects of the boundary layer thickness

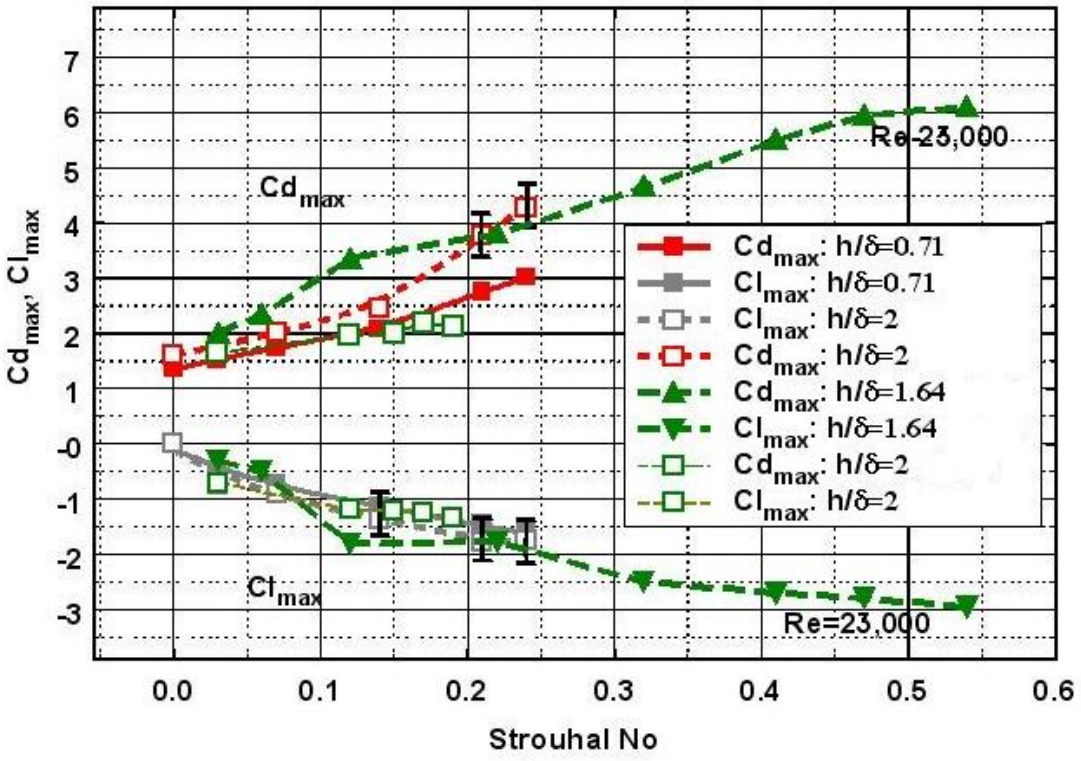

Figure 5-18: combined maximum coefficient values for both C_D and C_L, dashed line from present experiments (h/δ =2 for cases at Re=68,200, and h/δ =1.64 for cases at Re=23,000), continuous lines from Pierides 2010, (h/δ =0.71 for cases at Re=72,600, h/δ =2 for cases at Re=68,200)

In figure 5-18, all the values for the maximum coefficients cases are combined for both the drag and the lift coefficients for both cases of the present work of freestream velocity 3.7m/s and 11m/s which correspond to h/δ= 1.64 and 2 respectively (shown in dashed lines). Also the data from Pierides (2010), which were acquired on the same facility, are shown for multiple cases. In Pierides (2010), all experiments were carried out at almost constant freestream velocity of 11m/s at different locations of the wind tunnel, where the effect of the boundary layer thickness (δ) can be monitored. The first case corresponds to h/δ=2 (similar to the present case of Re=68,200), and the second case corresponds to smaller h/δ=0.71 (taken at further location of the testing area in the WT facility). At this location the value of the boundary layer thickness (δ) equals 140 mm. The drag data are systematically higher in the case of h/δ=2 than in the case of h/δ=0.71 and at

the peak of the dynamic effects they are up to 40 % greater. The peak lift coefficient is also slightly greater in the case of the thinner boundary layer with h/δ=2.0. The increase in Str has a significant effect on the maximum value of the drag coefficient which increases substantially. The data of the h/δ=2 case show clearly higher values than the corresponding h/δ=0.71 data for the same Str. In addition, the rate of increase of C_{dmax} with Str is higher in the thinner boundary layer with h/δ=2. For the case of h/δ=1.64 which was taken at lower Re of 23,000, an increase of the maximum drag coefficient were observed at higher Str. And one probable explanation to this is the fact the effective velocity profile in the boundary layer is smaller than the freestream profile, therefore the bigger the ratio of the actuator height (h) to the boundary layer thickness the bigger the resultant maximum coefficients.

It's important to mention here that a large difference of the maximum coefficient values for the drag measurements between the present case and similar case in Pierides (2010) exists (shown in figure 5-18 with open square symbols). This difference wasn't explained by the uncertainty of the measurements. It's not very clear the reason for this difference, however, it's suspected that the use of different servo-motor with different torque and speed characteristics maybe responsible. Servo-motors with different torque and speed demonstrated a difference in their dynamics, particularly in the derivative of acceleration with respect to time. This determines the duration for the actuator achieves the preset speed, which is seen in the accelerations data previously. This brings the fact that studying the actuator dynamics in terms of the time rate of change of the acceleration in addition to Strouhal number would be important to fully quantify the actuator response.

Chapter 6 : Flow Visualization & TR-PIV measurements

6.1 Introduction

In this chapter, concentrated flow visualization and TR-PIV measurements is presented to further investigate the flow around the actuator during the transient deployment. First, flow visualization experiments are carried out to understand how the flow develops around the moving actuator, and to make a possible association between the sudden increase in the aerodynamic forces and the flow dynamics and topology. In the second part of this chapter, TR-PIV measurements are carried out to resolve the flow velocity around the actuator, investigate the vorticity fields, and understand how these fields are affected by the deployment Strouhal number. In addition to this, an attempt is made using equation 4-1 to compute the aerodynamic forces using flow velocity data obtained by the TR-PIV mainly to estimate the contribution of each of the physical terms shown in equation 4-1, such as volume integral of the lamb vector and unsteady vorticity, in the drag and lift forces.

6.2 Flow Visualization

In these experiments, a sheet of laser light is used to illuminate the flow field at different locations in two directions, both in streamwise direction, figure 6-1.a and 6-1.b shows the locations of the light sheet where the images of the flow are taken in the wall normal direction and the spanwise direction respectively. Camera 2 is used for imaging at a rate of 3000 fpr, where the flow is seeded at the entrance of the wind tunnel using fog machine. The water based

vapor machine (type martin-1800) was proven to be more suitable for the flow visualization experiments than the atomized oil because of the high particles density the machine disperse, moreover, the light scatter by the vapor particles were more than those the case with atomized olive oil.

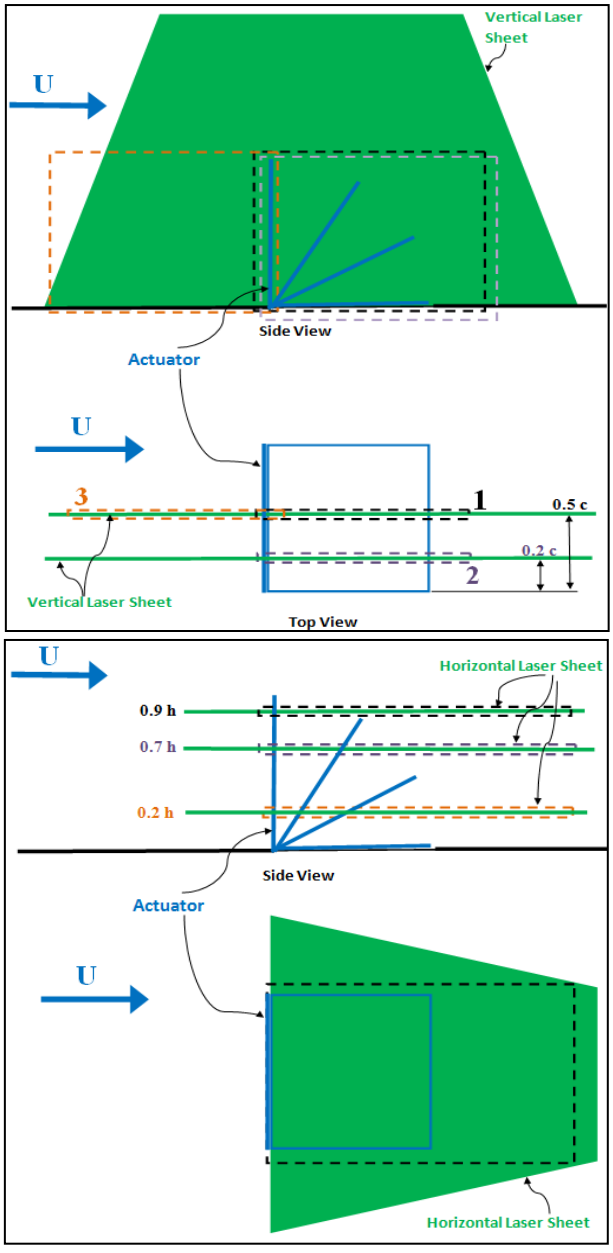

Figure 6-1: flow visualization experiments FOV's: a) FOV is in the streamwise-normal to the wall, b) FOV in the streamwise-spanwise direction.

6.2.1 Interaction between the actuator and boundary layer structures

The present flow can be considered as the result of a continuous transient interaction between a deploying actuator with a well described and controlled motion and the incoming flow which consists of freestream irrotational flow and boundary layer flow that contains turbulent structures with considerable degree of spatial and temporal randomness and "entrained free stream" fluid which undergoes transition from irrotational to rotational state. As a consequence of the randomness present in the input flow of this interaction, its output is dynamic and the instantaneous structure of the flow is very different even from the "phase-locked" averaged structure let alone the long time-averaged flow.

During the deployment of the actuator, the upstream turbulent boundary layer structures and the free stream fluid are decelerated and squeezed by the lateral straining in the longitudinal direction as they approach the moving plate. At the same time a horseshoe vortex (HV) (seen in figure 2) starts to form over the moving plate and during the final stages of deployment it has been moved upstream while the incoming boundary layer turbulent structures are pushed and diverted upwards. These structures start scrubbing the upper part of the plate as they form a very thin and highly sheared wall layer developing over the moving upstream surface of the plate which generates a substantial amount of vorticity by the action of pressure gradients at the wall and its own motion as described by equations 4-5 and 4-6.

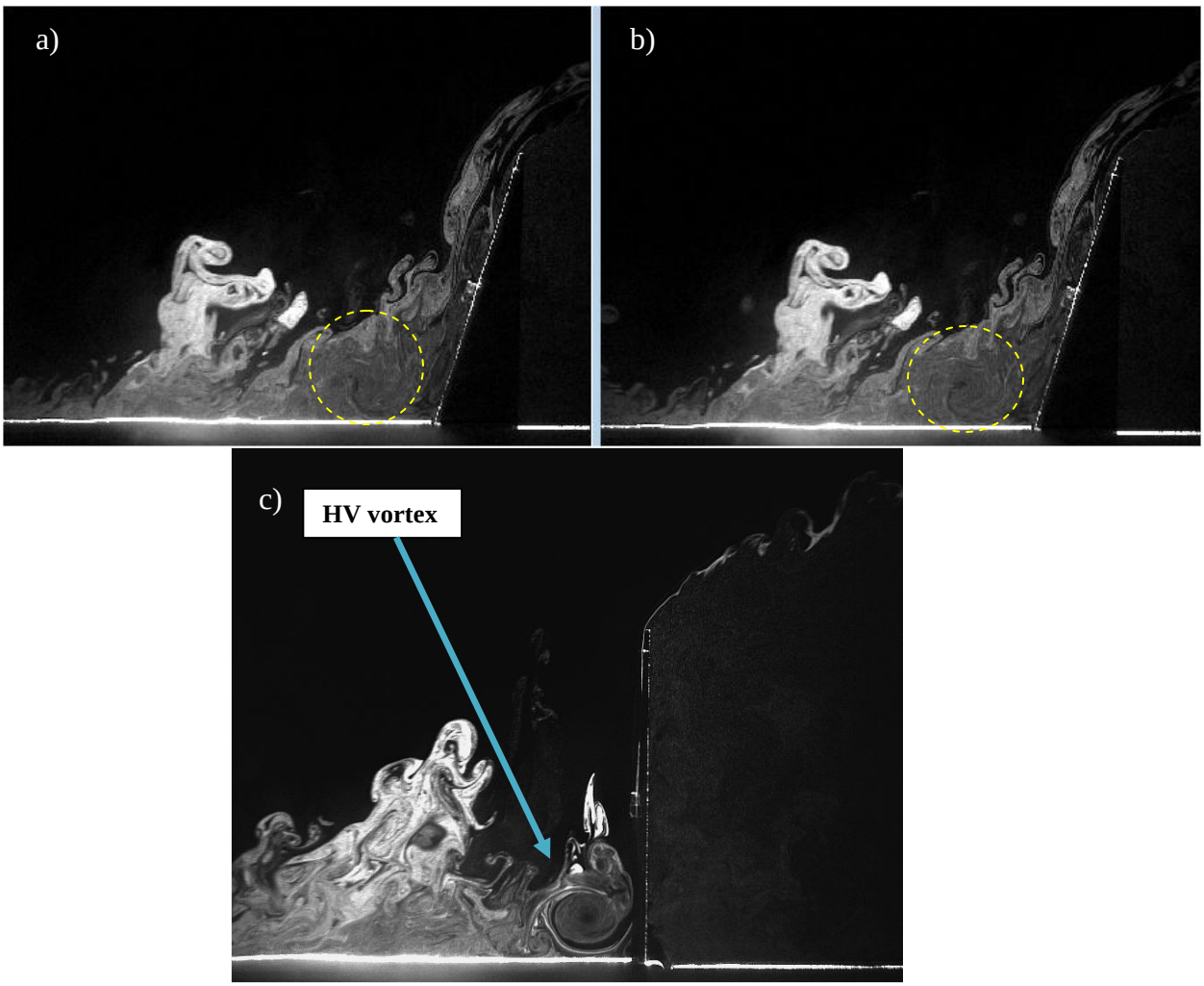

Figure 6-2: Upstream horseshoe vortex; a & b images sequence showing HV in early developing, in c HV is shown fully developed (these images are for low Str case)

Although this highly sheared wall layer is a not a conventional boundary layer since it is highly disrupted by huge external disturbances with scales much larger than its thickness, it will be treated as a boundary layer in the rest of this discussion. Its structure is very intermittent since is part-time turbulent and part-time laminar depending on whether a turbulent eddy from the incoming large scale boundary layer is scrubbing the moving plate or laminar "entrained free stream" fluid interacts with it. This partially turbulent and partially laminar boundary layer leaves the moving surface in the form of a separated shear layer which rolls up to form large scale vortices in the area between the wake and the free stream which are responsible for the

generation of the additional dynamic lift. Since the feeding boundary layer over the moving plate is intermittent the separated shear layer is also partly turbulent and partly laminar. It is not clear from the observations whether the laminar part can undergo or has undergone Helmholtz-Kelvin instability in the presence of large scale external turbulence in the neighborhood.

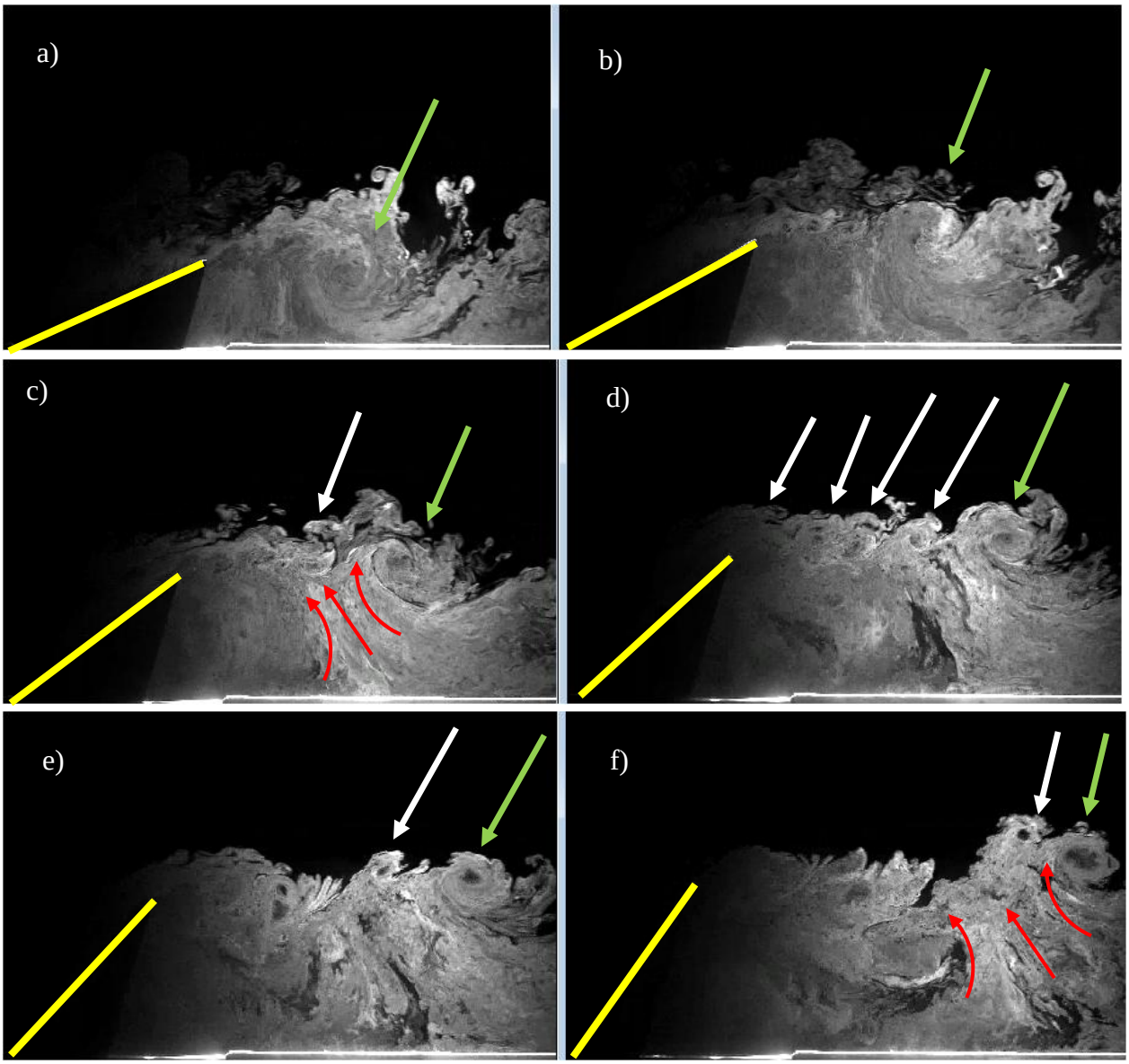

Figure 6-3: Vortical structures shed off the tip of the actuator, green arrow refers to initial CWR-TVS, images taken at 0.5c plane (Str=0.24. Re=68,200)

The most significant feature of the interaction of the moving winglet with the incoming flow developing over the upstream wall is the generation of vortical structures shed off the tip of the rotating panel. The evolution of the flow structures at the center of the flap (0.5c) is shown in sequence of images in figure 6-3 (also is shown in the video “Movie 1”, which has been obtained with a rate of 3,000 fpr). In this sequence, the green arrows refer a clock wise rotating tip vortical structure (CWR-TVS), which seems to be strengthening with the increase of the deployment angle fed by the low pressure region behind the panel.

The boundary layer separates the panel at its tip and an undulated shear layer is formed which undergoes deformation by the wake turbulence and tends to wrap around itself by the motion induced by the inrushing reverse flow in the wake.

In figure 6-4, the same structure (CWR-TVS) has been followed at off center plane (at 0.2 c), the structure (marked by the green arrow) seemed to move inward toward the center of the flap, while slowly moving downstream in figure 6-4a, 6-4b, and 6-4c, where the structure can still be seen at this plane, however, in 6-4d and 6-4e, it starts to disappear from this view. Then 6-4f, 6-4g and 6-4h it appears gradually again, and in 6-4i a vertical core of the structure can be seen while moving outward (toward the side edge), in 4j to 4l, it can be seen what appears to be the upper and lower part of the same vortical structure, which took the shape of a mushroom structure in this plane (likely to have a ring-shaped vortical structure. In the last three images, the lower side of this structure can be seen rotating in counter clockwise direction (CCWR-TVS).

To summarize, the CWR-TVS, seen in both planes 0.5c and 0.2c, is a vortical structure that shed of the tip of the moving panel at small angle, then this structure moves downstream at the same time it converges toward the center of the flap, then it starts to stretch again in the lateral

direction, in what seemed to be part of a ring vortical structure, where the upper part rotates in CW direction and the lower one rotates in CCW direction.

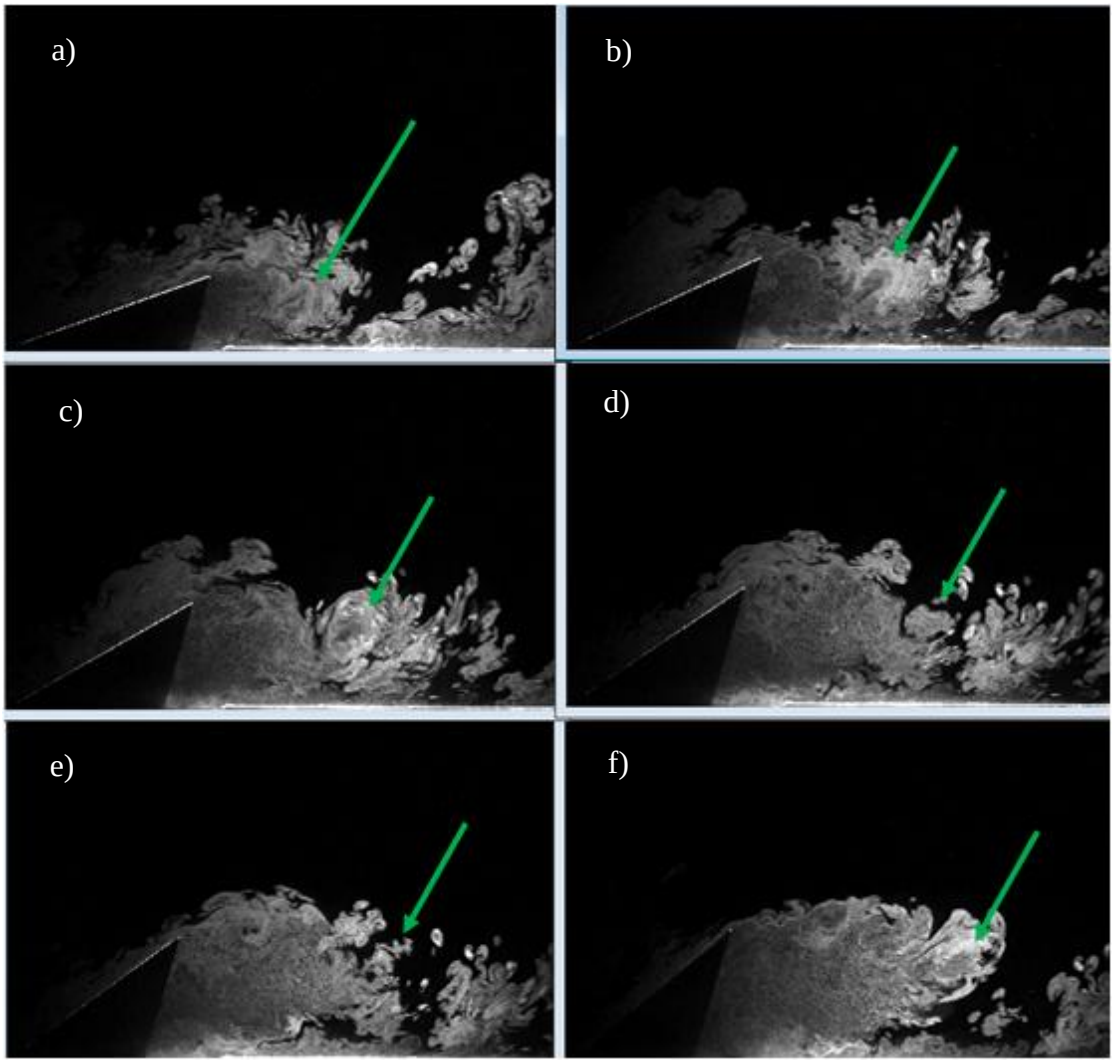

Figure 6-4: (a: f) Vortical structures shed off the tip of the actuator, green arrow show initial CWR-TVS at 0.2c (Str=0.24. Re=68,200)

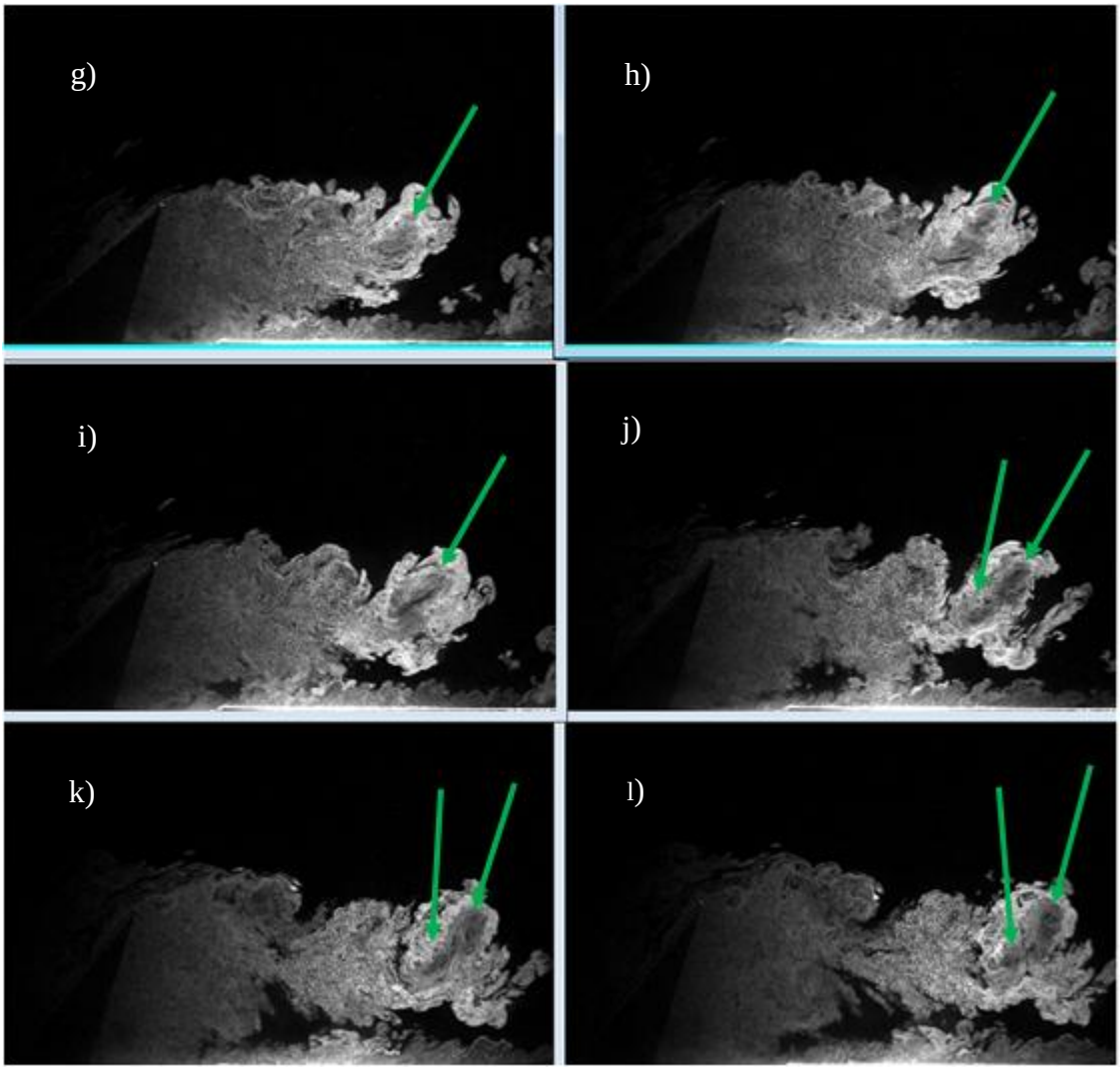

Figure 6-5 (g : l): Vortical structures shed off the tip of the actuator, green arrow show initial CWR-TVS at 0.2c (Str=0.24, Re=68,200)

The flow structures carrying this vorticity are part of the large scale recirculation zone formed in the wake of the moving panel. In between the two counter rotating structures fluid is erupted upwards suggesting the existence of a larger scale mushroom type vortical structure. This upward moving fluid is fed by the intense flow inrush over the stationary wall, which is directed towards the low pressure region developing in the wake of the moving panel.

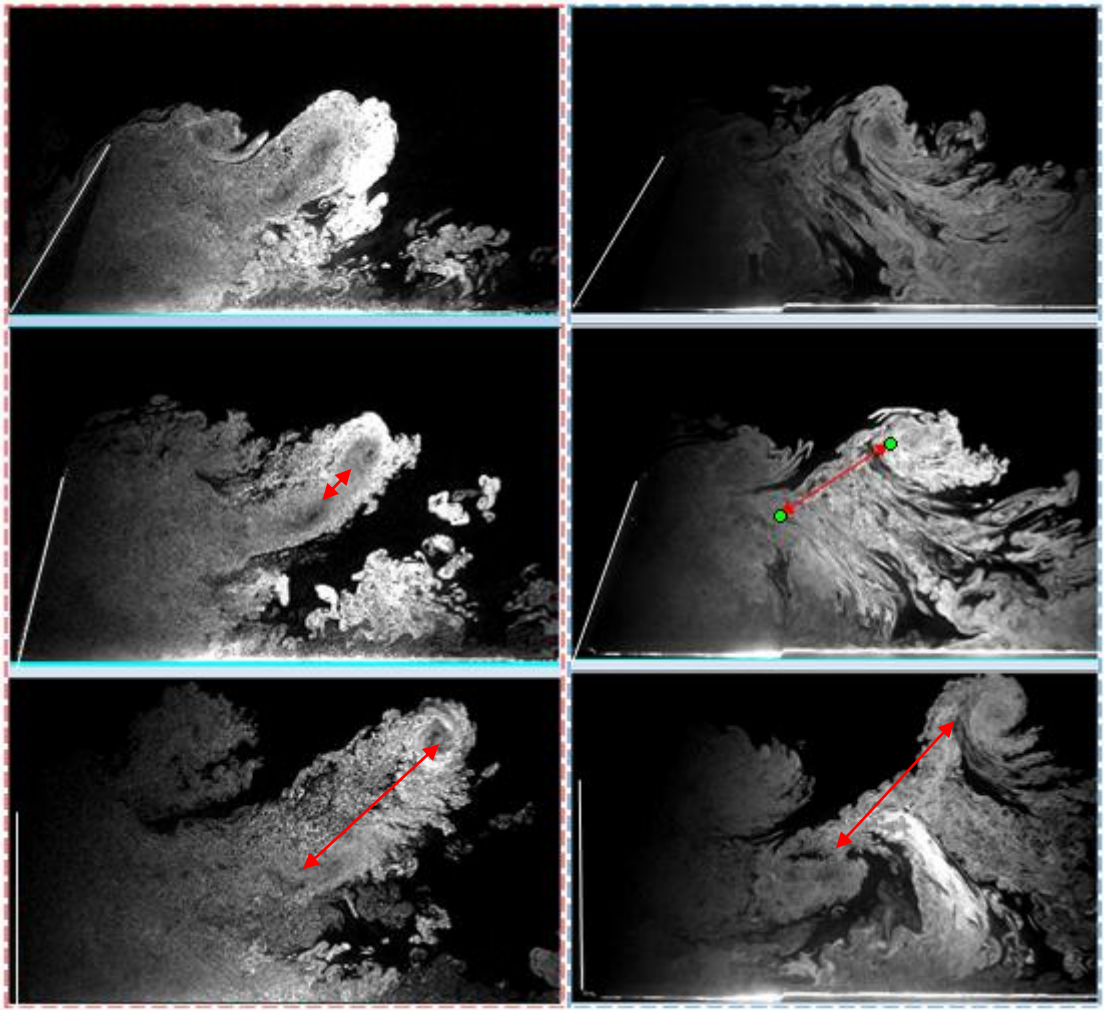

Figure 6-6: CWR-TVS developing at different Re, and higher Str, left column images at off-center plane (0.2c), right column at center plane (0.5c), flow at Re=45,500, Str=0.36

As the panel is further deployed additional TVSs are evident in the flow which move upwards and in the downstream direction. Four large scale CWR-TVSs are shown in figure 6-3d interconnected in a street like arrangement along the separated shear layer. It is the formation of the TVSs and the vorticity shed off the front face of the rotating panel which are responsible for the generation of the dynamic lift and drag forces. The presence of turbulence in the flow and particularly in the wake of the moving panel causes large distortion of the TVSs and induces mutual interaction among them, which may result in loss of their tracking in the subsequent images. A typical example of mutual interaction is shown in figure 3b where the first TVS has

been swept away by the stronger initial TVS while a new one starts to form close to the tip. As was explained earlier, in addition to the formation of TVSs, the inrushing reverse flow over the wind tunnel wall creates vorticity of opposite sign to that of TVS. This inrushing fluid also creates vorticity in the back surface of the panel as it moves towards the low pressure region of the tip. In that respect the large recirculatory motion in the wake of the panel results in the generation of vorticity opposite in sign to that of the TVS. The presence of strong turbulence in the wake distorts this CCWR-VS and its tracking is not quite obvious. It keeps growing, however, and reappears stronger than before when the panel is at about 55^o deployment angle as shown in figure 6-3f. The fact that is always connected to the initial CWR-TVS through the upward moving and slightly tilted backwards flow between them strongly suggests that they both belong to the same mushroom structure possibly in the form of a vortical ring, particularly if we associate it with images in figure 6-4j ,6-4k, and 6-4l. This structure appears to be the predominant characteristic in the wake of the panel during its transient rotational motion. Same structure appears in figure 6-5, which is taken for higher Strouhal number (Str =0.36) and lower Re=45,500 with freestream velocity U_0= 7.4m/s. In this figure all the flow characteristic in figures 6-3 and 6-4 seen to exist here as well, with only difference of the stretching of the vortical structure. This structure in higher Str case showed slower motion in the longitudinal direction, while it maintains its upward motion. In figure 6-3 the first TV is completely out of the camera view before the 90^o deployment angle is reached, however, in figure 6-5 the same TV shown at a distance equal to twice the actuator span length (c) at the time the panel reaches 90^o.

To further investigate this characteristic of the flow, we recorded the deployment at Str= 0.49 and Re =23,000. The same behavior seen extends (figure 6-6), where the 1^{st} TV travel slower downstream with the increase of Str and decrease of Re. In figure 6-6, the 1^{st} TV traveled only

about 1 c downstream at the time the panel reached 90^{o}, moreover, the TV motion barely seen between figure 6-6a and b.

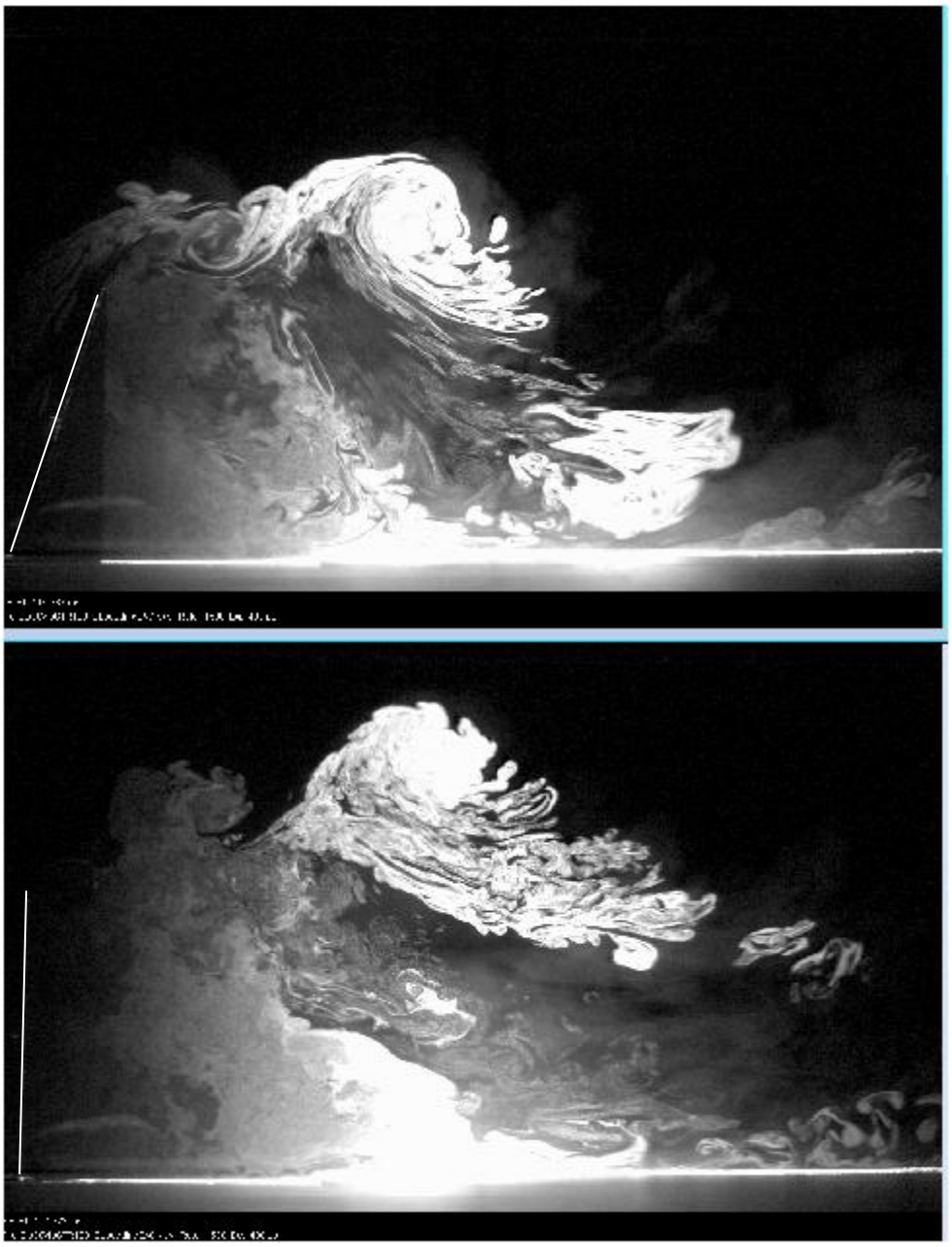

Figure 6-7: CWR-TVS position a) at 75^{o}, b) at 90^{o}, imaging at 0.5 c plane (flow at Re=23,000, Str=0.49)

At the end of deployment most of the TVSs are swept away and only one new TVS is formed which apparently is the last one which is responsible for the sudden drop in drag (see figure 6-7). After the end of the deployment, the shear layer is not wrapped around itself anymore and it

appears as an un-undulated shearing region between the faster moving free stream flow above and the wake of the panel below.

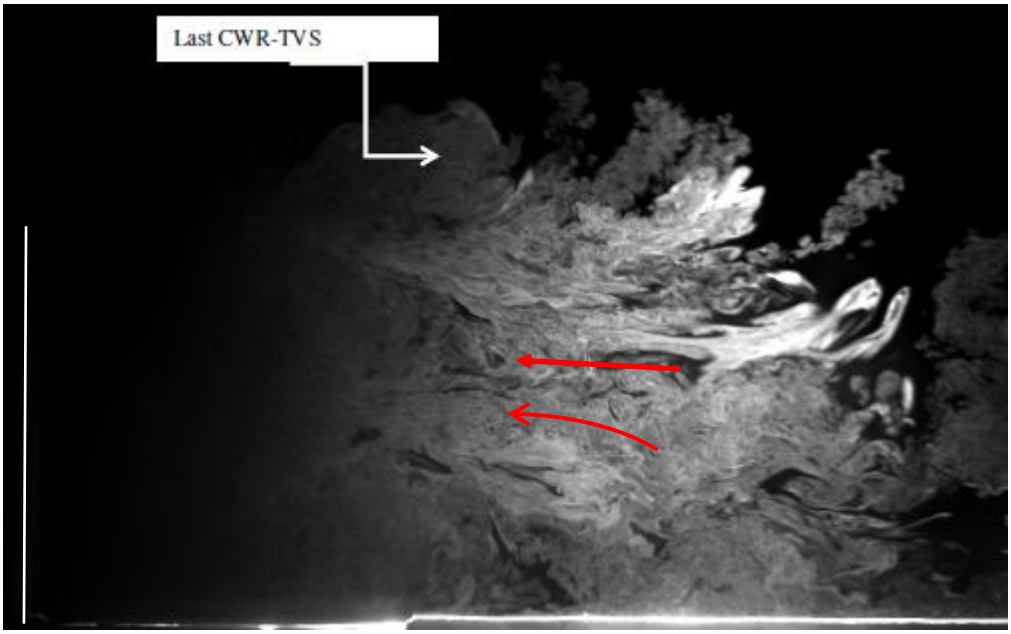

Figure 6-8: Flow Visualization with the flap at 90^o at 0.5c, (Re=68,200, Str=0.24)

In figure 6-8, which is taken off center at 0.2c plane, with the panel deployed at about 48^o, a number of CWR-TVSs are present starting with the shear layer vortices immediately leaving the tip of the top edge of the panel before they wrapped around to form a large scale TVS.

In the most downstream structure a CCWR-VS was identified bundled with the upstream CWR-TVS with substantial upward and backward tilted induced flow between them. The origin of this CCWR-VS could not be traced to any wall activities as in the previously discussed case of the CCWR-VS at the plane of symmetry which was observed to be formed near the wall. Although this CCWR-VS showing in figure 8 may well have been formed near the wall at a location outside the 0.2c plane, another explanation is possible. Most probably, both the CWR and the CCWR parts belong to the same leg of a vortical structure which has a circular shape in the spanwise direction and the CCWR part is the result of a cross section of the same vortical

structure. Such a three dimensional vortical structure may have been formed by the concurrent shedding of shear layer vorticity around the whole perimeter of the panel which includes not only the top edge but its two lateral edges which can shed vorticity oriented on a vertical plane. Thus the vortical structure initially consists of two legs on vertical planes apart by the width of the panel connected with the horizontal part to form a single continuous structure which is been distorted by the incoming boundary layer turbulence. This structure as it is transported downstream becomes more circular and because of the inrush of lateral fluid towards the low pressure wake of the panel, its two legs are re-orientated towards the middle plane giving the shape of an omega (Ω). This shape can definitely explain the appearance of the two opposite rotating vortical structures visualized by the planar laser sheet at 0.2c.

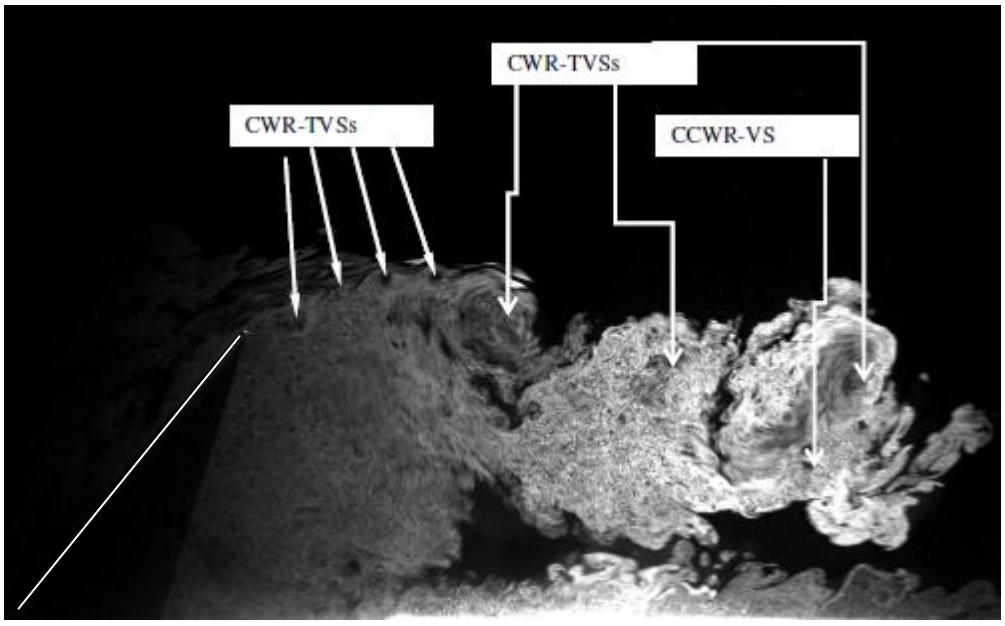

Figure 6-9: Flow visualization with laser sheet at 0.2c with flap at 48^{o} deployment (Re=68,200, Str=0.24)

In order to test this hypothesis the laser sheet was turned to become parallel to the tunnel wall and two additional flow visualization experiments were carried out. The evolution of the flow structure as a function of time can be observed in the video stored in (see Movie 2). In the beginning, typical boundary layer structures can be observed which usually are present in the

outer part of the flow. Since the boundary layer thickness is about 5 cm while the laser sheet is located at a distance y=9cm from the wall only the tip of the instantaneous structures is visualized. Figure 6-9 shows a picture of the flow with several of these outer wall structures to be present while the panel is located at 61^o deployment angle. The panel as it deploys pushed upwards fluid the tip of which starts to be noticeable at this frame while four frames later, as shown in figure 6-10, is clearly visible. In figure 6-11, when the panel is at 63^o, the appearance of a low concentration tube is observed which, most probably, is associated with the horizontal core of the vortical structure shed off the horizontal edge of the panel. This vortex core is connected to the two counter-rotating structures visualized in the next figure 6-12 with the panel at 63.2 deployment angle. These two structures move apart away from each other in the frame shown in figure 6-13 when the panel is at 65^o after it had crossed the laser sheet while there is a strong induced reversed flow between them at the plane of symmetry. The two structures are been transported slowly by the flow in the downstream direction while there is a stenosis of the visualized wake behind them, as shown in figure 6-14, which is associated with the inrushing fluid from the two lateral directions towards the plane of symmetry where the pressure is very low. Finally this stenosis is further stretched by the reverse flow and becomes quite narrow at 83^o deployment (figure 6-15) while large vortical structures are formed through wrapping around of the shear layers shed off by the two lateral edges of the panel. While this Ω-like structure has been observed at the y=9cm plane of visualization, it was also possible to identify a rotating structures at the y=2cm plane of the laser sheet, shown in figure 6-16, which appears to be lower in strength. This may be due to the strong interaction of these structures with the near wall turbulence, and the low incoming upstream flow velocity at the position of the BL, which may

have completely distorted their rotational characteristics or the vorticity carried by these structures may be rather weak.

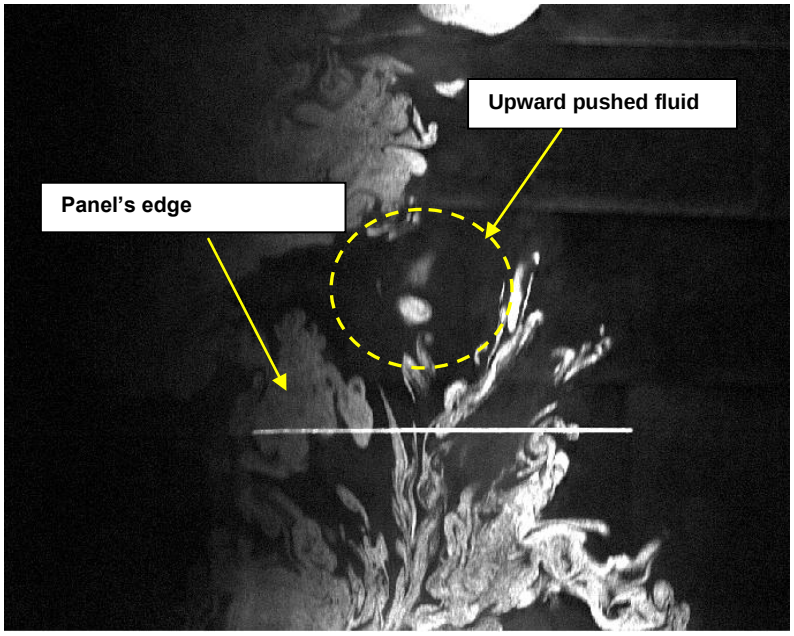

Figure 6-10: Flow visualization with laser sheet at y=9cm with panel at 61^{o} deployment. Flow with Re=68,200 & Str=0.24

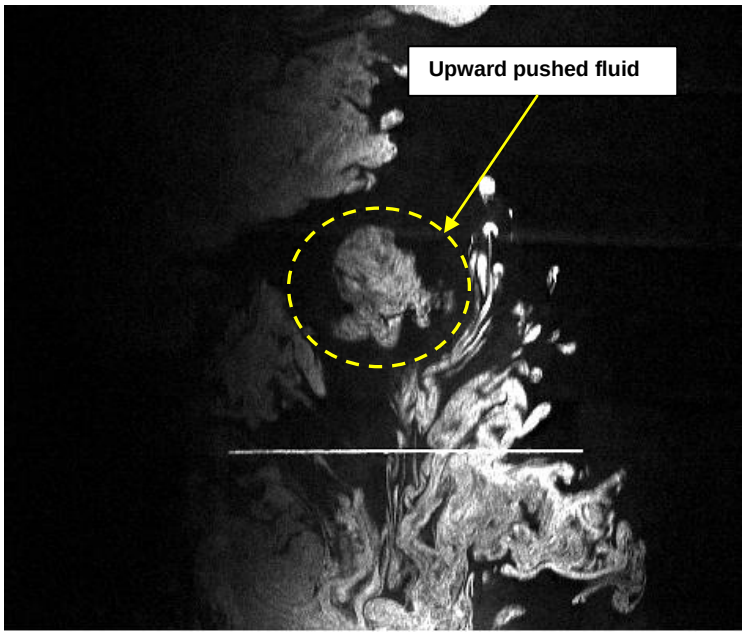

Figure 6-11: Flow visualization with laser sheet at y=9cm with panel at 61.6^{o} deployment. Flow with Re=68,000, Str=0.24

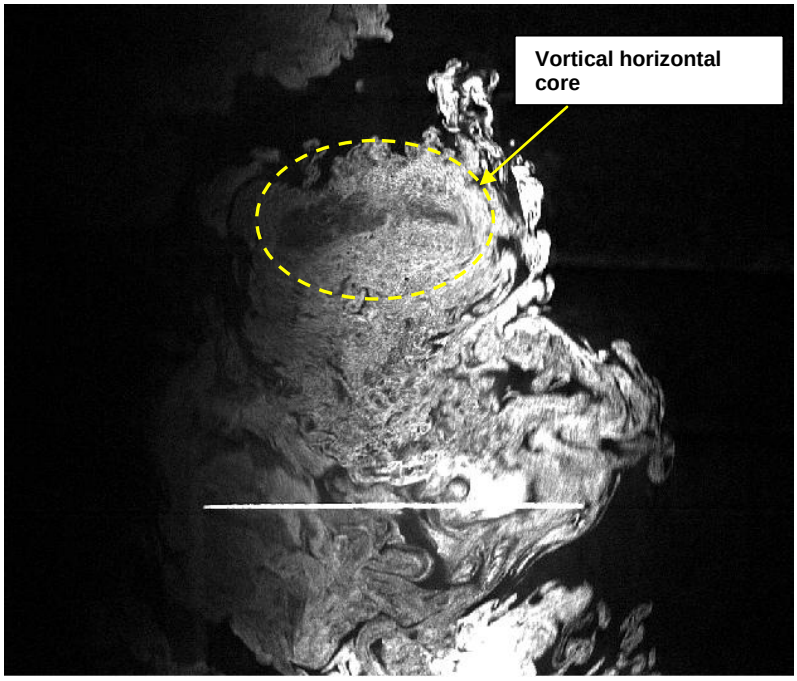

Figure 6-12: Flow visualization with laser sheet at y=9cm with panel at 63^{o} deployment.

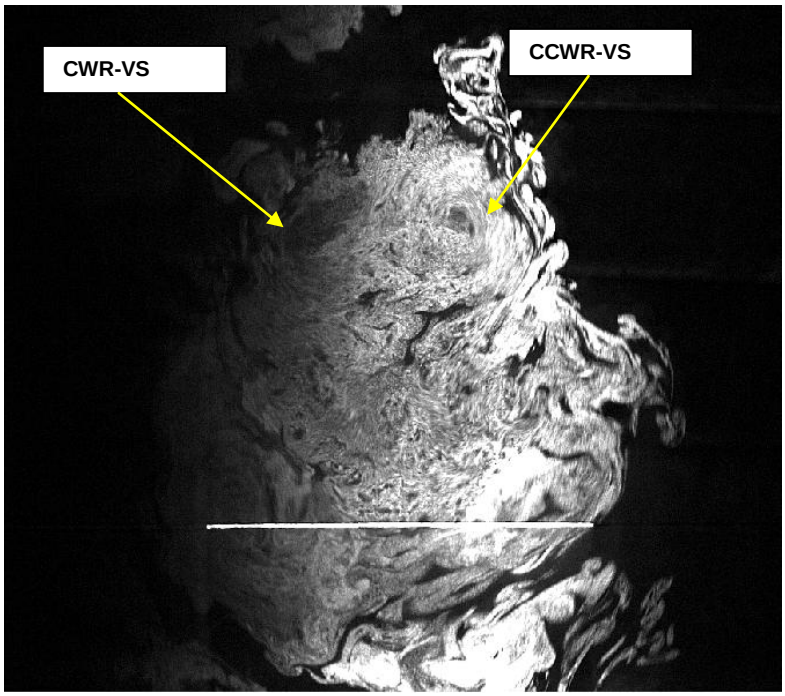

Figure 6-13: Flow visualization with laser sheet at y=9cm with panel at 63.2^{o} deployment.

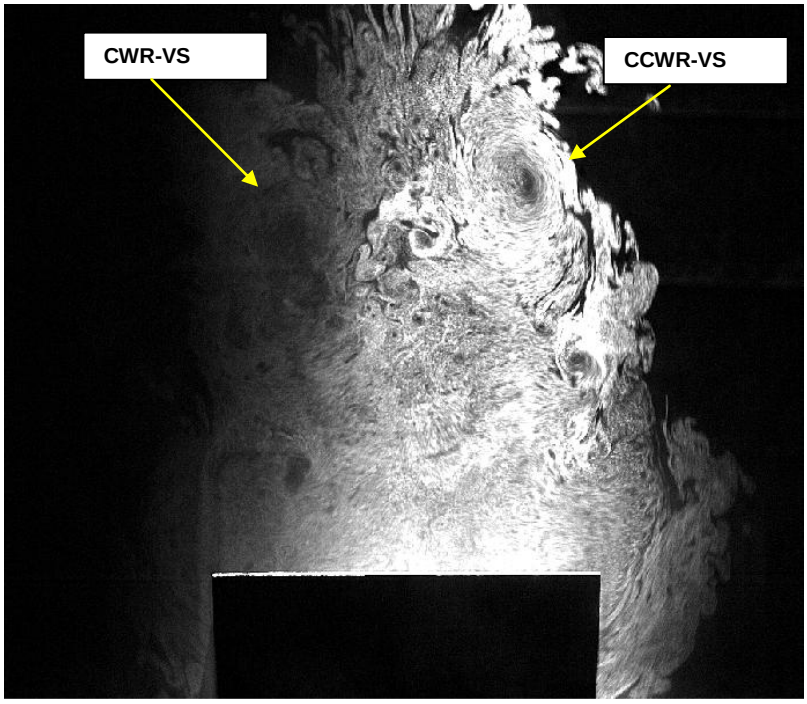

Figure 6-14: Flow visualization with laser sheet at y=9cm with panel at 65^{o} deployment

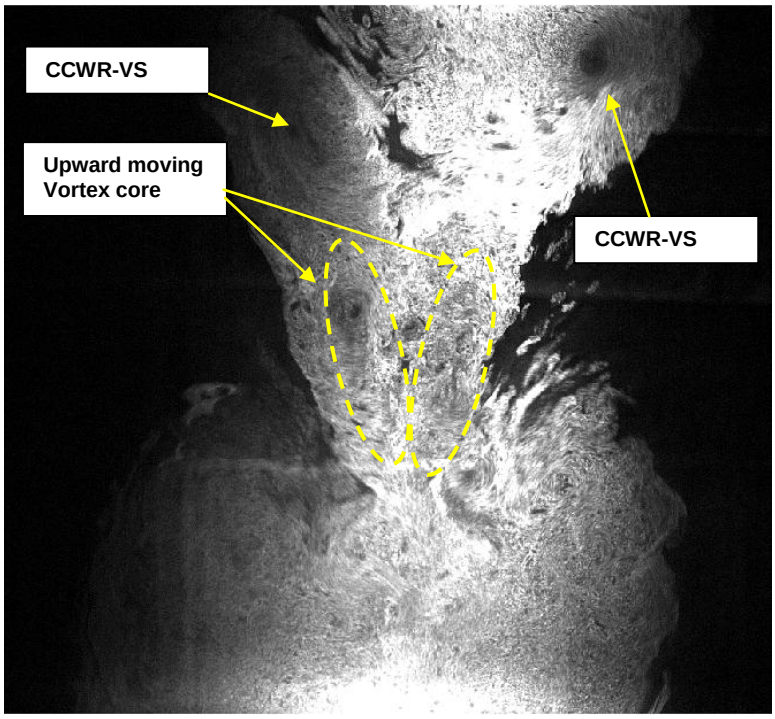

Figure 6-15: Flow visualization with laser sheet at y=9cm with panel at 73^{o} deployment

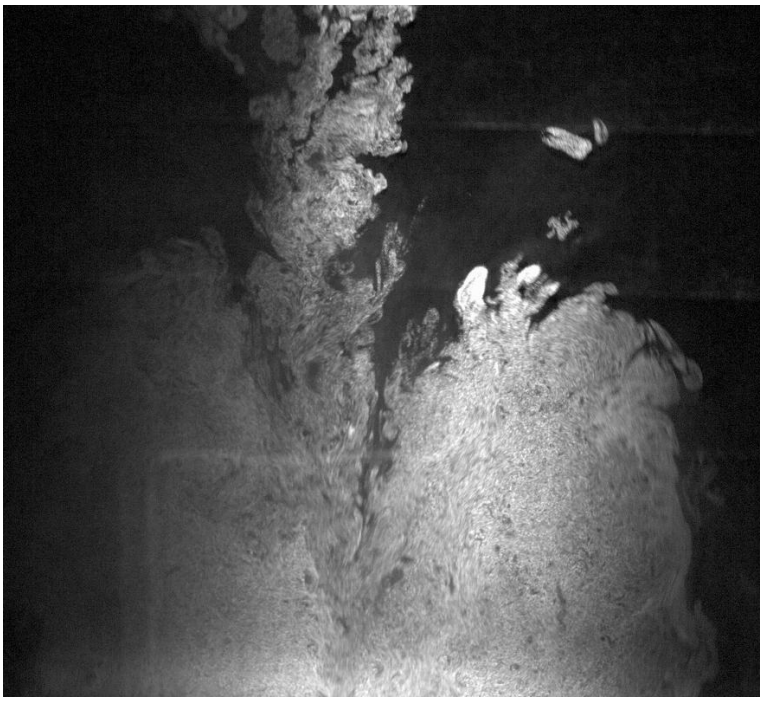

Figure 6-16: Flow visualization with laser sheet at y=9cm with panel at 83^{o} deployment

Figure 6-17: Flow visualization with laser sheet at y=2cm with panel at 25^{o} deployment (flow at Re=68,200, Str=0.24)

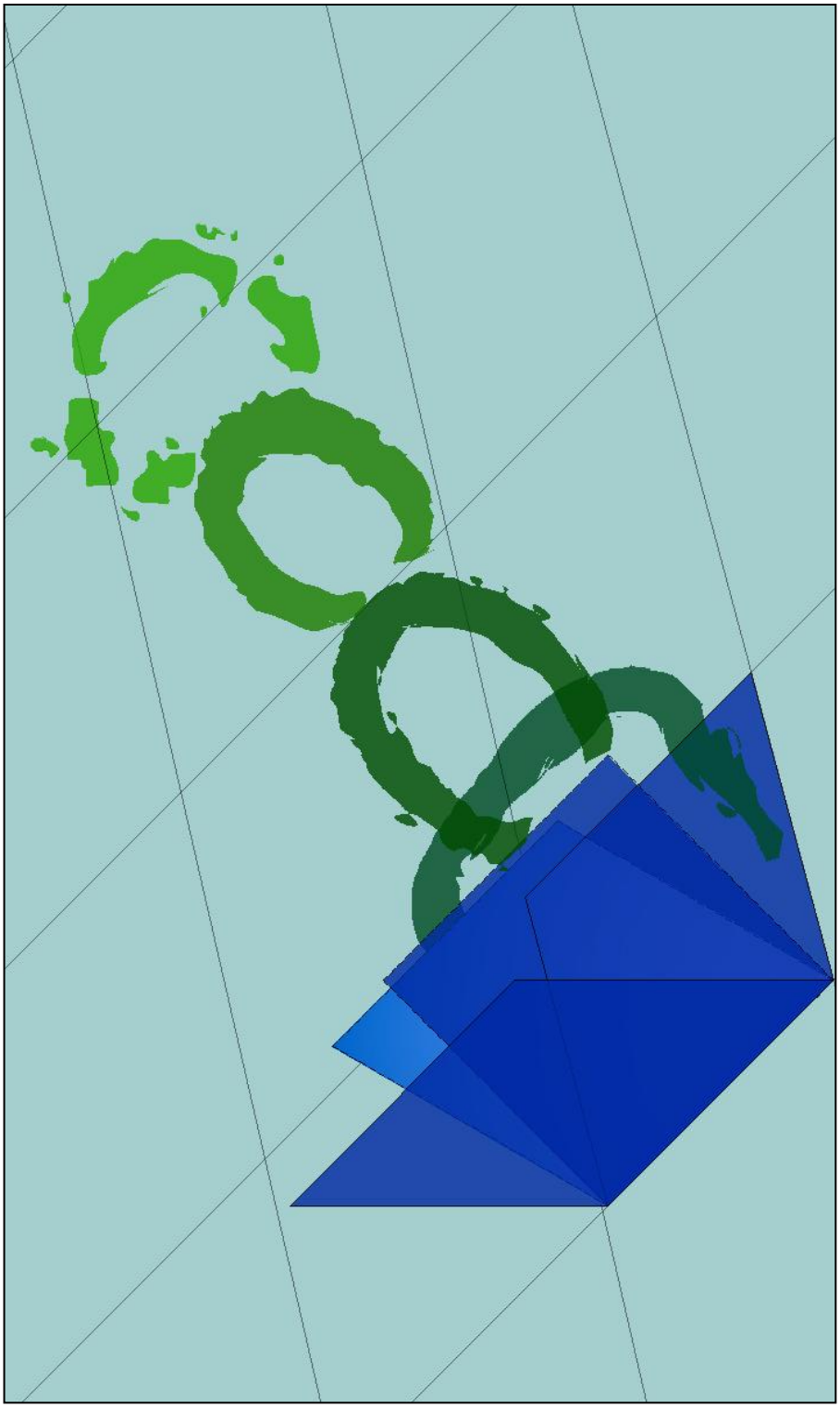

Figure 6-18: Conceptual structure for the first tip vortex (CWR-TVS) which seen in figure 6-3 and 6-4

6.2.2 Upstream effects during deployment

A series of flow visualization experiments were conducted focusing on the incoming boundary layer flow upstream of the panel (see Movie 3).Figure 6-17 shows a sequence of 11 images extracted out of this video during the panel deployment. The evolution of a typical large scale boundary layer structure (BLS) at Re_θ=3,400 is depicted in first image as it approaches the deploying winglet. A compressive straining of the BLS can be observed in the longitudinal direction while an expansive straining in the lateral direction is present as the fluid is decelerated in the longitudinal direction and then it is diverted over the panel or in the lateral directions. It is also evident that a stagnation point occurs when the panel is at 57.5^o (figure 17.1) at about 1/5h. The flow below that starts to separation and a recirculatory motion is observed at the root of the panel which eventually leads to the appearance of a horse vortex (HV) upstream of the panel with flow separation above the stationary wall of the wind tunnel. This stagnation point moves upwards to about 0.3h as the deployment progresses and the HV is more visible.

As this particular BLS is decelerated and compressed to a much thinner structure as it goes over the rotating panel, it wraps around the CWR-TSV generated at its tip as a very thin layer while there is a dark unseeded layer of free steam fluid between this and the proceeding structure. Thus the CWR-TSV is a rotating multi-layer structure formed by sandwiching piled up upstream BLS.

The HV is clearly evident in several of the images of figure 17. As the typical BLS approaches the moving panel first interacts with the HV at about a distance of x/h=-0.4 and then it starts to be compressed in the streamwise direction. Eventually it reaches the moving plate and it is swept away in the shear wall layer upwards towards the tip where it separates. This HV during the final stages of the panel deployment and immediately after when the flow adjusts to a steady state development has the characteristics of the turbulent horseshow vortex described by Agui &

Andreopoulos (1995) for the case of a high Reynolds number three dimensional turbulent boundary layer flow formed in front of a wall mounted cylinder. The HV in the present flow wonders considerably in both longitudinal and normal directions while exhibiting an intermittent strength which induces the generation of opposite rotating vortices at the wall.

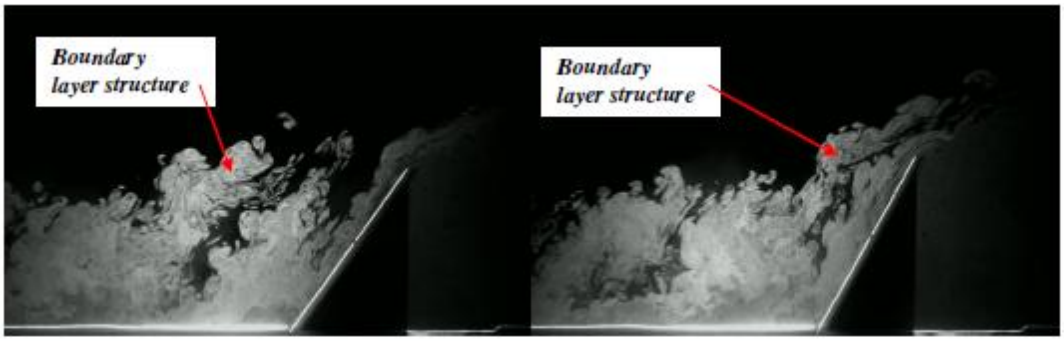

(1): Panel at 57.5°

(2): Panel at 64°

(3): Panel at 65.75°

(4): Panel at 67.5°

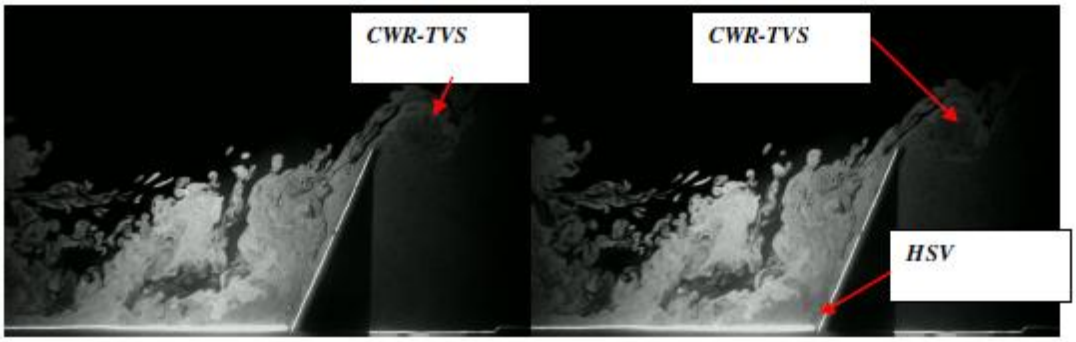

(6): Panel at 68.5°

(5): Panel at 69°

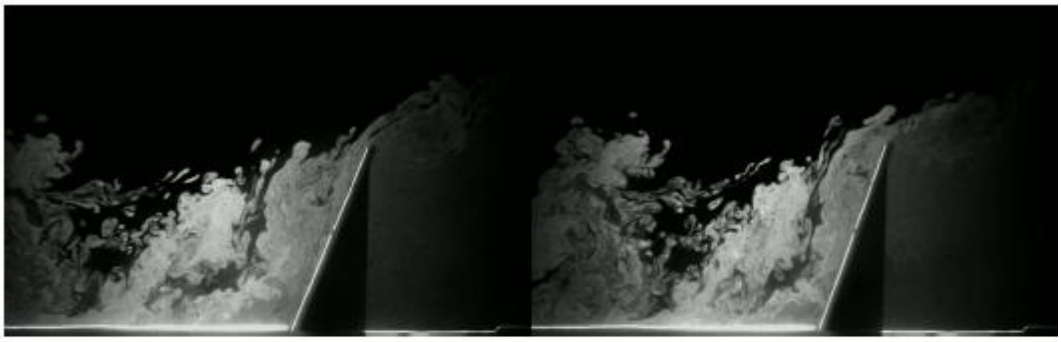

(7): Panel at 71.5°

(8): Panel at 74°

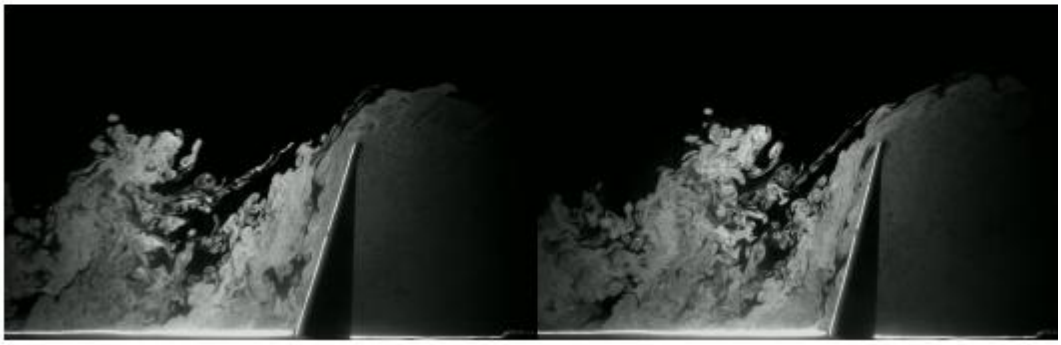

(9): Panel at 76.5°

(10): Panel at 79°

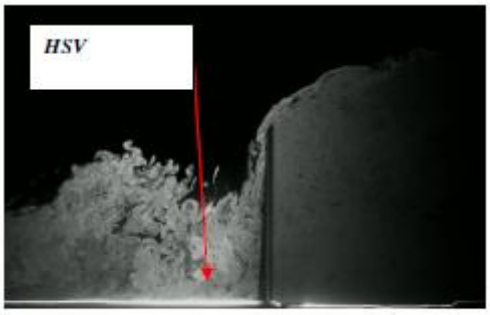

(11): Panel at 90°

Figure 6-19: (1) through (11): Sequence of flow visualization images during the interaction of the deploying panel with the incoming boundary layer flow obtained in flow with Re=68,200 & Str=0.24.

This HV does not contribute to the generation of excess dynamic forces on the panel. The Str=0.03 case has shown the development of HV during the last stages of the actuator deployment with very minimal dynamic drag above its static one. In general the HV affects the late stages of the flow structure during the panel deployment and the steady state flow structure

after the end of the deployment since it appears that it reduces the steady-state drag by diverting upwards the incoming boundary layer fluid part of which does not decelerate to stagnation on the front face of plate itself. In fact in earlier wall proximity studies (Pierides 2010) it has been measured that the Cd is considerable less when the plate touches the wall than its corresponding value when the plate is far away from the wall. Part of this reduction in Cd is due to momentum losses associated with the incoming upstream boundary layer and part is due to the HV formation upstream of the normal to the wall plate.

6.3 TR-PIV measurements

6.3.1 Experimental Settings and approach

The main objective of the PIV experiments is to investigate the quantitative effect of the change of the Strouhal number on the flow around the rotating panel during the deployment. In addition, a comparison between the steady state case, when for the actuator is fully deployed and the impulsive deployment at different Str. Three cases of different Strouhal number were considered in this experimental setup. The field of view included in these experiments followed two locations in the streamwise-normal-to-wall direction at the center plane and off-center at 0.2c from the actuator edge (see figure 6-1a). These experiments are carried out at constant Reynolds number of 23,000; and freestream velocity of 3.7 m/s. The lower Reynolds number was chosen here for two reasons. First, it would allow achieving higher Str. Cases, as Str is inversely proportional to the freestream velocity U_0. Second, obtaining high quality TR-PIV data, where the second Re of 68,200 used in the flow visualization cases produced lower quality PIV results as discussed in the first part of this thesis.

A particular attention is given to the flow behind the flap, as it's believed from the flow visualization analysis that the vortical structure generated in the wake of the actuator perhaps the major contributor to the enhancement of the aerodynamics of the actuator.

The rate of the image acquisition and PIV realization for all cases was 5000 per second. This was determined from initial evaluation for the PIV quality at this rate, which proved to be suitable for the range of the experiments presented here.

In all experiments, post triggering is used to trigger the high speed camera, while the camera memory is able to acquire more than 6 sec of real-time flow images at the 5000 fpr. This is relatively long duration of acquisition which allowed eliminating any complicated synchronization between the actuator and the camera system. In these streamwise-normal-to-wall FOV experiments the camera was mounted on a tripod facing the optically accessible side of the wind tunnel, while the flow moves left to right.

The camera recording is then transferred to the computer in a video format files, these files are used to extract the individual raw images and adjusting the intensity level using matlab. All the raw images are named accordingly and transferred to INSIGHT 3G for PIV processing (also see the flow chart shown in figure 3-15 for complete summary of the PIV processing).

6.3.2 Results and discussion:

Figure 6-20 and 6-21 show sequence of streamlines plots of the flow in the instant wake of the actuator during the deployment at Str =0.27. In the left hand side column the PIV data is taken at the center plan of the actuator (0.5c), while on the right hand side, the streamlines plots are carried out at off-center-plan at 0.2c.

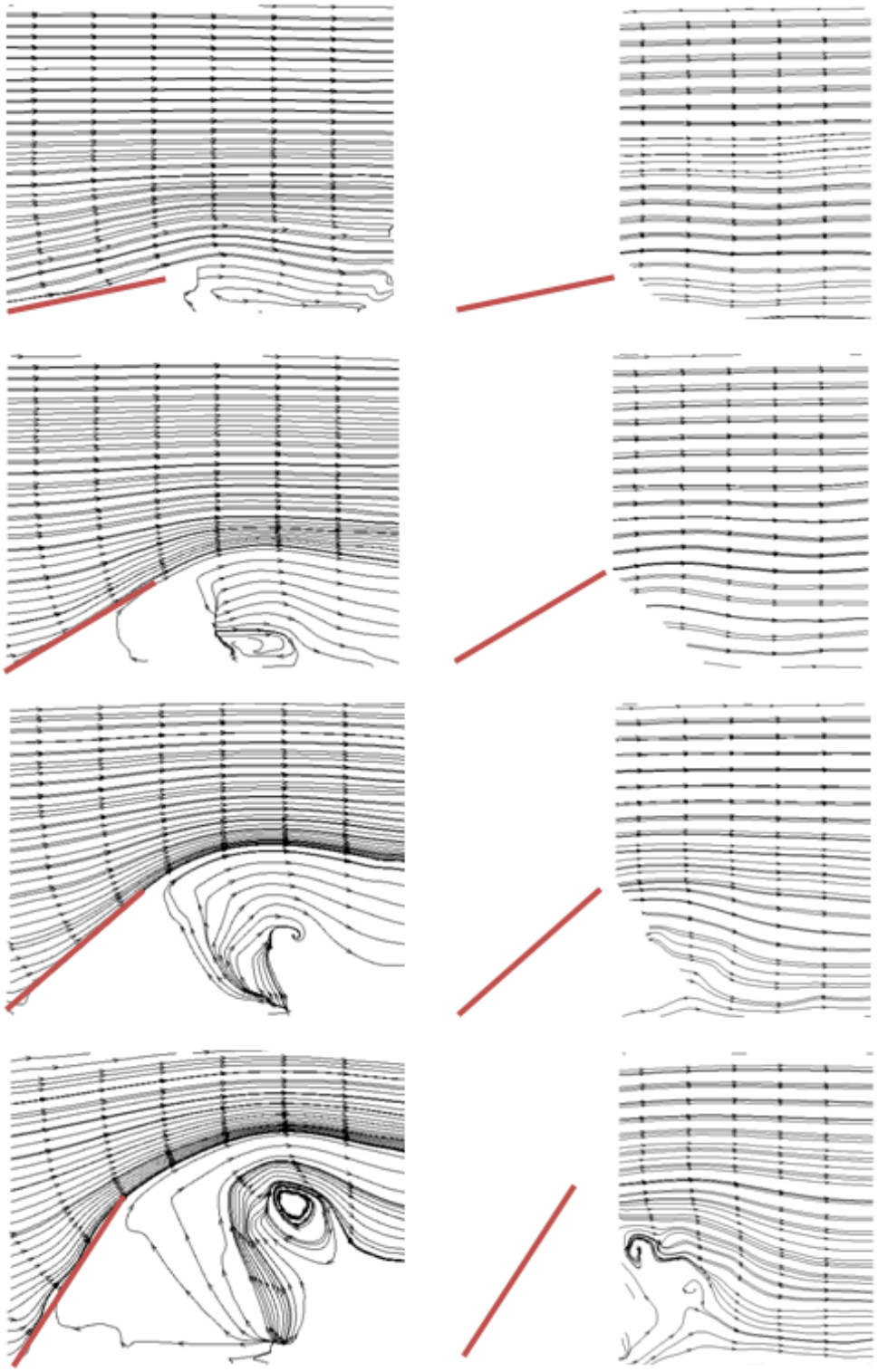

Figure 6-20: 1st set of instantaneous Streamlines sequence of during the actuator deployment calculated from TR-PIV measurements for Str= 0.27 and U= 3.7m/s, left column at center plane of the actuator (0.5c), right column at plane 0.2c

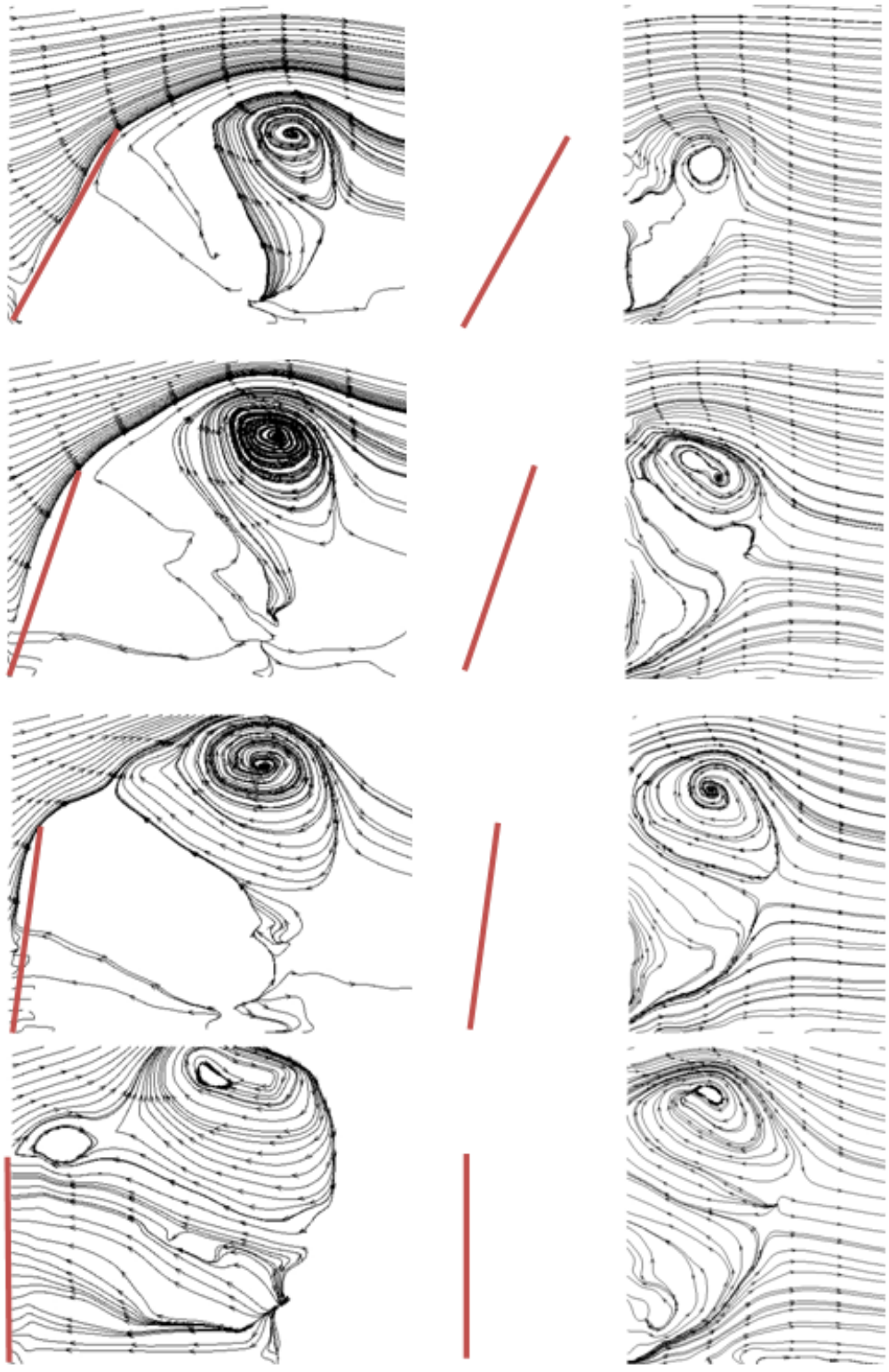

Figure 6-21: 2nd set of instantaneous Streamlines sequence of plots during actuator deployment calculated from TR-PIV measurements for Str= 0.27 and U= 3.7m/s, <u>left</u> column at center plane of the actuator (0.5c), <u>right</u> column at plane 0.2c

In the sequence representing the center plan of the actuator, at early deployment angle the initial tip vortex (CW-TVS) is seen to be created. This initial CW-TVS is then follows a trajectory mostly in the y-direction, with almost no translation in the x-direction, at the same time the vortex shown to be strengthen as the deployment angle increases. As discussed previously in the flow visualization experiments this vortex shown to travel in x-direction slower in case of lower Re. This thought to be a result of the strength of the momentum of the incoming flow that is lower in the present case. The vortex strength can also be seen in the growing size of circular streamlines. In the off-center plan, the vortex appears spatially delayed, as it's believed to wrap around the actuator body as presented on figure (6-18). At the end of the deployment another vortex appears to be created at the tip of the actuator.

In figure (6-23), sequence of 12-contour-plots of the vorticity during the deployment at Str=0.27. In the first three plots, strong vorticity fields are seen to be generated on the surface of the actuator. This vorticity is thought to feed creation of the CW-TVS, and it's a result of the high acceleration of the actuator during the early part of the deployment, which is discussed in chapter 6 referring to the encoder signal, the incoming boundary layer flow is confronted with an obstruction with even high local Str, as the incoming flow is lower closer to the wall. Also, in the early part of the deployment, the HV is not yet established. This level of wall vorticity generated is reduced spatially in later time during the deployment as can be seen in the sequence following third image. On the other hand, as previously seen in the streamlines plots (figure 6-20 & 6-21) , the CW-TVS appears very early in the deployment ($<15^0$), however, in the vorticity contour plots, The CW-TVS strength appears stronger in the bottom side closer to the tip.

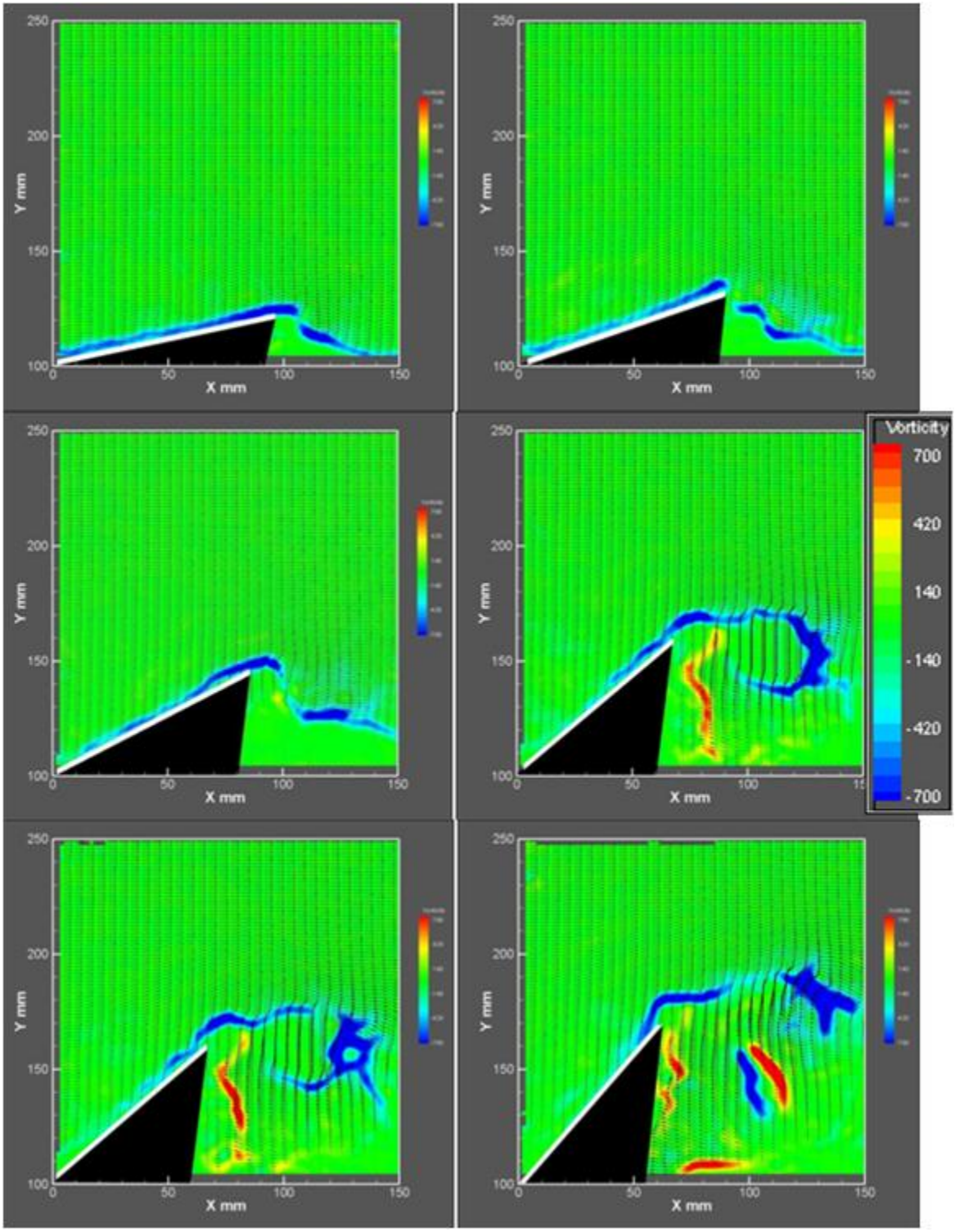

Figure 6-22: Instantaneous Vorticity contours for the flow during the deployment (U=3.7 m/s, Re= 23,000, Str=0.27) (the arrows in black show the velocity vectors)

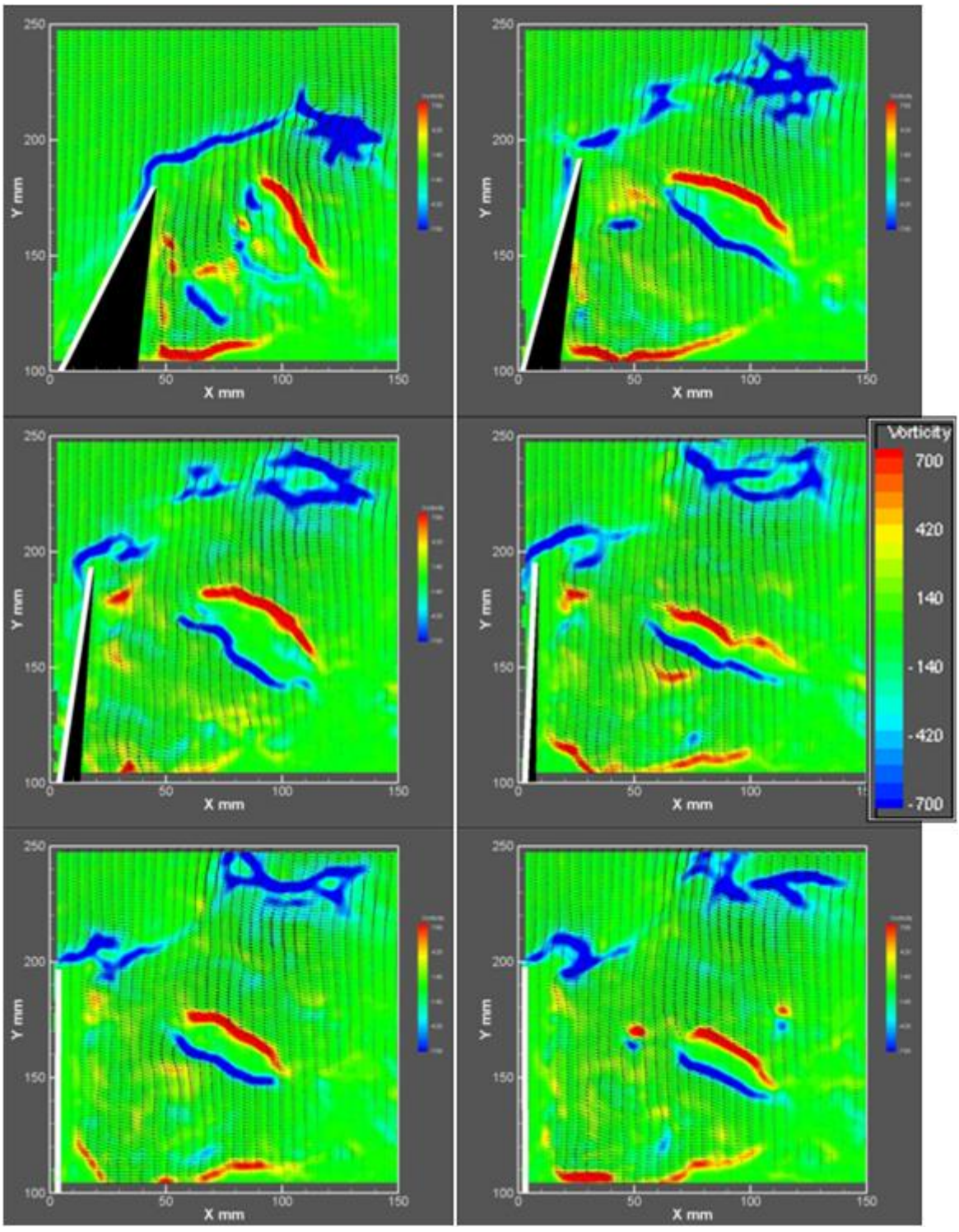

Figure 6-23: Instantaneous Vorticity contours for the flow during the deployment (U=3.7 m/s, Re= 23,000, Str=0.27), (the arrows in black show the velocity vectors)

A t the time the actuator reaches 45^o, the CW-TVS is then fully seen with equal strength all around its own circular shape. Also, in figure 6-23, The CW-TVS is seen to be dominating the flow field during the deployment, the structure detached in early stages from the tip of the actuator, however, it travels very slowly in the x-direction. This believed to partly redirect the flow to dynamically feed the CW-TVS structure, while simultaneously the low pressure region behind the actuator, which is mostly the region responsible to the drag, is in a part spatially shielded by CW-TVS. At the same time, this low pressure region behind the actuator is also dynamically challenged by another low pressure region created by the relatively large stationary CW-TVS.

Later in the deployment at about 80^o, the initial CW-TVS appears to break, and other CW-TVS is created at the tip of the actuator. This is seen to be quantitatively and qualitatively different for different Str, as seen in the plots in figure 6-24. This figure shows the vorticity computed at the instant the actuator reaches 90^o. The third vorticity plot in this figure is for Str=0.54 case, which shows only one CW-TVS is created during the deployment, in the mean time, stronger vorticity field is apparent in this case compare to the case with Str=027, which is shown in the middle plot. In the top plot in figure 6-24, a much lower vorticity is seen while the Str=0.03. Figure 6-25 shows the average vorticity, where the actuator kept at 90^0 to exclude any deployment effect. Figures 6-24 and 6-25 show clearly the strong effect of the increase Str on the increase of vorticity field in the wake region of the actuator.

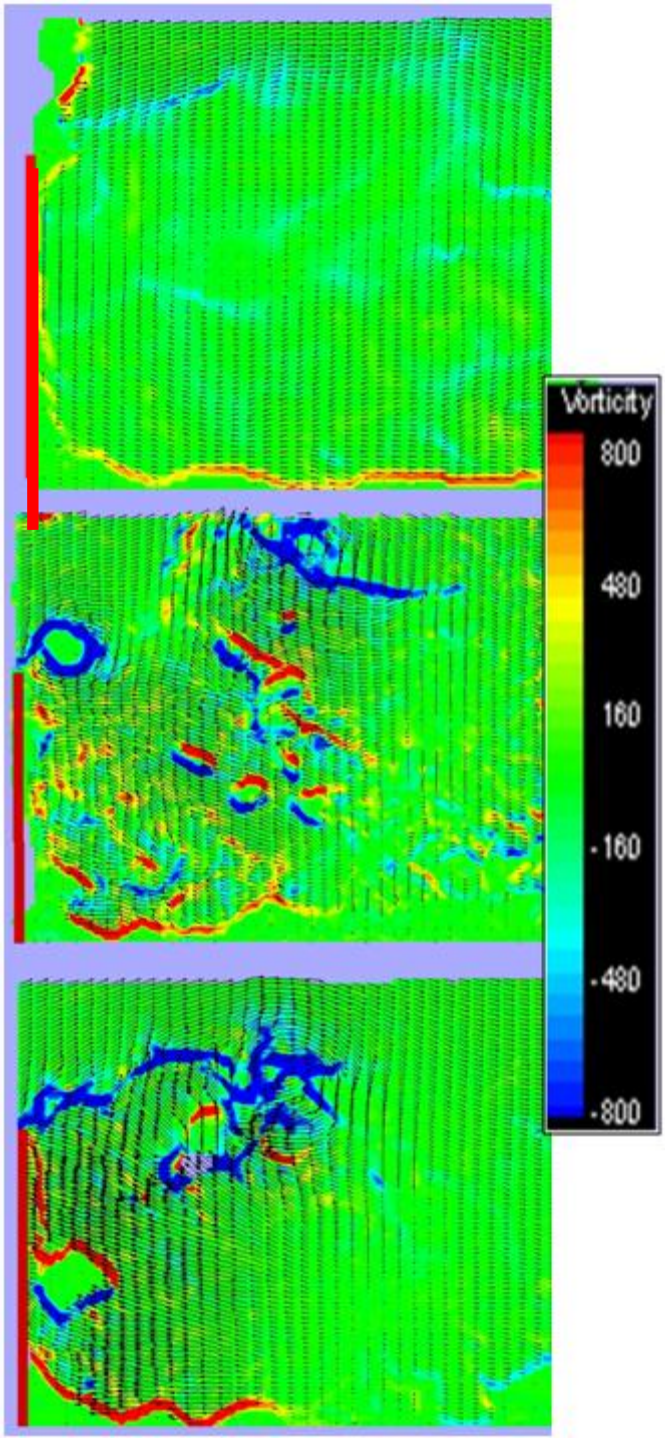

Figure 6-24: Instantaneous Vorticity contour for three different Str. Cases, at the instant the actuator reaches full deployment 90 degree, (top to bottom) Str=0.03, 0.27, 0.54, U=3.7m/s, Re=23,000 (the arrows in black show the velocity vectors)

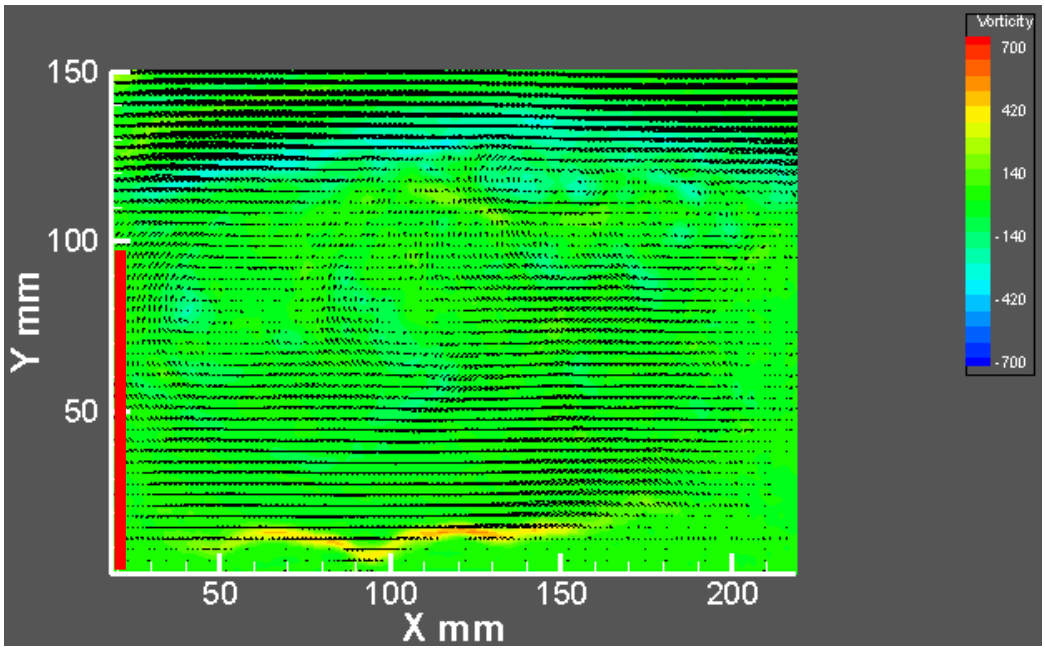

Figure 6-25: Average Vorticity Contour calculated from the steady state experiment at U=3.7m/s, Re=23,000 (the arrows in black show the velocity vectors)

Another look at the differences between the flow at the center plan and the off-center plan (closer to the side-tip at 0.2 c), figure 6-26 show a comparison of the vorticity contour plots both for Str=0.27 and at the instant the actuator reaches 90^0, it's seen in this figure that the CW-TVS is much stronger at the center plan.

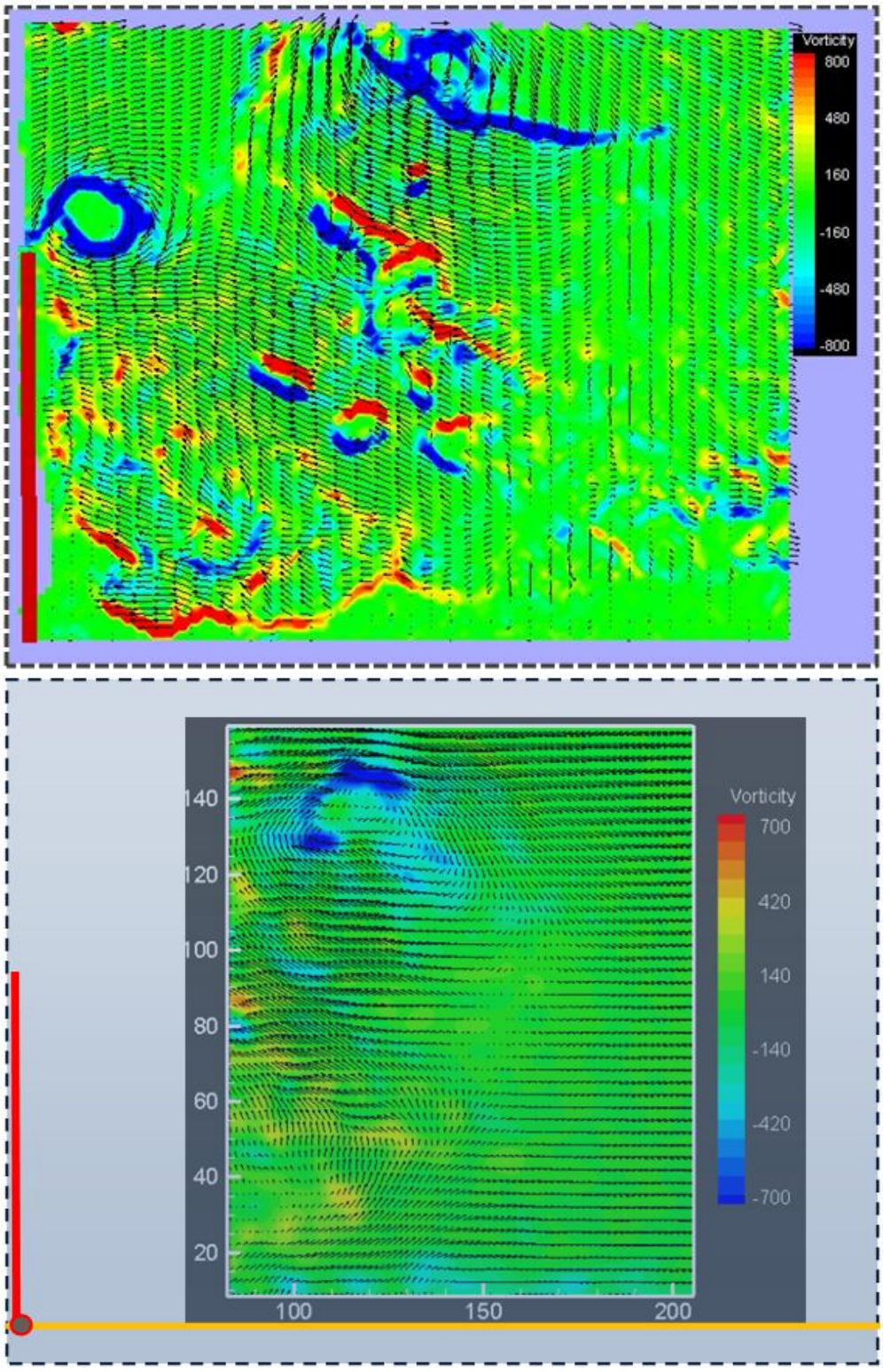

Figure 6-26: Instantaneous Vorticity contour for Str= 0.27 at 90˚, Top plot at center plane of the actuator (0.5c), bottom plot at plane 0.2c

6.3.3 Forces Estimation using Far-Field velocity data and the integral of Lamb Vector:

In this section, we attempt to use the formulation discussed in section 5.2. As the TR-PIV data are available and the velocity field can be resolved for unsteady flow field around the actuator, this earlier formulation by Wu (2005) presented a crucial progress to calculate the unsteady aerodynamic loads generated by the flow volume (figure 6-28) using only the flow velocity data in the far field (V_f) by applying integral analysis on a finite volume around solid bodies.

It's important to note that the objective of this analysis is to remain in qualitative terms, since the control volume being considered is simplified to 2-dimensinal form. However, the high aspect ratio of the actuator under investigation produces highly three dimensional flow, except the formulation in equation (5.1) maintains physical representation of the flow in each of the terms, which made it extremely useful to understand this for this type of flow by computing the contribution of each of these terms to total aerodynamics forces produced by this flow dynamics, in addition to this, the fact that the flow dynamics around the actuator during the deployment maintained similar basic features, seen in the vortices created all around the actuator tip, which believed to have major contribution to the aerodynamic forces.

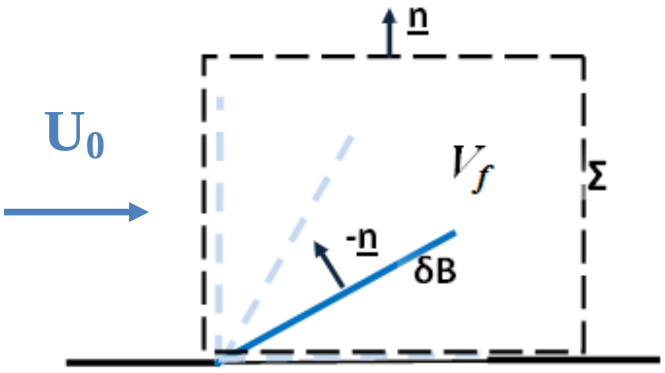

Figure 6-27: Control Volume around the actuator at the center plan (0.5 c)

(For comprehensive reason, we repeat some of the earlier discussion in chapter 5 in terms of the current setup) where equation 5.1a and 5.1b are:

$$\mathbf{F} = \rho \frac{\mathrm{d}}{\mathrm{dt}}\left[\int_{\partial \mathrm{B}} \mathbf{r} \mathrm{U}_{\mathrm{bn}} \mathrm{dS} + \int_{\Sigma} \mathbf{r} \mathrm{U}_{\Sigma \mathrm{n}} \mathrm{dS}\right] - \rho \frac{\mathrm{d}}{\mathrm{dt}} \int_{\mathrm{V_f}} \mathbf{r} \times \boldsymbol{\omega} \mathrm{dV} - \rho \int_{\mathrm{V_f}} \boldsymbol{\omega} \times \mathbf{U} \mathrm{dV} - \rho \int_{\Sigma} \mathbf{r} \times (\mathbf{n} \times \boldsymbol{\omega} \times \mathbf{U}) \mathrm{dS} + \mathbf{F}_{\Sigma} \qquad \textit{(Eq. 5.1a)}$$

$$\mathrm{F}_{\Sigma} = -\int_{\Sigma} \mathbf{r} \times [\mathbf{n} \times \mu(\boldsymbol{\nabla} \times \boldsymbol{\omega})] \mathrm{dS} + \int_{\Sigma} \mu \boldsymbol{\omega} \times \mathbf{n} \, \mathrm{dS} \qquad \textit{(Eq. 5.1b)}$$

where ρ is the fluid density, r the position vector measured from any given origin, V_f is the fluid domain bounded internally by the body surface ∂B and externally by an arbitrary control surface Σ. Both surfaces ∂B and Σ are allowed to move with velocities $\mathrm{U_{bn}}$ (actuator velocity) and $\mathrm{U_{\Sigma n}}$ the flow velocity at the surface in the normal to the surface direction.

In the following discussion the forces terms are identified in order as follow which will serve the following discussion as each term is explained in terms of its physical contribution:

$$\mathbf{I} = \rho \frac{\mathrm{d}}{\mathrm{dt}}\left[\int_{\partial \mathrm{B}} \mathbf{r} \mathrm{U}_{\mathrm{bn}} \mathrm{dS}\right], \qquad \mathbf{II} = \rho \frac{\mathrm{d}}{\mathrm{dt}}\left[\int_{\Sigma} \mathbf{r} \mathrm{U}_{\Sigma \mathrm{n}} \mathrm{dS}\right], \qquad \mathbf{III} = -\rho \frac{\mathrm{d}}{\mathrm{dt}} \int_{\mathrm{V_f}} \mathbf{r} \times \boldsymbol{\omega} \mathrm{dV},$$

$$\mathbf{IV} = -\rho \int_{\mathrm{V_f}} \boldsymbol{\omega} \times \mathbf{U} \mathrm{dV}, \qquad \mathbf{V} = -\rho \int_{\Sigma} \mathbf{r} \times (\mathbf{n} \times \boldsymbol{\omega} \times \mathbf{U}) \mathrm{dS} \qquad \mathbf{VI} = \mathbf{F}_{\Sigma}$$

Where: $VI_a = -\int_\Sigma r \times [n \times \mu(\nabla \times \omega)]dS$ and $VI_b = \int_\Sigma \mu\omega \times n\, dS$

Where: I represents the inertia effects of the incompressible fluid in the volume, and II represents the surface integral of time-rate of change of the first moment of the normal velocity to the surface. III, and IV are volumetric integrals represents the time-rate of change of the first moment of the vorticity field and the Lamb force[3] respectively. V is a surface integral represents the moment of the Lamb vector flux through the outer surface Σ. Finally VI_a and VI_b represent all viscous effects on Σ.

The above formulas are then adapted in terms of the direction of the drag and the lift, also referred to as *i* and *j* direction respectively. While all the velocity data in equation 5.1 is obtained from the already available case for TR-PIV at Re= 23,000, U=3.7 m/s and Str= 0.27, except the first term, which identify actuator kinematics. This term data is obtained from earlier direct force measurements experiments (discussed in chapter 6), in this case the encoder signal as well as the two accelerometers (tangential and radial) are adapted for the current analysis.

6.3.4 Results and Discussion:

A very good qualitative agreement has been achieved between the earlier direct force measurements and the forces calculated in the finite volume around the flow. This is shown in figures 6-28 and 6-29 for both the drag and lift coefficients. The solid-line plots in both figures represent the coefficients based on the unsteady loads measured directly from forces balance discussed in chapter 6 with the means of load cells in both drag and lift directions. While the square-symbols represents the computed coefficients based on the integral analysis for the finite volume captured by the TR-PIV. Generally the trend is captured in both cases, including the

[3] Lamb forces defined as : $\vec{l} = \vec{\omega} \, X \, \vec{U}$

location of the peak. The over shoot at the end of drag coefficient plot is due to insufficient flow velocity data in the upstream of the actuator at the full deployment position. This can be seen for the control volume in figure 6-27. During the last 15^0 of the deployment, the upstream part of the control volume used in this analysis becomes small, and only capture the low velocity region in front of the actuator. This affects the overall drag and show negative drag for this part. This primarily is due to the reverse flow behind the actuator, and the lack of upstream velocity data, which is represented with near zero values for this region. However, this part is completely independent of the analysis for earlier deployment angles (0 to 75^0).

In the meantime, the over shoot at the end of the deployment in lift coefficient case is in fact represents the force in the lift direction. This force is now applied on the wall of the wind tunnel which is not measured by the load cells in the force balance case.

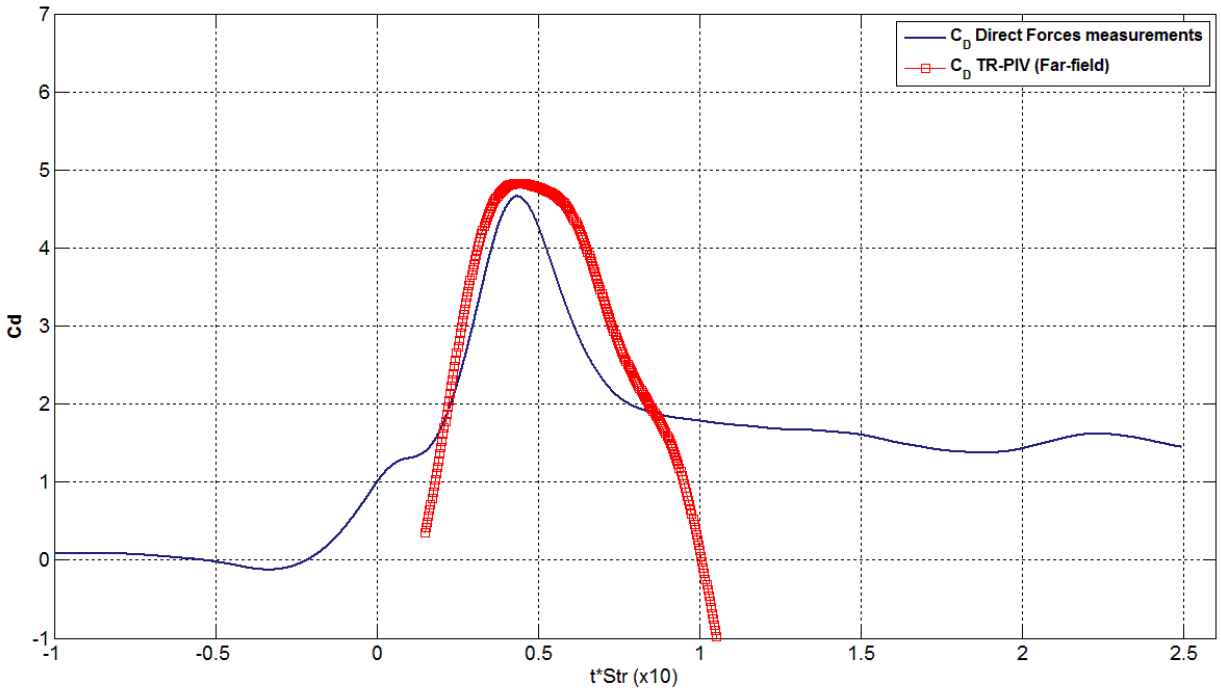

Figure 6-28: Qualitative comparison between drag coefficient computed from TR-PIV far-field analysis and drag coefficient measured directly by (Re=23,000, U=3.7m/s, Str=0.27)

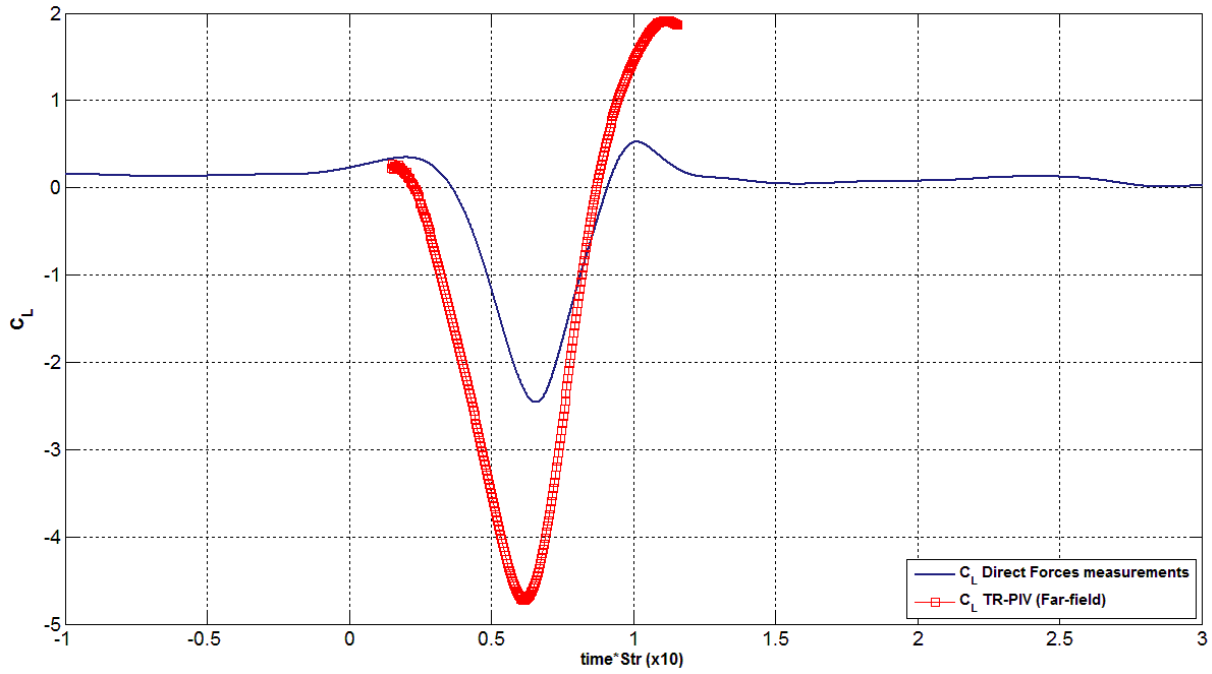

Figure 6-29 Qualitative comparison between drag coefficient computed from TR-PIV far-field analysis and drag coefficient measured directly by (Re=23,000, U=3.7m/s, Str=0.27)

Figures 6-30 and 6-31 are showing the actual drag and lift forces (N), computed from equation 5.1. The total drag in figure 6-30 is plotted with solid blue line. All the other terms in the equation are plotted in dashed lines or marks. A major contribution in to the drag is seen to be from the first term I_i, this term, which represents the actuator motion with acceleration: $\overrightarrow{a_B} = -\ddot{\alpha}\,\vec{k}\,X\,\vec{r} + \dot{\alpha}^2\,\vec{r}$ where $\ddot{\alpha}$ is the acceleration, $\dot{\alpha}$ is the angular velocity, and $\vec{r}$ the position vector for the rigid body. While second term II_i, which represents surface integral of the first moment of normal velocity to the surface, is seen in for both drag and lift cases to be insignificant.

III_i, which is shown here in light blue, represents volume integral of the time rate of change of the first moment of the vorticity. This term shows significant contribution to the loading in the drag direction as the rate vorticity is increased significantly during the deployment. It appears from this figure that this term is the responsible for maintaining high drag coefficient for longer period, above the steady state values. And also compensated for term IV_i, which is equivalent to

the lamb force in the drag direction. This term appears to have negative contribution to the overall drag. This is a result of the reverse flow behind the actuator, however, this term shown to contribute about one half of III_i. The timing of both terms, III_i and IV_i, seems to be simultaneous, while the contribution of the time rate of the vorticity component diminishes in later stages of the deployment.

V_i, which represents the surface integral of the moment of the Lamb vector flux, appears to have very little effect in the drag direction compared to the previous terms. F_Σ seen in two components VIa_i and VIb_i, represents the effect of the viscosity on the overall forces. This term is seen to have almost no effect in both force directions, as it stayed close to zero as shown in both figures (6-30 and 6-31).

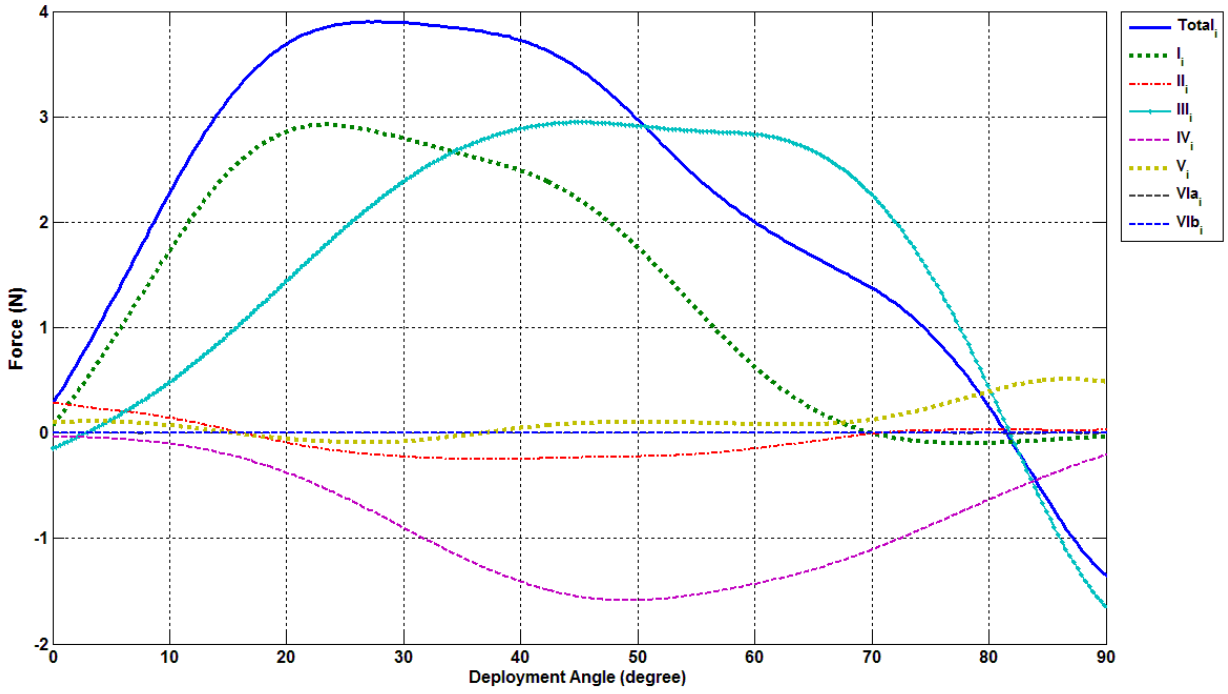

Figure 6-30: All force terms and total force in the drag direction (identified in Eq 5.1) plotted against the actuator deployment (Re=23,000, U=3.7m/s, Str=0.27)

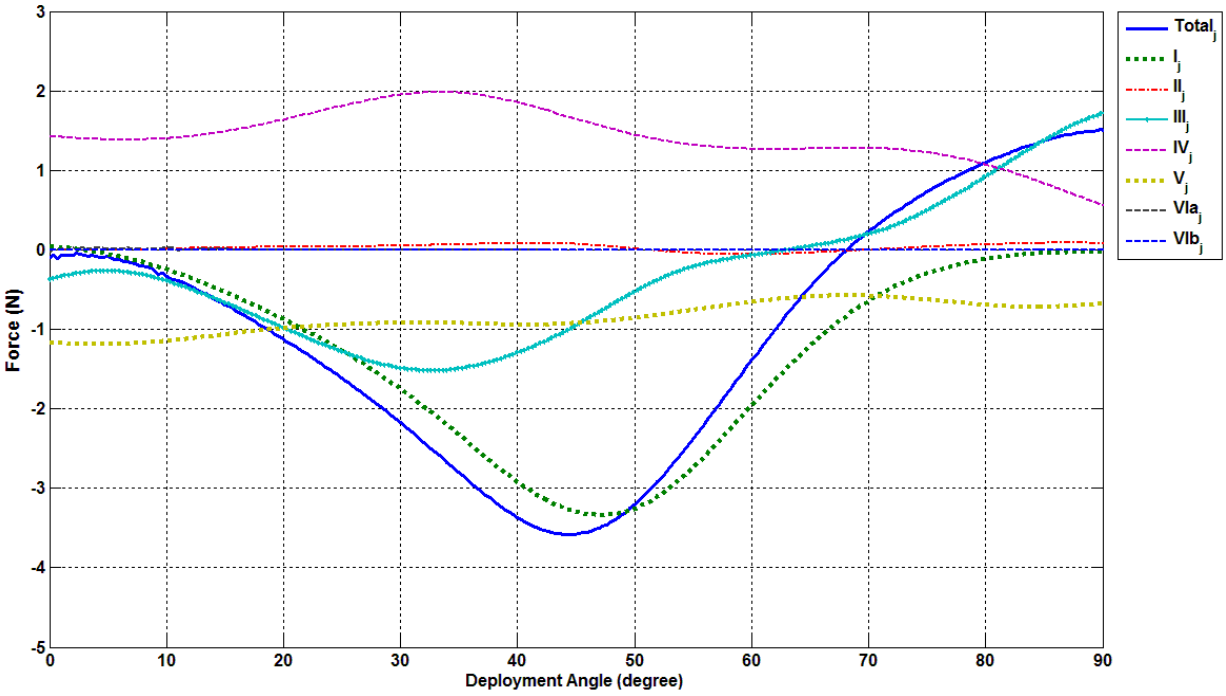

Figure 6-31: All force terms and total force in the lift direction (identified in Eq 5.1) plotted against the actuator deployment (Re=23,000, U=3.7m/s, Str=0.27)

Figure 6-31, the total lift force is shown with the solid blue line, while all the other terms are shown with dashed or marked lines. In the lift force direction, the net forces appear to correlate with motion of the rigid body I_j, while the contribution of the time dependent III_j and V_j showing negative force that is compensated with a positive force from IV_j (lamb vector term), term V_j (surface integral of the moment of the Lamb vector flux) preserved negative value over the deployment period with little change. Similarly the lamb vector term maintained positive force with small peak at about 35^o angle, which perhaps is due to the increase of the vorticity that combined with temporary increase of the u-component of the velocity in the region above the actuator tip, while limited reverse flow in u-direction behind the actuator. And as mentioned previously, II_j and F_Σ (viscosity term) seen to have insignificant contribution to the overall lift as they do in the case of the drag.

6.4 Summary:

In this part, an intensive investigation is carried out to understand the flow around an impulsively deployed actuator against incoming turbulent boundary layer flow from zero to 90^o at different Str number cases. Direct forces analyses in addition to flow visualization and TR-PIV measurements are carried out to measure the aerodynamic forces of the transient process and compare it to the steady state results at full deployment, also analyses are carried out to measure the effect of the change of Str number. In the flow visualization and TR-PIV experiments, special interest were given to the correlation between Str and the vorticity generated and the coherent structure signatures in both the upstream and the downstream of the actuator. Additionally, a comparison was made to compare the outcome aerodynamic forces with the change of both the Reynolds number and the thickness of the turbulent boundary layer. Finally, Far-field analyses were implemented to compute the aerodynamics forces using the velocity data in the finite volume around the actuator. The results were extremely beneficial to understand the underlying physics of contribution of each of the terms represented in equation 5-1, such as the volume integral time rate of change of the vorticity, forces generated due to the acceleration of the actuator, volume integral of lamb vector and other terms into the net forces in the direction of the drag and the lift. However, these analyses cannot be conclusive in quantitative terms because the three-dimensionality of the current flow.

Based on the presented analyses in this part, some conclusions were made; first, the aerodynamic forces are greatly enhanced under transients conditions compared to steady state aerodynamics. These forces increase even further with the increase of the deployment angular velocity in terms of the incoming freestream flow velocity, which is defined as Strouhal number ($Str=U_{tip}/U_0$). Flow visualization and TR-PIV with CW laser are utilized experimentally to understand the flow

dynamics that is responsible for this increase. A CW-TVS appears to be created early on the deployment. This structure wraps around the actuator and detaches but stays in the vicinity of the immediate wake of the actuator until full deployment. This structure believed to have a major contribution to the force increase.

With increasing Str., the strength of CW-TVS, as well as the vorticity in general, increases in the region behind of the actuator. In all cases, the initial CW-TVS appears to form a mushroom vortex as indicated by the flow visualization experiments, which appear to be part of a ring structure forms on the downstream that suddenly convected downstream after full deployment. CW-TVS is also followed with smaller similar vortices shed off the tip of the actuator. This shedding is seen at higher frequency in the high Re case. Finally, a far-field analyses is employed, using the velocity data from the TR-PIV, showed significant contribution of the motion of the actuator, the unsteady vorticity field to the net force in the drag case, similarly in the lift force case. Also the contribution of the lamb vector, which was in opposite direction to the lamb force, is seen to be about half of the time rate of change of the vorticity.

Chapter 7 : Split-View TR-Stereo PIV to measure 3-component velocity field

7.1 Introduction

In this chapter, a new setup for the TR-PIV is utilized to attain Stereographic view to the flow field, this will allow to obtain 3-component velocity for the flow field, similar to velocity data obtained from the Stereo PIV as it discussed in the first chapter, with the use of the high speed camera and CW laser in the present setup, a TR-Stereo PIV velocity data can be obtained.

The three dimensionality of the flow field in the actuator application as well as many of fluid applications were the main motive to come about the present setup. The 3rd component (out-of-plan component) becomes increasingly important to obtain as the flow becomes turbulent.

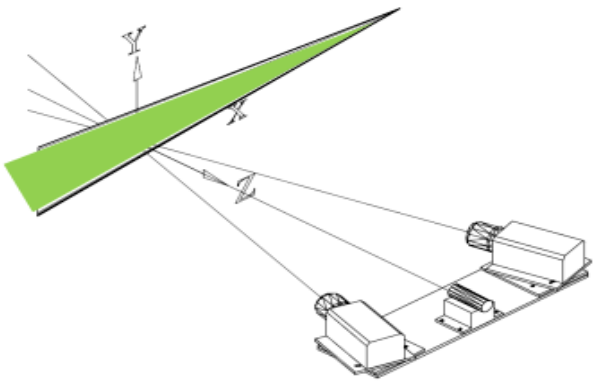

Figure 7-1: Stereo-PIV: two-camera system to resolve three-component velocity field (planar laser sheet represented by triangle in X-Y plane)

Originally, Stereo-PIV setup uses two cameras and Nd-YAG pulsed-laser to capture two simultaneous images of each camera, where the cameras are oriented to look at the flow field

from two different viewpoints (figure 7-1). This will allow to determine the three dimensional location of the particles inside the flow field. Calibration images, which will be discussed in this chapter, must be taken to the flow field to map the flow field between both camera views.

7.2 Present Setup:

In the present setup, as shown in figure 7-2, one high speed camera is used along with four planar mirrors to obtain the stereographic view to the field of view. The CW laser was used for illumination.

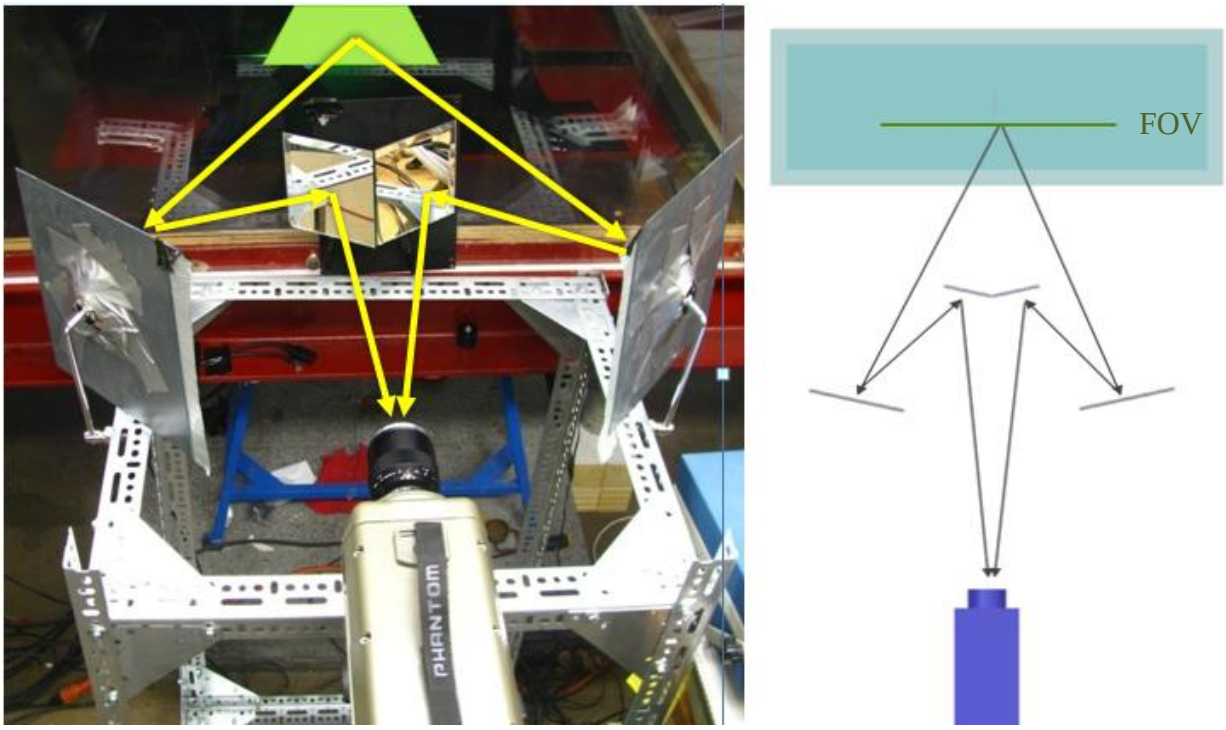

Figure 7-2: Split-view TR-SPIV setup, left: photograph of the actual setup placed in front of the WT. Right: top-view for the setup

This setup presented many advantages over the previous Stereo PIV, as it provides identical system parameters, since both views are taken with the one camera system. This minimizes their differences which makes the stereo reconstruction more robust. In addition to this, it eliminates any need for synchronization that is usually needed between the both cameras, the

laser and the flow incident. Also, in economical terms, the cost of the system is substantially reduced as the two camera system is replaced here with only one camera; similarly the low cost CW diode laser replaces the costly pulsed laser system.

The setup were used to measure the velocity during the deployment of the actuator at the center plane in the streamwise direction as shown in figure 7-3, in the this case Strouhal number was set to be 0.27 and the freestream velocity is 3.7m/s.

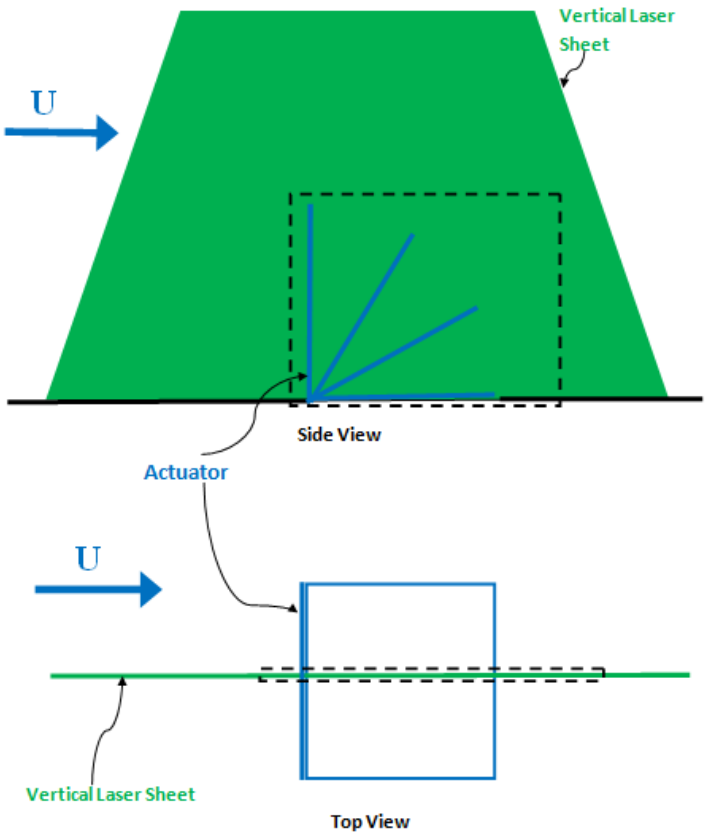

Figure 7-3 location of PIV field of view in the split-view case

7.3 Spatial Calibration:

This task is necessary to relate the world coordinate (X_w, Y_w, Z_w) to the camera's pixels coordinate in both views (x_A, y_A) and (x_B, y_B), therefore will establish the spatial relation of the

displacement of the particles in the camera plan to those in of the real displacement in the 3D world coordinates to reconstruct the 3-D velocity vector.

For this process a target plate (shown in figure 7-3) is used to obtain calibration image by both views of the camera (figure7-4). The target plate characterized by the circular dots distributed in rectangular grid with distances of 10mm in both the horizontal and the vertical directions, those dots also placed in a staggered format on two planes in z direction to resolve the third spatial dimension. The distance between the two planes in z is 1 mm, which corresponds to the thickness of the light sheet. As show in figures 7-3 and 7-4 the target-plate contains a fiducial mark at the center which is used as a reference point to prescribe a location of the origin.

Using these dots in the target plate and the location of their centroids on the camera views will allow for solving the system of equation giving by:

Figure 7-4: Target-plane with two planes in z

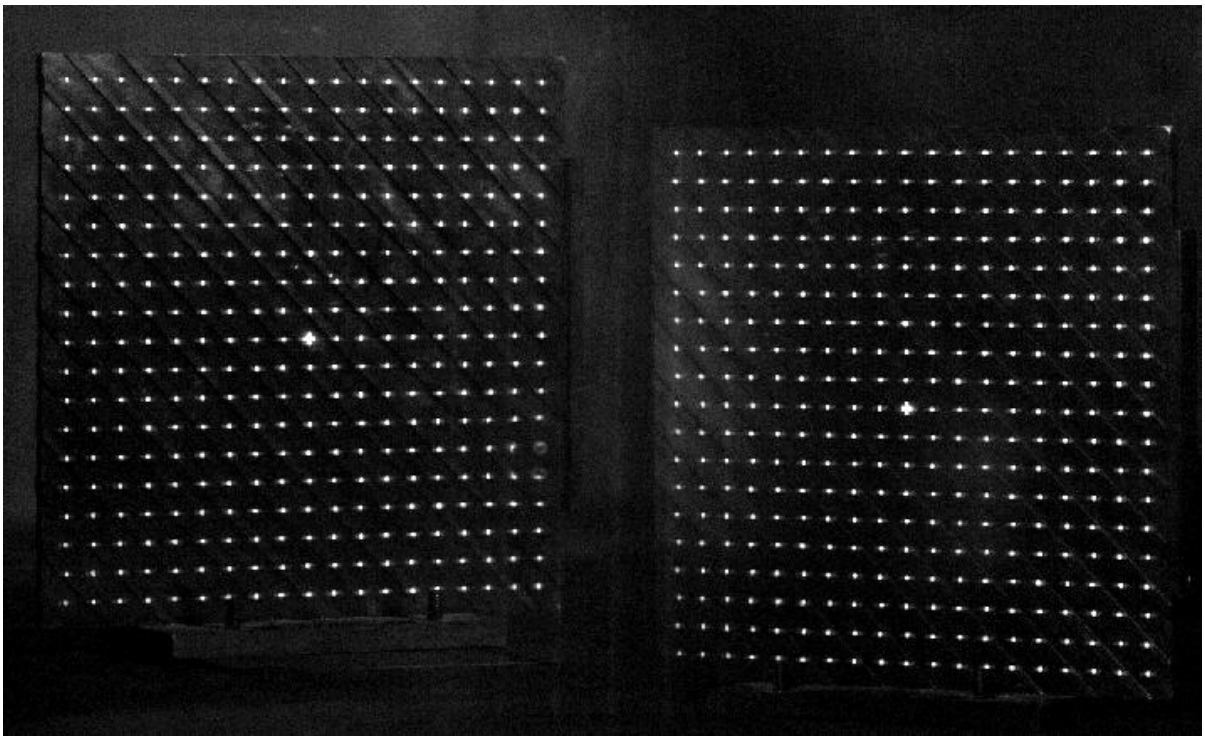

Figure 7-5: Both camera views (stereo) of the same target-plane in the one image using one camera system and four planar mirrors

$$\begin{Bmatrix} \alpha x_A \\ \alpha y_A \\ \alpha \end{Bmatrix} = \begin{bmatrix} L_{A11} & L_{A12} & L_{A13} & L_{A14} \\ L_{A21} & L_{A22} & L_{A23} & L_{A24} \\ L_{A31} & L_{A32} & L_{A33} & L_{A34} \end{bmatrix} \begin{Bmatrix} X_w \\ Y_w \\ Z_w \\ 1 \end{Bmatrix}$$

$$\begin{Bmatrix} \alpha x_B \\ \alpha y_B \\ \alpha \end{Bmatrix} = \begin{bmatrix} L_{B11} & L_{B12} & L_{B13} & L_{B14} \\ L_{B21} & L_{B22} & L_{A23} & L_{B24} \\ L_{B31} & L_{B32} & L_{A33} & L_{B34} \end{bmatrix} \begin{Bmatrix} X_w \\ Y_w \\ Z_w \\ 1 \end{Bmatrix}$$

Where L_{Aij}, L_{Bij} are the mapping model coefficients for camera view A and B respectively, and $\propto$ is constant, L_{A34} and L_{B34} are chosen to be zero to avoid trivial solution L_{ij}=0.

An over-determined system of equations is then found by applying at each dot point's centroid, the is system is then solved by a standard non-linear least square method to find the coefficients, for more information about this model and the accountability for non-idealized imaging such as geometric condition see (M. Raffel et al. 2007). In figure 7-5, a rectangular grid is overlaid on the flow image that includes both camera views.

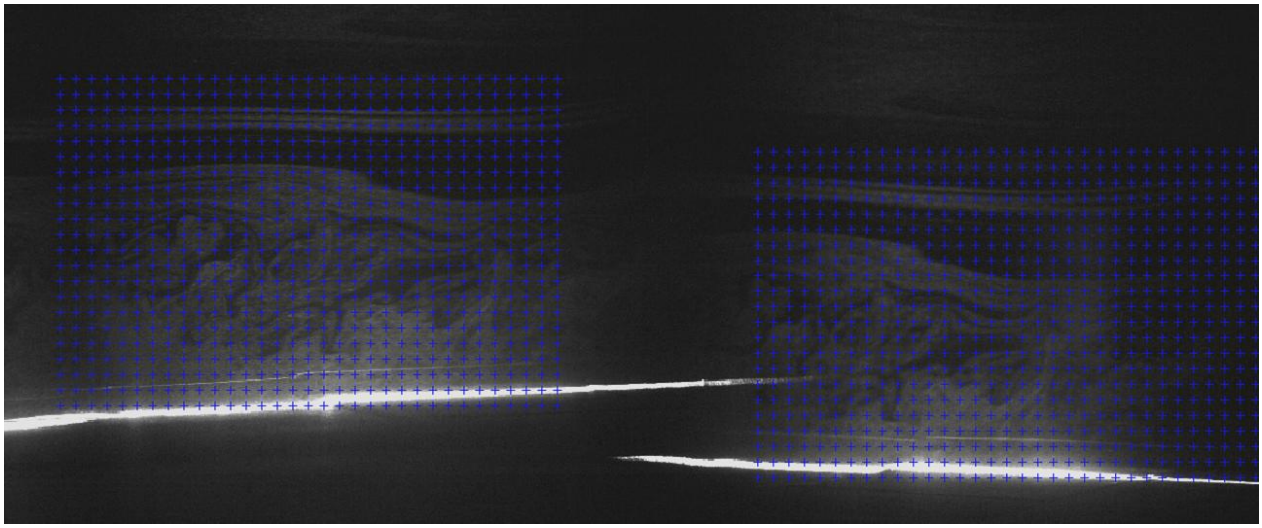

Figure 7-6: rectangular grid overlaid on the top of flow image of both camera views

7.4 Experimental Results

First, the flow visualization the images, which are at identical timing, showed the important characteristic vortex structure of the flow as shown in the figure 7-7, the black rectangular shapes are the tip of the actuator from the perspective views.

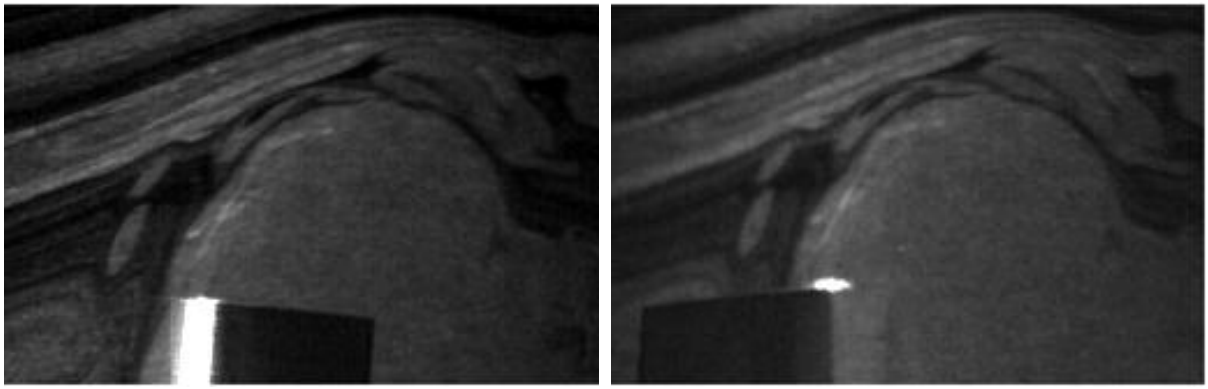

Figure 7-7: Sample two-view image cropped and magnified to show the tip vortex

For the PIV result, the vorticity contours are shown in figure 7-8 at different deployment angles during the actuator deployment, where the shadowing seen in the images are indication of the w-component of the velocity. It's notable that the vorticity of the initial TV is reduced in magnitude comparing to the 2D results.

In figure 7-9 the contour plots for the components U, V and W are shown (top to bottom), where the w-component of the velocity is shown with considerable magnitude with maximum of 4 m/sec.

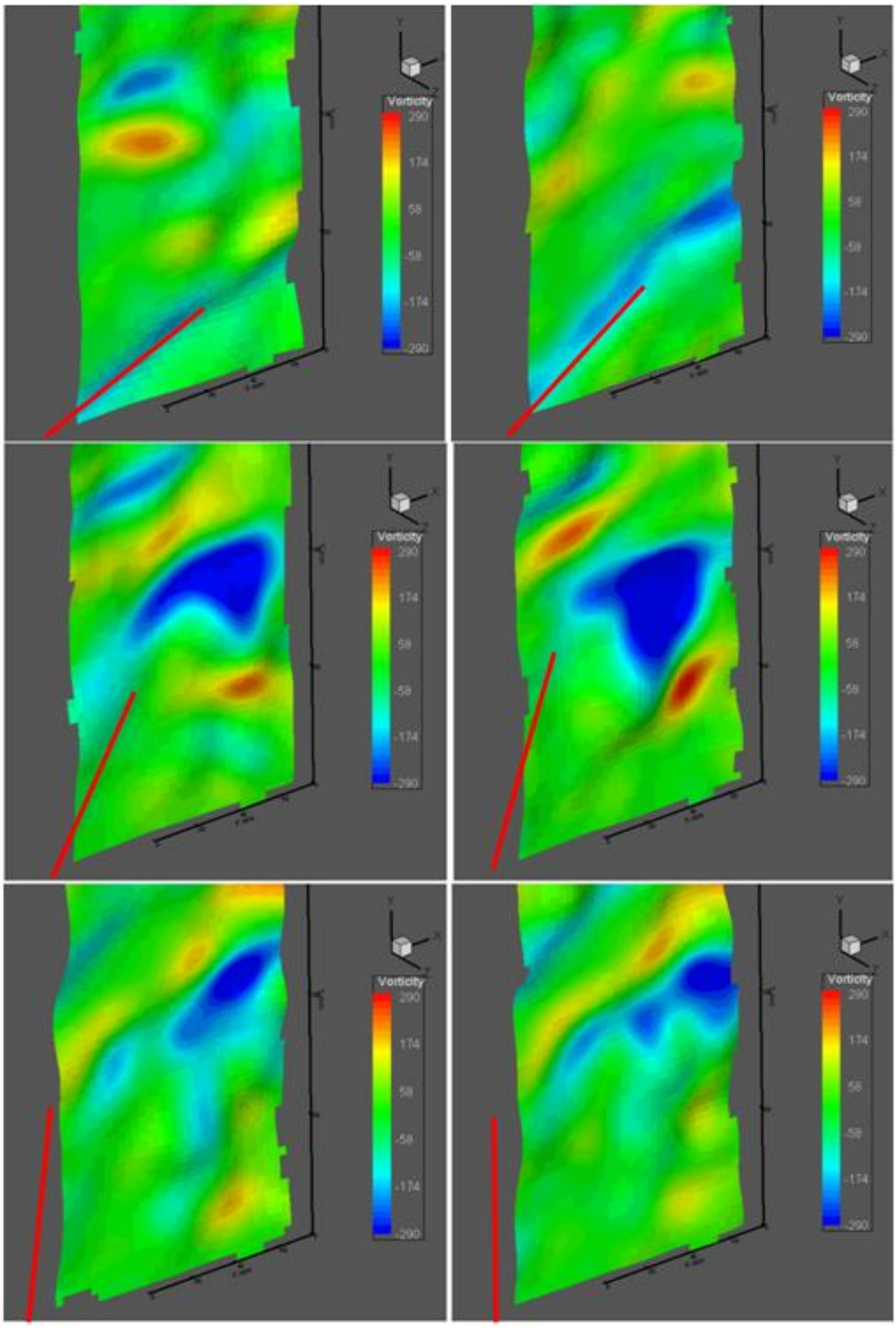

Figure 7-8 Vorticity contour for the flow developing during the actuator deployment (U= 3.7m/s, Re=23,000, Str=0.27)

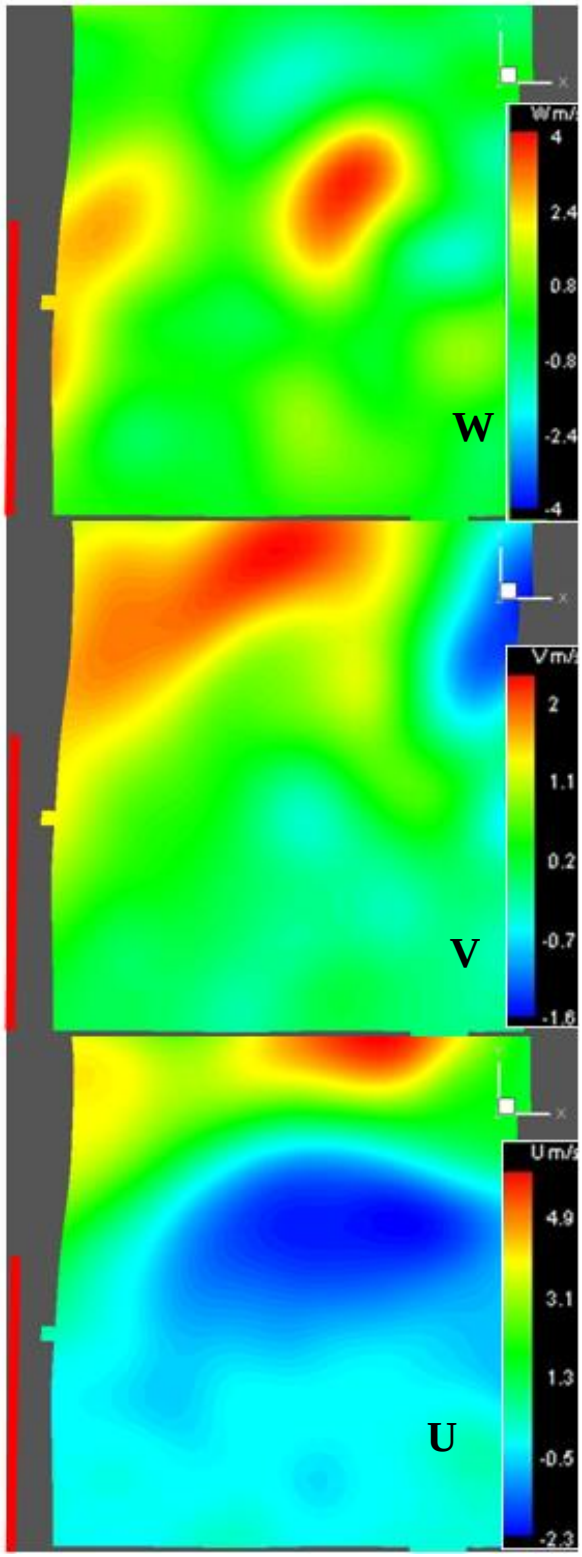

Figure 7-9: contour plots for the velocity components U, V, W, (top to bottom). The plots at the time the actuator reaches 90 degrees (U= 3.7m/s, Re=23,000, Str=0.27)

7.5 Future Improvements:

In the current setup for the split-view TR-SPIV the w-component of the velocity is obtained with the use of one high speed camera, however, the spatial resolution were lower than the TR-PIV applied previously. The main reasons for the reduction on the spatial resolution were first, the use of one camera chip to accommodate for twice FOV, which corresponds to the two views. Second, Scheimpflug condition is another limitation to how much magnification factor can be used for the field of view, since any increase of the lens focal length or decrease the distance from the camera lens to the field of view will result in strong out of focus area in one or both sides of each image view. A higher resolution camera chip would increase the spatial resolution due to the former limitation.

Chapter 8 : Summary and recommendations for future work

TR-PIV technique was evaluated in the first part of this thesis based on the velocity data obtained in TBL flow experiments, which are carried out in the wind tunnel facility. Quality of the data obtained is shown to depend on the output power of the CW laser, the quality of the images produced by the high-frame-rate camera, the size of the flow field, the speed of the flow, and/or the duration of exposure for the images. In the second part, the technique was successfully applied on the transient deployment of flat panel to investigate the difference of the aerodynamic forces in this case to the steady state case. The technique provided us with the unsteady 2-D velocity information for the flow around this actuator with high temporal resolution. This velocity information was then used to compute and analyze the vorticity fields around the actuator and revealed some significant coherent structures, some of which were only seen in the unsteady deployment. Also, different experiments are carried out with the techniques to understand the effect of the different Strouhal numbers and deployment speeds on the generated forces.

In the last section, Split-View TR-PIV setup was introduced as new setup for the technique. The main purpose of this setup was to obtain 3-component velocity vector. This was achieved by arranging only one high-frame-rate camera along with four-planar mirrors to produce two stereographic views on the same camera chip. With this arrangement the third component of

the velocity vector can be resolved with simple addition to the initial setup, while some benefits are gained by simplifying the system to use one camera.

The increase of the range of application of the techniques considered the most desired future development of these techniques. Here are some potential ways to increase the range of applications to measure velocities in higher speed flow:

- Providing the laser with higher laser power and /or higher camera resolution will directly allow to higher velocity application.
- Preprocessing conditioning to the raw images may reduce the streaking effect. This can be achieved by artificially replacing the elongated particle image by circular particle image. This will be based on the fact that the width of streaking particle image represents an image of the actual particle diameter.
- Applying the techniques with liquid flows and hydrodynamic applications would allow obtaining data at higher velocities as the seeding particles used are much larger and more reflective. This would allow obtaining stronger signal for the particles image with smaller exposure period with the same laser power range.

In terms of the Split-view setup, the spatial resolution of the obtained data is important to be increased; especially that it uses the same chip used in the one view setup. The sensitivity of the third component of the velocity also should be increased, as it is limited in the current setting to reduce the effect of the Scheimpflug effect. Using higher resolution camera chip will definitely partially help to extend both the spatial resolution and the third component sensitivity. However, an optical solution to limit the Scheimpflug effect would be highly desirable to improve the later concern.

Appendix A : PIV Processing, Post Processing and Practical Considerations

A.1 Image Correlation for PIV

Correlation analysis between two consequent frames for the seeded flow is required to obtain the velocity vectors in the flow field, which is calculated by obtaining the displacement vector in each frame as previously mentioned. As been described in Gonzales and Woods (1992), the cross-correlation is defined as:

$$R(x,t) = \sum_{m=0}^{M-1}\sum_{n=0}^{N-1} I_1^{i,j}(m,n).\, I_2^{i,j}(m-x,n-t)$$

And cross-correlation coefficient is defined as follow:

$$R(x,t) = \frac{\sum_{m=0}^{M-1}\sum_{n=0}^{N-1} I_1^{i,j}(x,t).\, I_2^{i,j}(m+x,n+t)}{\sqrt{[\sum_{m=0}^{M-1}\sum_{n=0}^{N-1} I_1^{i,j}(m,n)^2 \,.\, \sum_{m=0}^{M-1}\sum_{n=0}^{N-1} I_2^{i,j}(m+x,n+t)^2]}}$$

Where I_1, and I_2 are the Interrogation Areas (IA). I_1 is from frame 1 and the corresponding IA I_2 is from frame 2, and m and n are the local indices of pixels in I_1, I_2.

In PIV, Interrogation areas I_1 and I_2 represent the small rectangular areas which typically range between 16 to 64 pixels in width and height. These areas which contain number of particles demonstrate a specific spatial pattern of intensity. This pattern is correlated in both frames to determine the maximum normalized cross-correlation (shown in figure A-1). This maximum location corresponds to the displacement of the particles pattern.

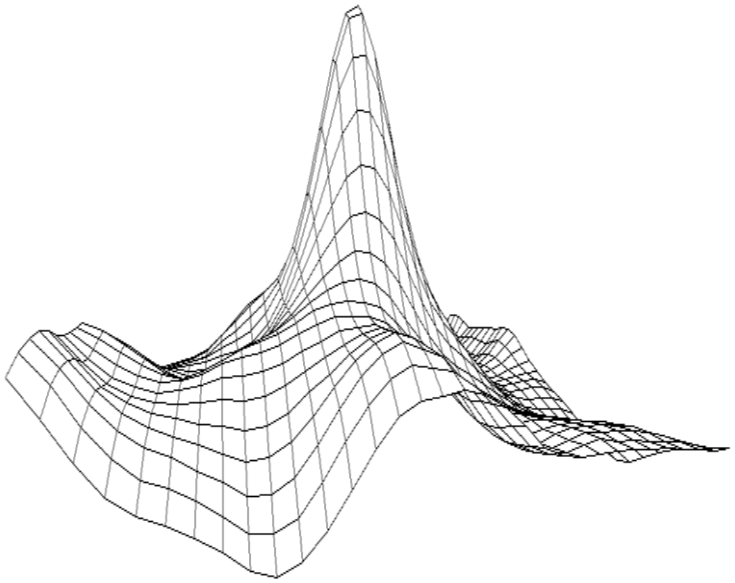

Figure A-1: Correlation map for an Interrogation Area fitted to Gaussian Profile

It is also important to mention here that the correlation values are being fit to a Gaussian profile to increase the accuracy to sub-pixel resolution using the following equation:

$$dx = x + \frac{(\ln(I_{p-i}) - \ln(I_{p+i})}{2.(\ln(I_{p-i}) + \ln(I_{p+i}) - 2\ln(I_p)} - x_0$$

Where I is the intensity value, p is the peak pixel, i is the indices of neighboring pixels, x is the integer shift and x_0 is the zero-shift.

The cross correlation can be done by direct correlation methods, however, due to the large number of data to be processed, is beneficial to implement the correlations using Fast Fourier Transform (FFT) algorithm, which can be implemented with much fewer computations.

Multi-Pass Processing:

Maintaining high dynamic range for the velocity measurements in the flow field is crucial to PIV, particularly for the flow that demonstrates high velocity gradient, such as flow with

obstructions, wall bounded flow, and jet flow. Using multi-pass processing provides the ability to have high dynamic range and not to sacrifice the accuracy of the measurements.
In multi-pass processing, a large IA (i.e. 64x64) is applied first to compute the displacement, in the following pass, a smaller IA (i.e. 16x16) is applied after making a shift of the initial IA by the amount of displacement calculated in the first pass. This will zero the shift in the new pass which will increase the correlation peak value for the small IA by correlating with the most probable IA in the second frame. This can be considered an adaptive processing, where each IA is shifted just by the right amount for the correlation process.

A.2 Image Conditioning (Preprocessing)

Applying cross correlation on images in their raw form could produce large number of spurious vectors. This could be a result of many reasons; such as electronic noise in the image background, flare due to the reflection of the laser on solid surfaces. Also in many cases, part of the image required to be masked and not to be processed as in areas where light is reflected from solid objects. For these reasons, some conditioning for the images (preprocessing) can be done to enhance the image quality and facilitate the processing.
The preprocessing tasks done in present work were global or local preprocessing, the global processing such as background noise subtraction and mask application (to identify the area of interest for processing) were applied on the whole image. The local preprocessing applied here basically is a normalization of IA intensities by the average intensity of this specific IA. This compensates for variation of the laser spatial intensity and/or camera gain level, as shown in figure (A-2) images c and d are the result of image of dividing a and b by its own intensity average respectively.

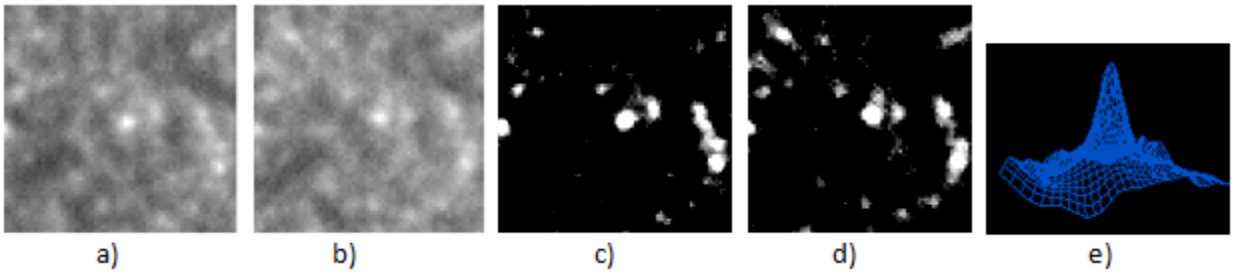

Figure A-2: Example of noisy-background image in a and b, normalization applied in c and d using the average intensity of the IA to improve the image quality; a) IA from 1st frame b) IA from 2nd frame, c) Normalized IA from 1st frame, d) Normalized IA from 2nd frame. e) The corresponding correlation map.

A.3 Post processing

Post processing in PIV is an essential task to obtain valid velocity vector field. This task requires a good understanding of the velocity field being measured. In most cases, the processing for the PIV is applied on hundreds of PIV pairs at once, which will produce tens of thousands of velocity vectors, and would need hours of processing time. This would require a robust post processing approach, and an optimum choice for validation filters parameters.

Figure A-3 shows the effect of applying the velocity validation filters and interpolation on the velocity vector, the main purpose of the post processing is to eliminate the invalid vectors from the flow field; second is to replace these vectors in the flow fields with either valid or close to the expected value at this location. For this reasons applying the optimum post processing (validation) filters is very crucial to obtain good results in addition to reduce the time needed to processing. In TR-PIV, some difficulties appear in implementing this task in an automated fashion, particularly when the flow under investigation demonstrates high unsteadiness in the velocity field. This requires re-identifying new optimal values for the validation filters parameters in between file processing.

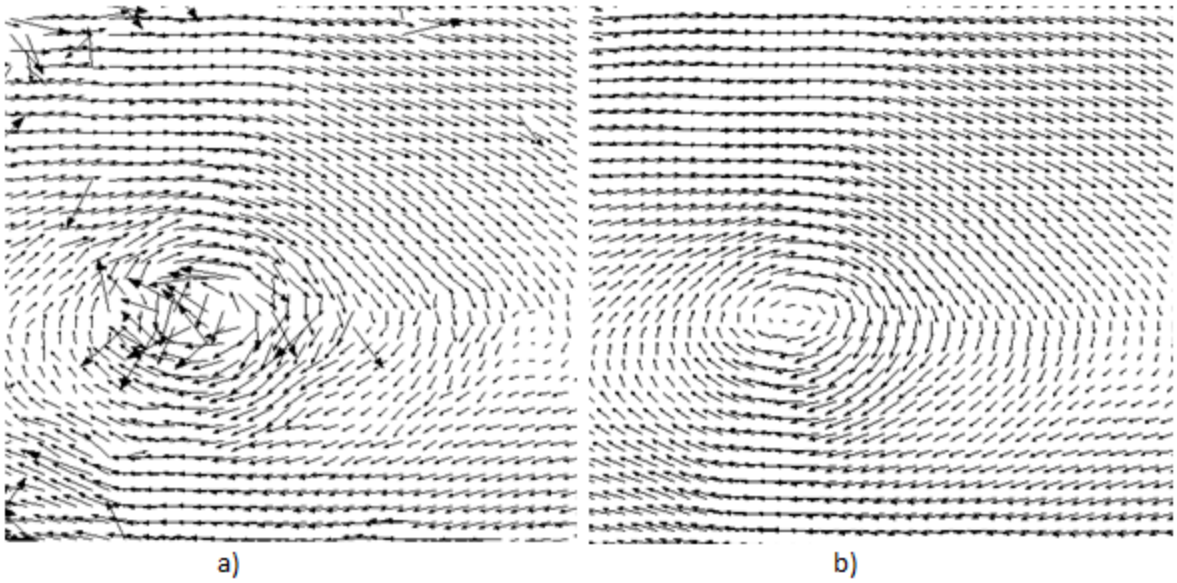

Figure A-3: Post processing effect a) before vector validation, b) after vector validation

Validation process is not only implemented in the post processing; in multi-pass processing some of these filters can be applied to remove initial invalid vectors. This way in the following pass another valid vector can be determined to limit the use of interpolation.

The validation filters can be categorized as following:

1. Global (Image based) filters.
2. Global (Velocity-based) filters.
3. Local (Velocity-based) filters.

Global (Image-based) filters

a. Intensity-based filter: by thorough inspection of the images, the range of the light intensity due to the particle imaging can be determined so correlation to be only executed for the regions with average intensity within this range. This would allow excluding any correlation to be executed in dark low intensity regions, which would be identified as

background noise. This also can be applied on higher intensity regions as in reflective surfaces.

b. Correlation-Peak-value filter (Signal-to-noise-ratio): This filter is considered the most important filter to be applied, and it's a measure of the correlation quality. Peak value filter is the ratio of the largest correlation peak value to the second largest; it's also known as the Signal-to-noise-ratio (SNR). The value of 1.3 has been shown by Adrian (1996) to be appropriate criterion for this ratio, however, this value should be determined for each experiments to improve correlation outcome.

Global (Velocity-based) filters:

c. Velocity range filter: A global filter to be applied on the whole flow field, by setting a maximum and minimum values for all velocity components, and eliminate any vector beyond these set values.

d. Velocity standard deviation filter: a global filter using the statistical standard deviation of the existing velocity data as a factor to eliminate the invalid velocity vectors.

Local (Velocity-based) filters:

e. Mean local filter: This filter use the neighboring IA's mean velocity value to determine the validity of the center vector based on prescribed tolerance value. In this filter, a neighborhood is usually range from 3x3 to 9x9 IA's.

f. Median local filter: similar to the mean local filter, but the median value instead, and it's been argue by Westerweel (1995) to more effective compare other velocity based filters.

Post Processing Interpolation

After applying validation filters and replacing the invalid vector with valid ones, the velocity field will be left with some vacant spaces, where the vectors are removed and no valid vector can be found to replace them. At this stage some interpolation can be used to fill out these vacant spaces with velocity vectors that can be determined by either the median or mean local neighbors. The interpolation process must be carefully implemented, because it may result in creating a large new region of data without merits.

A.4 Practical Considerations:

Seeding Particles Size and Density, and Field of View:

Due to the limitation on the size of the particles to ensure they accurately follow the fluid motion without significant lag, a small particle is used (further discussion provided later in this chapter) for example, the particles used to seed most air flow applications have to be in order of one micron. This small sized particle sets limitations on the flow field size; hence each particle should be imaged clearly in the camera where it should be projected on more than one pixel to avoid pixel locking effect which would increase error due to pixel discretization (this value increases to more two pixels per particle for accurate turbulence measurements (Prasad et al. 1992), (Christensen KT 2004), (Angele K et al. 2005). Typically the flow field in the camera CCD is divided into smaller IA's, each area should contain ten (or more) pairs of particles (figure A-4) on average to obtain a quality statistical correlation between both frames according to (Keane and Adrian 1995).

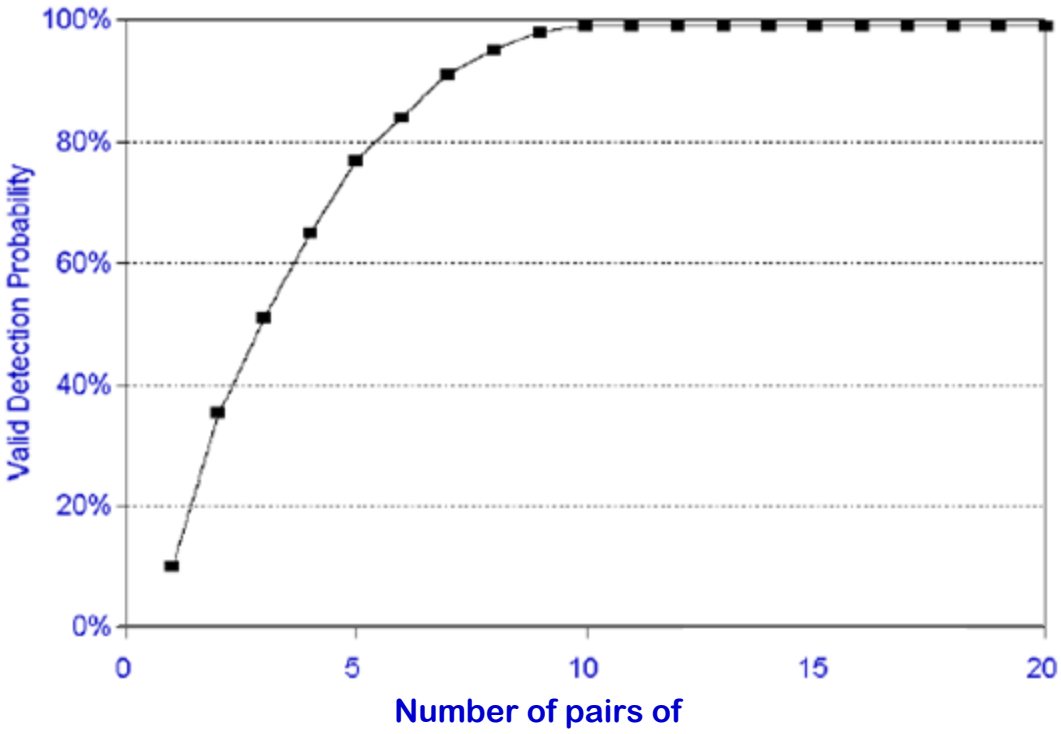

Figure A-4: The increase of between interrogation areas (x-axis) increases the correlation peak value, maintaining ten pairs overlap between the both interrogation areas showed high probability for a valid correlation (Keane and Adrian 1995).

Velocity Gradient:

As mentioned earlier, the velocity vector computed in PIV represents the motion of group of particles, hence it is very important to understand that the outcome vector not necessary represents the true velocity value, it's also important to know that it does not represent the average velocity vector of this IA, which is a common misconception, because the method to calculate the velocity vector rely on finding the maximum correlation to determine the displacement, the outcome vector would have a bias towards the most likely velocity value in this region instead of the average value of the velocity.

For this matter, the IA's size must be chosen to contain the smallest velocity gradient possible. This could require different processing for different areas in the flow field based of the velocity gradient of the velocity, however, recent processing technique uses multi passes

processing, which, allowed to be process smaller IA therefore smaller velocity gradient regions, at the same time maintaining high global dynamic range for the velocity.

Using minimum of ten pairs of particles overlap also meant a reduction on the spatial resolution, since each measured displacement accounts for the most likely displacement of the entire group.

Time difference limitation:

Flow Reynolds' number and type of flow (i.e. laminar or turbulent, two-dimensional or three-dimensional flow) created limitation on how large Δt can be. Because of Δt is a universal parameter for the entire flow field, it has to be chosen to accommodate the highest velocity in the flow field, while this would decrease the accuracy of measuring the lowest velocity values as well as turbulence quantities. TR-PIV presents a solution to this problem by giving the ability to compute the low velocity values at using low sampling rate of the acquired images and vice versa for the high velocities, Multi-pass processing also presents a limited solution for this problem as mentioned earlier in this chapter.

Measuring Two-Dimensional Vs Three-Dimensional Flow:

Early PIV used only one camera to image the flow in planar illuminated sheet of laser light. The use of only one camera made it possible for the observer (the camera) to only compute the two velocity components in field of view (FOV) direction; also it's required that the particles to be continue to exist inside FOV in the second frame. This creates a limitation on measuring any highly three-dimensional flow. Later advances on PIV, such as Stereo-PIV, provided the ability to measure three components of the velocity by the use of second camera, however, the third component (out-of-plane component) must be relatively small, which made

it not suitable for isentropic three-dimensional flow applications with large FOV. Recently (as mentioned on chapter one), some volumetric techniques introduced such as V3V (TSI Inc.) using three cameras and illumination of volume flow field, which was an important development to the PIV based measurement, however, it's still not suitable for air and gases applications[4] due to the scarcity of light available to create strong signal-to-noise ratio by the smaller particles used in the gas flow.

[4] V3V (TSI Inc.) is suitable for liquids flow (i.e. water) with preset volume of 140x140x100 mm^3, using seeding particles with about 10 μ m diameter.

Bibliography

Adrian R.J., Yao C.S. (1985): Pulsed laser technique application to liquid and gaseous flows and the scattering power of seed materials, Appl. Optics, 24, pp. 44–52

Adrian, R. J. (1986). An image shifting technique to resolve directional ambiguity in double-pulsed Velocimetry. Appl. Opt. 25, 3855-38858

Adrian, R. J. (1996) Bibliography of Particle Velocimetry Using Imaging Methods: 1917-1995, TSI Inc. St. Paul, Minnesota. Also available as TAM Report No. 817, UILU-ENG-96-6004, Dept. Theoretical and Applied Mechanics, Univ. Illinois at Urbana-Champaign.

Adrian, R. J. (1996), Twenty years of Particle Image Velocimetry. 12th International Symposium on Applications of Laser Techniques to Fluid Mechanics, Lisbon, 2004

Anderson, J. M., Streitlien, K., Barrett D. S. & Triantafyllou M. S. 1998 Oscillating foils of high propulsive efficiency. J. Fluid Mech. 360, 41–72.

Andreopoulos J., Agui J. H., Wall-vorticity flux dynamics in a two-dimensional turbulent boundary flow, *J. Fluid Mech.* (1996), 309 : pp 45-84

Angele, K. P., Muhammad-Klingmann, B. (2005) A simple model for the effect of peak-locking on the accuracy of boundary layer turbulence statistics in digital PIV, Experiments in Fluids Vol 38: 341–347

Arakawa S., Okamoto K., "Three-dimensional spatiotemporal recursive cross correlation method for dynamic PIV" 6th international Symposium on Particle Image Velocimetry Pasadena, USA (2005)

Balakumar B.J, Adrian R., Large and very large motion in channel and boundary-layer flows, Philosophical transactions - Royal Society, vol:365 iss:1852 pg:665, 2007.

Balint, J., Wallace, J.M. & Vukoslavcevic, P. 1991 The velocity and vorticity vector fields of a turbulent boundary layers, Part 2. Statistical Properties. J. Fluid Mech. 288, 53-86

Betz, A., “Ein Beitrag zur Erkl¨arung des Segelfluges,” Zeitschrift f¨ur Flugtechnik and Motorluftschiahrt, Vol. 3, 1912, pp. 269–272

BIRCH J. M. & DICKINSON, M. H. 2001 Spanwise Flow and the Attachment of the Leading-Edge Vortex on insect Wings. Nature, Vol. 412, No. 6848, 729–733, doi:10.1038/35089071.

BUCKHOLTZ, J. H. J. & SMITS, A. J. 2006 On the evolution of the wake structure produced by a low-aspect-ratio pitching panel. *J. Fluid Mech.* 546, 433–443.

Christensen KT (2004) The influence of peak-locking errors on turbulence statistics computed from PIV ensembles. Exp. Fluids 36:484–497

Christensen KT; Adrian RJ (2001) Statistical evidence of hairpin vortex packets in wall turbulence. *J. Fluid Mech*, Vol 431, 433-443

Coles, D.E., 1956, The law of the wake in the turbulent boundary layer, J. Fluid Mech.,191226.

Dickinson, M. H. and Götz, K. G. (1993). Unsteady aerodynamic performance of model wings at low Reynolds numbers. J. Exp. Biol. 174, 45-64.

Dickinson, M. H., Lehmann, F. and Sane, S. P. (1999). Wing rotation and the aerodynamic basis of insect flight. Science 284, 1954-1960.

Dracos T, Virant M, Maas HG (1993) Three-dimensional particle tracking velocimetry based on photogrammetric determination of particle coordinates. In: Cha SS, Trollinger JD (eds) Optical diagnostics in fluid and thermal flow. SPIE, Bellingham, Washington, pp 457–466

Ellington, C. P. (1984). The aerodynamics of hovering insect flight. I. The quasi-steady analysis. Philos. Trans. R. Soc. Lond. B. Biol. Sci. 305, 1-15.

Ellington, C. P. (1999). The novel aerodynamics of insect flight: applications to microair vehicles. J. Exp. Biol. 202, 3439-3448

Ellington, C. P., van den Berg, C., Willmott, A. P. & Thomas, A. L. 1996 Leading-edge vortices in insect flight. Nature 384, 626–630

Elzawawy A., Bravo L., Andreopoulos Y., Watkins C., Compressibility and Density Effects in Free Subsonic Jet Flows: Three Dimensional PIV Measurements of Turbulence" 37th AIAA Fluid Dynamics Conference and Exhibit, 2007

Falco R. E., Coherent motions in the outer region of turbulent boundary layers, Phys. Fluids 20, S124 (1977); doi:10.1063/1.861721

FREYMUTH, P. 1988 Propulsive vortical signature of plunging and pitching airfoils. AIAA J. 23, 881–883 (1988)

Gonzales Rafael C., Woods Richard E. "Digital Image Processing. Addison"-Wesley, 1992

GREEN, M. A. & SMITS, A. J. 2008 Effects of three-dimensionality on thrust production by a pitching panel. J.Fluid Mech., vol. 615, 211–220.

Guezennec Y., R.S. Brodkey, N. Trigui and J.C. Kent, Algorithms for full automated three-dimensional particle tracking velocimetry. Exps. in Fluids, 17 (1994), pp. 209–219.

Head, M. R. & Bandyopadhyay, P. 1981 New aspects of turbulent boundary layer structure. J. Fluid Mech. 107, 297{337.

Hedenström, A., Johansson, L. C., Wolf, M., von Busse, R., Winter, Y. and Spedding, G. R. (2007). Bat flight generates complex aerodynamic tracks. Science 316, 894-897.

Hedenström, A., Rosén, M. and Spedding, G. R. (2006). Vortex wakes generated by robins Erithacus rubecula during free flight in a wind tunnel. J. R. Soc. Interface 3, 263-276.

Hedrick, T. L., Usherwood, J. R. and Biewener, A. A. (2004). Wing inertia and whole-body acceleration: an analysis of instantaneous aerodynamic force production in cockatiels Nymphicus hollandicus) flying across a range of speeds. J. Exp. Biol. 207, 1689-1702.

HO C. H. & TAI, Y-C. 1998 Micro-electro-mechanical systems (MEMS) and fluid flows, Annu. Rev. Fluid. Mech. 1998.30:579-612.

Ho, S., Nassefa, h., Pornsinsirirakb, Taib, N. Y-C, Ho, C-M. 2003 Unsteady aerodynamics and flow control for flapping wing flyers, Progress in Aerospace Sciences 39, 635–681(2003).

Honkan, A. and Andreopoulos, J. "Vorticity, Strain rate tensor and Dissipation in the Near Wall of Turbulent Boundary Layer," J. Fluid Mech., 350, pp. 29-96, 1997.

Jardin T., Chatellier L., Farcy A., David L., Correlation between vortex structures and unsteady loads, Exp Fluids (2009) 47:655–664 for flapping motion in hover

Kármán, T. von (1921) Über laminare und turbulente Reibung, Z. Angew. Math. Mech., 1, 233-252, (English translation in NACA Technical Memo. 1092).

Kasagi N, Nishino K (1993) Flow field measurement with particle image velocimetry. JSME 96:34–39

Keane, R. D., Adrian, R. J. and Zhang, Y., Super-resolution particle imaging velocimetry, Meas. Sci. Technol, 1995, 6, 754–768.

Kim D. & Gharib, M. 2010 Experimental study of three-dimensional vortex structures in translating and rotating plates Exp Fluids (2010) 49:329–339. DOI 10.1007/s0034801008726.

Klebanoff, P.S., 1955, Characteristics of turbulence in a boundary layer with zero pressure gradient, NACA Rept. 1247

Kline and Robinson (1990) Turbulent boundary layer structure - Progress, status, and challenges, Structure of turbulence and drag reduction; Zurich, Switzerland

Knoller, R., "Die Gesetze des Luftwiderstandes," Flug- und Motortechnik (Wien), Vol. 3, No. 21, 1909, pp. 1–7

Kolmogorov A.N 1941 The local structure of turbulence in incompressible viscous fluid for very large Reynolds numbers. Dokl. Akad. Nauk SSSR. 30, 301–305.

Koumoutsakos, P. & Shiels, D. 1996 Simulations of the viscous flow normal to an impulsively started and uniformly accelerated flat plate. J. Fluid Mech. 328, 177–227.

Kurtulus D. F., Scarano F., David L., Unsteady aerodynamic forces estimation on a square cylinder by TR-PIV, Exp Fluids (2007) 42:185–196

Lighthill J Brown L.M, Pais A, Pippard B Twentieth century physics vol. II1995pp. 795–912. Eds. New York, NY:Amer. Inst. Phys..

Lilienthal, O., 1889, Der Vogelflug als Grundlage der Fliegekunst (Birdflight as the Basis of Aviation)

Maas HG, Gruen A, Papantoniou D (1993) Particle tracking velocimetry in three-dimensional flows. Part 1. Photogrammetric determination of particle coordinates. Exp Fluids 15:133–146

Markus Raffel, C. Willert, S.Wereley, J. Kompenhans "Particle Image Velocimetry, A practicle guide" 2nd ed. 2007

Marongiu C., Tognaccini R., Far-Field Analysis of the Aerodynamics Force by Lamb Vector Integrals, AIAA, Vol. 48, 2010

Maxworthy, T. 1981 The fluid-dynamics of insect flight. Ann. Rev. Fluid Mech 13:329–350.

Meinhart CD; Adrian RJ (1995) On the existence of uniform momentum zones in a turbulent boundary layer. Phys Fluids, Vol 7, 694-696

Pierides A., PhD Dissertation 2010, An Experimental Study on the Characteristics of Transient Deployment of Hinged Wing Actuators within a Boundary Layer

Pierides A., Elzawawy A., Andreopoulos Y., Transient force generation during impulsive rotation of flat panels embedded in boundary layers, *J. Fluid Mech*., "under review"

Pope Stephen "Turbulent Flows" Cambridge University Press; 1st edition (2000)

Prandtl, L. 1925. Bericht über Untersuchungen zur ausgebildeten Turbulenz, Z. Angew. Math, Meth., 5, 136-139

Prasad AK (2000) Stereoscopic particle image velocimetry. Exp Fluids, Vol 29, 103-116

Ringuette, M. J., Milano M. & Gharib, M. 2007 Role of tip vortex in the force generation of low-aspect ratio normal flat plates, *J. Fluid Mech*. Vol. 581, 453-468.

Robinson, S. K. 1991 Coherent motions in turbulent boundary layers. Annu. Rev. Fluid Mech. 23, 601{639.

Sane, S. P. (2003). The aerodynamics of insect flight. J. Exp. Biol. 206, 4191-4208.

Santiago J.G., S.T. Wereley, C.D. Meinhart, D. Beebee, and R.J. Adrian, "A particle image velocimetry system for microfluidics," Exp. Fluids, Vol. 25, No. 4, 316-319, (1998)

Sarpkaya T & Kline, H. K. 1982 Impulsively-started flow about four types of bluff body. Trans. ASME I: J. Fluids Engng 104, 207–213.

Schlichting H Boundary-layer theory. In McGraw Hill 1956 New York, NY: McGraw Hill

Sharp, K.V., Hill, D.F., Troolin, D., Walters, G., Lai, W., 2009, "Volumetric 3-component Velocimetry (V3V) measurements of the turbulent flow in stirred tank reactors," Experiments in Fluids, doi 10.1007/s00348-009-0711-9

Spalart, P.R., 1988, Direct simulation of a turbulent boundary layer up to $Re_\theta = 1400$, J. Fluid Mech., 187, 61-98

Spedding, G. R. (1993). On the significance of unsteady effects in the aerodynamic performance of flying animals. Contemp. Math. 141, 401-419.

Suryadi, A. Ishil T. & OBL, S. 2010 Stereo PIV measurement of infinite, flapping rigid plate in hovering condition, Exp. Fluids (2010) 49:447–460. DOI 10.1007/s00348-009-08814-3.

Taira K, Dickson, W.B, Colonious, T. & Dickinson, M.H. & Rowley, C. W 2007 Unsteadiness in a Flow over a Flat Plate at Angle-of Attack at Low Reynolds Numbers, AIAA-65342 conference paper.

Theodorsen, T. 1952 Mechanism of turbulence. In Proc. Second Midwestern Conference on Fluid Mechanics, Mar. 17-19 . Ohio state University, Columbus, Ohio.

Triantafyllou, M. S. Techet, A. H., Zhu, Q., Beal, D. N., Hover F. S. &. Yue, D. K. P. 2003 Vorticity control in fish –like propulsion and control, J. Integ. Comp. Biol, 42, 1026-1031.

Triantafyllou, M. S., Triantafyllou, G. S. & Gopalkrishnan, R. 1991 Wake mechanics for thrust generation in oscillating foils. Phys Fluids A 3(12):2835–2837.

Troolin D R; Longmire E K; Lai WT (2006) "Time-resolved PIV analysis of flow over a NACA 0015 airfoil with Gurney flap," Experiments in Fluids, 41, pp. 241-54

Von Ellenrieder K. D., K. Parker and J. Soria, 2003, Flow structures behind a heaving and pitching finite-span wing J. Fluid Mech., 490 : pp 129-138

Wernet MP ‘Temporally resolved PIV for space–time correlations in both cold and hot jet flows‘ - Measurement Science and Technology, 2007

Westerweel J. (1993): Digital Particle Image Velocimetry – Theory and application Ph.D. Dissertation, Delft University Press, Delft

Westerweel J., Scarano F. (2005): Universal outlier detection for PIV data, Exp. Fluids, 39, pp. 1096–1100.

Willmott, A. P., Ellington, C. P. and Thomas, A. L. R. (1997). Flow visualization and unsteady aerodynamics in the flight of the hawkmoth, Manduca sexta. Philos. Trans. R. Soc. B. Biol. Sci. 352, 303-316.

Wu J. Ma H. Y., Zhou M. D, Vorticity and vortex dynamics, Springer, 2006

Wu J. Unsteady fluid-dynamics force solely in terms of control-surface integral, Physics of fluids, 17, 2005